The Electron-Capture Branch of ^{100}Tc and Implications for Neutrino Physics

Sky Sjue

A dissertation submitted in partial fulfillment
of the requirements for the degree of

Doctor of Philosophy

University of Washington

2008

Program Authorized to Offer Degree: Physics

University of Washington
Graduate School

This is to certify that I have examined this copy of a doctoral dissertation by

Sky Sjue

and have found that it is complete and satisfactory in all respects,
and that any and all revisions required by the final
examining committee have been made.

Chair of the Supervisory Committee:

_____

Alejandro García

Reading Committee:

_____

Alejandro García

_____

Stephen Ellis

_____

Kurt Snover

Date: _____

University of Washington

Abstract

The Electron-Capture Branch of ^{100}Tc and Implications for Neutrino Physics

Sky Sjue

Chair of the Supervisory Committee:
Professor Alejandro García
Physics

This study presents a measurement of the electron-capture (EC) branch of the decay of ^{100}Tc, with the result $B(\mathrm{EC}) = (2.6 \pm 0.4) \times 10^{-5}$. The EC branch measurement, in conjunction with measurements of single-beta and two-neutrino double-beta decay rates in the $A = 100$ system, provides an important test for nuclear many-body theories used to calculate the neutrinoless double-beta decay rate of ^{100}Mo. A discussion of the implications of our branch measurement for double-beta decay calculations follows for both the single-state dominance hypothesis and the proton-neutron quasiparticle random phase approximation. The matrix element that determines the EC branch also determines the cross section for neutrino capture on ^{100}Mo, which has the potential to measure pp neutrinos spectroscopically at relatively low energies because of its small neutrino-capture threshold, $Q_{\mathrm{EC}} = 168$ keV. Our branch measurement determines the efficiency of a proposed solar-neutrino detector using ^{100}Mo to be $\approx 80\%$ greater than previous estimates.

TABLE OF CONTENTS

LIST OF FIGURES

LIST OF TABLES

ACRONYMS

ADC: Analog-to-digital converter

BR: Branching ratio

CKM: Cabibbo-Kobayashi-Maskawa matrix

CVC: Conservation of vector current

EC: Electron capture

FWHM: Full width at half maximum

IC: Internal conversion

IIE: Internal ionization and excitation

LEPS: Low energy photon spectrometer

MNS: Maki-Nakagawa-Sakata matrix

MSW: Mikheyev-Smirnov-Wolfenstein effect

NIM: Nuclear instrumentation modules

PMT: Photomultiplier tube

QCD: Quantum Chromodynamics

QED: Quantum electrodynamics

RFQ: Radiofrequency quadrupole

SCA: Single channel analyzer

SCC: Second-class currents

TAC: Time-amplitude converter

TTL: Transistor-transistor logic

ACKNOWLEDGMENTS

I would like to thank my parents for their encouragement and guidance throughout my life. I would like to thank Alejandro García for his patience and everything he taught me. I am very grateful to the highly capable staff at CENPA, including Greg Harper, Doug Will, John Amsbaugh, Dick Seymour, Erik Swanson, Barb Fulton, and Kate Higgins. I gratefully acknowledge the skillful machine work of Hank Simons, David Hyde, and Jim Elms. Seth Hoedl and Dan Melconian provided valuable assistance at various stages of my graduate studies. Thanks to Laura Stonehill, Noah Oblath, Michelle Leber, and Laura Bodine for being good-humored and helpful company in the office over the years. To the many more whom I have failed to acknowledge here, please accept my apologies. I would also like to thank the many friends I've made in Washington for all their support and the adventures we have shared. Finally, I feel compelled to acknowledge the unconditional love of my eternally neglected dog, Panama.

Chapter 1

PHYSICS MOTIVATION

1.1 In Brief

If a positive signal were observed from experiments searching for neutrinoless double-beta ($0\nu\beta\beta$) decay, the neutrino would be identified as its own anti-particle. In order to extract useful information beyond this important identification, a reliable description of the nuclear wave functions will be essential. For this reason, much work has gone into improving the accuracy of nuclear matrix element calculations for double-beta decay [44, 16, 82, 21, 71]. It is important to test theoretical models by requiring them to reproduce multiple observables that could be sensitive to similar operators. A few double-beta decay candidates, including ^{100}Mo, have the ground state of the intermediate nucleus with spin-parity $J^\pi = 1^+$. These nuclei allow measurements of single-beta decay rates in addition to the two neutrino double-beta ($2\nu\beta\beta$) decay rates to check calculations.

^{100}Mo offers a test system with up to seven constraints (see Figure 1.1), including measurements of the $2\nu\beta\beta$ decay rates to both the ground state and two excited states of ^{100}Ru, single-beta decay rates from the intermediate ^{100}Tc ground state to both the ground state and two excited states of ^{100}Ru, and the electron-capture (EC) rate from ^{100}Tc to ^{100}Mo. Excluding the highly suppressed $2\nu\beta\beta$ decay to the $J^\pi = 2^+$ excited state of ^{100}Ru, the EC rate is the most uncertain. A more accurate measurement of the EC rate provides an improved test for theoretical models.

Ejiri *et al.* [20] proposed to use ^{100}Mo as a detector for both $0\nu\beta\beta$ decay and solar neutrinos. For the latter, the efficiency for low-energy neutrino captures is determined by the same matrix element that drives the rate for the EC transition from ^{100}Tc to ^{100}Mo. The basic features of the detector can be found in Reference [20], which estimated that the amount of ^{100}Mo needed to perform a significant measurement would

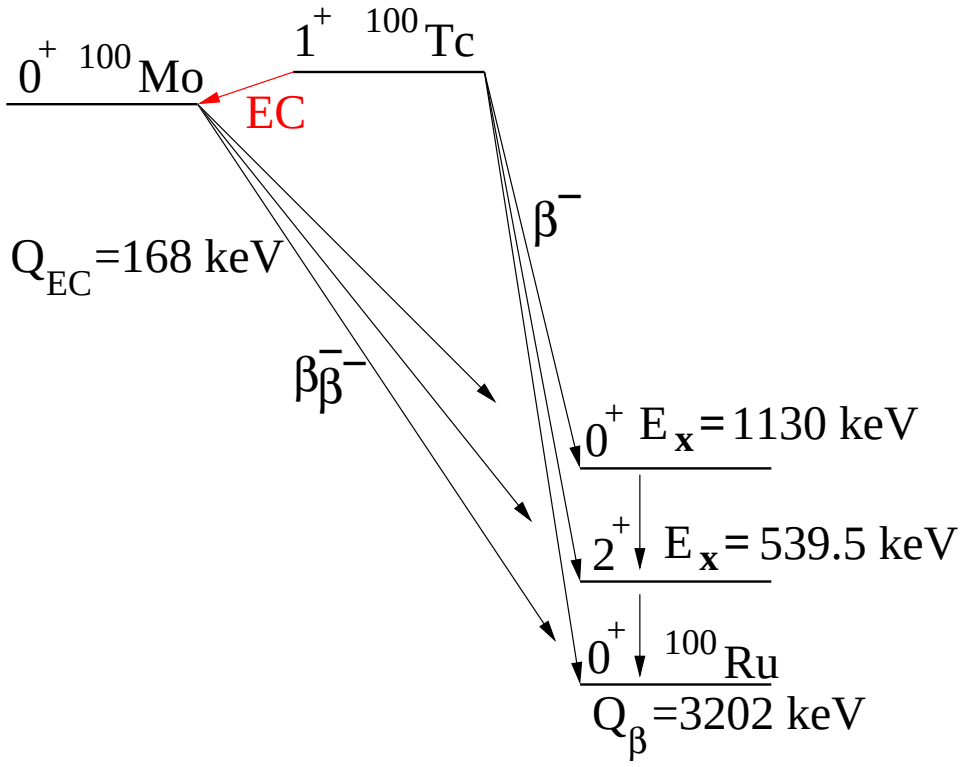

Figure 1.1: The $A = 100$ system and its seven observables: three β^- decays from ^{100}Tc to ^{100}Ru, three $2\nu\beta\beta$ decays from ^{100}Mo to ^{100}Ru, and the EC decay from ^{100}Tc to ^{100}Mo.

be 3.0×10^3 kg of ^{100}Mo (31×10^3 kg of natural Mo). Their calculation was based on an indirect determination of the strength for the transition:

$$B(\mathrm{GT};^{100}\,\mathrm{Mo} \rightarrow^{100}\,\mathrm{Tc}) = 3g_A^2|\langle^{100}\mathrm{Tc}||\sigma\tau||^{100}\mathrm{Mo}\rangle|^2 \tag{1.1}$$

deduced from a $^3\mathrm{He} +^{100}\,\mathrm{Mo} \rightarrow^3\,\mathrm{H} +^{100}\,\mathrm{Tc}$ measurement [2] which yielded:

$$B(\mathrm{GT})_{\mathrm{indirect}} = 0.52 \pm 0.06. \tag{1.2}$$

But it is also possible to determine the EC branch directly. A previous experiment measured the ^{100}Tc EC branch to be $(1.8\pm0.9)\times10^{-5}$, from which one obtains $B(\mathrm{GT};^{100}\,\mathrm{Mo} \rightarrow^{100}\,\mathrm{Tc}) = 0.66 \pm 0.33$, barely inconsistent with zero.

This document presents a more precise measurement of the EC branch and discusses its implications. The following sections of this chapter place these motivations in a broader context, then examine them in greater detail.

1.2 The Standard Model

It is human nature to seek explanations. An explanation generally leads to more questions. The ultimate goal of particle physics is to explain all observed phenomena with the simplest possible theory. The so-called "Standard Model," plus recent modifications due to discoveries about neutrinos, is the most complete theory we have to explain the universe. But the Standard Model requires many *ad hoc* constants and fails to incorporate gravity. Experiments that test the Standard Model offer clues toward a more complete theory.

The Standard Model of particle physics describes all known interactions besides gravity. The Standard Model includes twelve fermions which interact via both massive and massless mediating bosons, plus the Higgs boson, which gives all the other particles their masses. The twelve fermions include six quarks and six leptons. Leptons include the electron (e), the muon (μ), and the tau (τ), plus three corresponding neutrinos (ν_e, ν_μ, and ν_τ). The Higgs boson is the only particle in the Standard Model that has not been experimentally observed.

Fermions all have spin $s = \frac{1}{2}$ and interact by exchanging bosons with spin $s = 1$. Fermions interact via the electroweak interaction by exchanging photons and W^-, W^+, and Z bosons; only the quarks interact via the strong interaction by exchanging gluons.

Although it is the strongest known interaction, the strong interaction is not so readily apparent in our daily lives, because it is confined to atomic nuclei. Only the six quarks interact strongly by exchanging gluons. The strong interaction is responsible for the formation of protons, neutrons and nuclei. First u and d quarks, true particles in the Standard Model, are bound into protons and neutrons (both three quarks, uud and udd, respectively); then the residual strong force keeps the protons and neutrons bound as a nucleus via forces generated by meson (two-quark particle) exchange. The existence of stable, multiply-charged nuclei is sufficient to demonstrate the strength of the strong interaction: if the residual strong interaction were not strong enough to overcome the repulsion between the like charges of protons, no multiply-charged nuclei would exist and hydrogen would be the only element.

The electroweak interaction is broken into the weak interaction and the electromagnetic interaction at the energy scales that currently pervade the bulk of the observed universe and our daily lives. The weak interaction's apparent weakness is due to the fact that the interaction proceeds via the exchange of massive particles; at energies that are small compared the masses of these particles, its strength is proportional to $1/M^4$, where M is the mass of the W^-, W^+, or Z boson that mediates the interaction. Using units in which mass and energy are equal, then assuming an energy scale of 1 MeV (representative of Q values common in nuclear beta decay) and a mass $M \approx 100$ GeV (in the ballpark for the weak interaction's intermediate bosons) for simplicity, this results in a weak coupling that is smaller than the analogous electromagnetic coupling by a factor of $(Q/M)^4 = (1/10^5)^4 = 10^{-20}$. The electromagnetic interaction, the portion of the electroweak interaction that is stronger at ambient energies, is responsible for all of chemistry and the five human senses. For example, it is a combination of the sensitivity of the human eye and Rayleigh scattering, the law that describes how light scatters in the atmosphere, that makes the sky appear blue to us.

The charge-carrying W^- and W^+ allow the weak interaction to convert one strongly-bound nucleus into another. As a practical example, Carbon-14 (^{14}C) is created when cosmic-ray protons collide with nuclei in the earth's atmosphere and create secondary neutrons, which then collide with one of the nuclei in the nitrogen gas that composes 78% of the atmosphere. The subsequent reaction, $^{14}\mathrm{N}(n,p)^{14}\mathrm{C}$, creates small amounts of ^{14}C in the atmosphere. ^{14}C is unstable to the weak process of beta decay, with a half-life of 5700 years. Living plants absorb carbon dioxide from the atmosphere, which includes a small fraction (before the industrial revolution, between 180 and 300 ppm for hundreds of millenia) of carbon dioxide with ^{14}C. Only living plants absorb the ^{14}C from the atmosphere; thus the amount of ^{14}C decreases monotonically after the plant's death. The amount of ^{14}C present in fossils gives good estimates of their ages.

The Standard Model includes dozens of unexplained constants including, but not limited to, the masses and charges of the twelve fermions. Further observations and improved theories may explain the origins of these enigmatic numbers. The Standard Model is well documented. For brevity, this chapter will focus on the weak interaction and its relation to nuclear, particle, and astrophysics, in order to explain the relevance of the EC decay of ^{100}Tc to our understanding of the universe.

1.3 Neutrinos

The weak interaction and neutrinos have played an important role in the development of particle physics for the past century. Three types of decay radiation were discovered around the turn of the 20^{th} century. In a paper published in 1899, Rutherford first discovered two types of radiation from uranium which he called alpha and beta, based on different attenuation lengths observed when he covered a uranium source with thin aluminum sheets of varying thicknesses. Villard dubbed a third type of radiation gamma rays, which were observed to penetrate several feet of concrete. Further experiments by Rutherford, Pierre and Marie Curie, and others showed that the alpha particles were helium nuclei and the beta particles were electrons. Rutherford later showed that the gamma rays were electromagnetic radiation with a much shorter

wavelength than x rays.

The problem was that the beta radiation seemed to defy the cherished conservation laws of energy and momentum. If a nucleus at rest decays into two particles, for instance a daughter nucleus with mass M_f and a beta particle with mass m_e, then conservation of momentum implies that the two decay particles have the same momentum. The fixed amount of energy available to the decay uniquely determines this momentum,

$$p_e = \sqrt{\frac{(Q + M_f + m_e)^2 - M_f^2 - m_e^2}{2}}, \tag{1.3}$$

in which Q is the difference between the atomic masses of the parent and daughter nuclei. But experiments found that beta particles had continuous distributions of energy ranging from $E_e = m_e$ to $E_e = Q + m_e$. Either one of the conservation laws would need to be scrapped, or something was missing from the picture.

In 1930, in a letter to a conference which he was not able to attend, Pauli proposed that there could be a third particle emitted in the beta decays, carrying the missing energy and momentum. This particle had to be neutral to have evaded observation. Data indicated that its mass should be approximately equal to or less than the electron mass. Fermi published a theory of beta decay [29] in 1934, which included these light, neutral particles. Neutrons had already been discovered, so when asked whether his neutral particles were the same, Fermi added the Italian diminutive suffix to the neutron to dub the little mystery particles “neutrinos.”

The first-order formula from perturbation theory that describes beta-decay rates is still referred to as Fermi’s Golden Rule:

$$\Gamma_{i\to f} = \frac{2\pi}{\hbar} \int dE_f \frac{dN}{dE_f} |\mathcal{M}_{fi}|^2 \delta(E_f - E_i). \tag{1.4}$$

$\Gamma_{i\to f}$ is the rate of transition from the initial state i to the final state f. $\mathcal{M}_{fi}$ is the matrix element of the perturbative interaction between the intial and final state. The integral $\int dE_f \frac{dN}{dE_f} \delta(E_f - E_i)$, known as the “phase space integral,” takes into account the number of final state configurations available. Appendix A includes background on perturbation theory and Appendix B gives results of phase space integrals for some of the decay processes that will be discussed in this text.

Assuming the existence of the neutrino and treating both its mass and the daughter nucleus's recoil energy as negligible compared to nuclear beta-decay Q values, Equation 1.4 yields qualitative agreement with experimental data, without any knowledge of the microscopic form of the weak interaction. Neglecting the microscopic form of the interaction in the matrix element $\mathcal{M}_{fi}$ and approximating the nucleus as a point charge makes matters simpler. Under these assumptions, the energy spectrum of an electron from beta decay should have the form

$$\frac{d\Gamma}{dE_f} \propto F(Z, E_e) E_e p_e (E_0 - E_e)^2, \tag{1.5}$$

where the electron's momentum, energy, and maximum energy are p_e, E_e, and E_0, and $F(Z, E_e)$ is a correction for the Coulomb potential of a point charge with charge Z, the charge of the daughter nucleus.

This approximation is quite accurate for many beta-decay energy spectra. For example, Figure 1.2 shows a simulation of the beta-energy spectrum from ^{100}Tc for the 93% beta-decay branch to the ground state of ^{100}Ru. $F(Z, E_e)$ shifts the energy spectrum toward $E_e = m_e$ (zero kinetic energy), because the positively-charged nucleus creates a potential well for the outgoing electron. For β^+ decay, the correction is given by the same function but with the opposite charge, $F(-Z, E_e)$, which shifts the spectrum to higher energies.

Direct observation of the neutrino came twenty years later. In 1956, Cowan and Reines published the results of an experiment [70] that detected the neutrinos radiated from a nuclear reactor at Savannah River Plant in Georgia. Their detector was based on $CdCl_2$ dissolved in water. The high flux of anti-electron neutrinos from the reactor produced positrons and neutrons,

$$\bar{\nu}_e + p \rightarrow n + e^+, \tag{1.6}$$

then the positrons annihilated and produced two 511-keV photons. The neutrons were absorbed by the cadmium, which then emitted a γ ray:

$$n + {}^{108}\text{Cd} \rightarrow {}^{109}\text{Cd}^* \rightarrow {}^{109}\text{Cd} + \gamma. \tag{1.7}$$

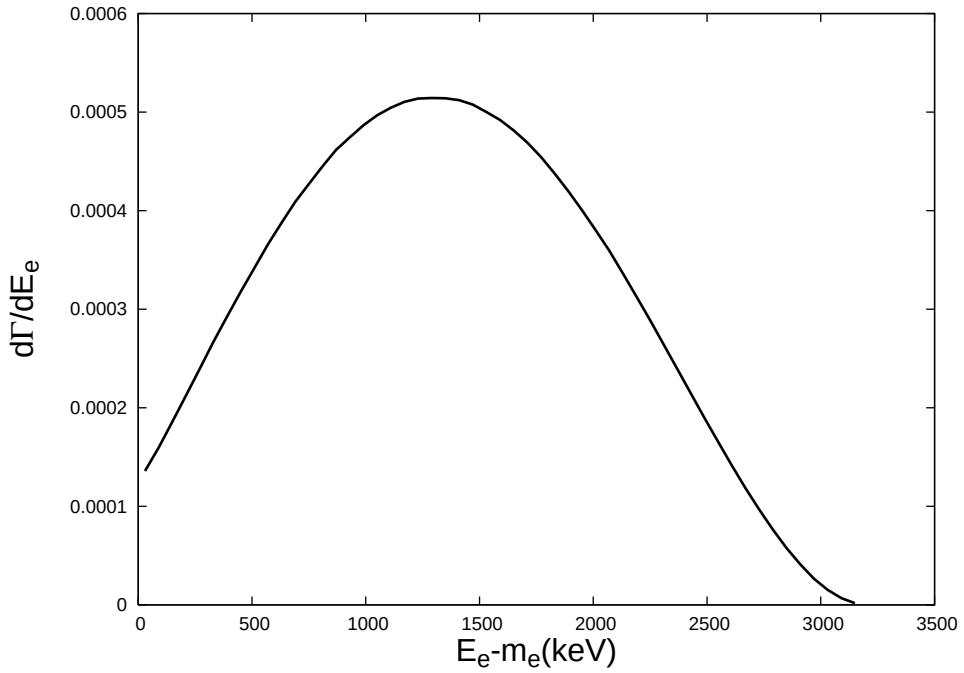

Figure 1.2: Simulated $Q = 3202$ keV beta-decay energy spectrum from ^{100}Tc to the ground state of ^{100}Ru.

Cadmium has a large neutron-absorption cross section and the three photons were all emitted within ≈ 5 μs. Direct observation of the coincidences between the two annihilation photons and the ^{109}Cd γ ray verified the neutrino hypothesis.

1.4 Parity Violation

Should the laws of nature change when viewed with a mirror? Until the latter half of the 1950s, the answer was thought to be no, based on guidance from the theory of electrodynamics. A change of parity, or spatial reflection, is mathematically equivalent to the transformation of a reflected image in the direction perpendicular to the plane of a mirror (see Figure 1.3). We denote a change of parity by the symbol Π, which is defined to invert coordinates:

$$\Pi : \vec{r} \Rightarrow -\vec{r}. \tag{1.8}$$

It follows that $\Pi^2 = 1$, which implies that there are only two possible eigenvalues for parity, ± 1. The fields of electrodynamics provide examples of these two possibilities: the electric field is a vector ($\Pi : \vec{E} \Rightarrow -\vec{E}$) and the magnetic field is a pseudovector, or axial vector ($\Pi : \vec{B} \Rightarrow \vec{B}$). Maxwell's Equations are invariant under a change of parity if we also transform the electric field and magnetic field accordingly. This invariance of the equations of motion means that all electromagnetic processes remain unchanged by inversion of the coordinates in the equation. Parity is conserved by electrodynamics.

In 1957, Wu *et al* [86] observed a correlation between the momenta of the beta particles from the decay of ^{60}Co and the polarization of the nucleus's spin. Expressing this mathematically, they found

$$\frac{d\Gamma}{d(\cos(\theta))} \propto 1 - cP\vec{s} \cdot \frac{\vec{p}_e}{E_e}, \tag{1.9}$$

in which c is a constant (for the nonce), $\vec{s}$ is spin of ^{60}Co, P is its polarization, and θ is the angle between $\vec{s}$ and $\vec{p}_e$. The beta particles were emitted preferentially opposed to the nuclear spin. This correlation is due to the weak interaction itself; that is, it comes from the modulus squared of the matrix element, $|\mathcal{M}_{fi}|^2$, in Equation 1.4. Consider

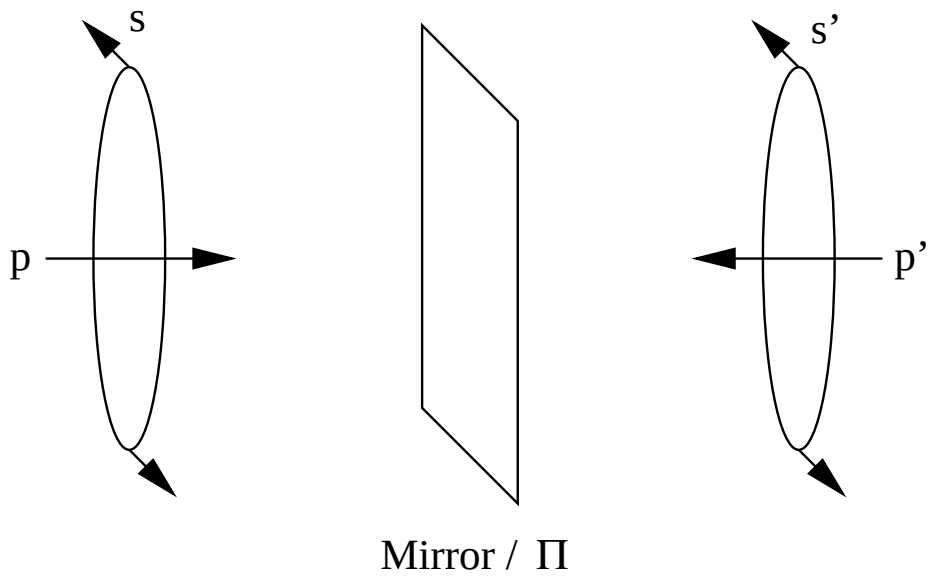

Figure 1.3: $\vec{p}$ and $\vec{s}$ (or $\vec{E}$ and $\vec{B}$) under parity: the momentum ($\vec{E}$) perpendicular to the plane of the mirror changes direction, but the spin $\vec{B}$ does not. By the right-hand rule, the spin is intitially opposed to the momentum, but in the same direction in the mirror image.

the effect of spatial reflection upon the angular correlation:

$$\Pi : \left(1 - cP\vec{s} \cdot \frac{\vec{p}_e}{E_e}\right) \Rightarrow \left(1 + cP\vec{s} \cdot \frac{\vec{p}_e}{E_e}\right). \tag{1.10}$$

The sign has changed on the dot product because $\vec{p}_e$ is a vector (like $\vec{E}$) and $\vec{s}$ is an axial vector (like $\vec{B}$). Spatial reflection reverses the correlation, so the beta particles would be emitted preferentially parallel to the nuclear spin. Figure 1.3 illustrates this reversal. Equation 1.9 would no longer be true: the spatial reflection of the left-hand side is achieved by substituting $\theta \Rightarrow \pi - \theta$, from which one would find

$$\frac{d\Gamma}{d(\cos(\theta))} \Rightarrow -\frac{d\Gamma}{d(\cos(\theta))} \propto -1 + cP\vec{s} \cdot \frac{\vec{p}_e}{E_e}, \tag{1.11}$$

which is not the same as the spatially reflected correlation in Equation 1.10. Thus we say that the weak interaction violates parity.

A more mathematical description is necessary to adequately describe the form of parity violation in the weak interaction and elucidate its consequences. First we consider quantum electrodynamics (QED). All conventions used for the γ matrices are

presented in Appendix C. In QED, the interactions between charged particles follow from a Lagrangian density,

$$\mathcal{L}_{\text{QED}} = \bar{\psi}(\gamma^\mu p_\mu - m)\psi - q\bar{\psi}(\gamma^\mu A_\mu)\psi - \frac{1}{4}F^{\mu\nu}F_{\mu\nu}, \tag{1.12}$$

in which $F^{\mu\nu}$ is given by

$$F^{\mu\nu} = p^\mu A^\nu - p^\nu A^\mu, \tag{1.13}$$

and A^μ is the vector field that represents photons. The first term on the right-hand side of Equation 1.12 is just the energy associated with a free particle of mass m. The third term describes the propagation of photons. Interactions are described by the second term, which can be suggestively written

$$\mathcal{L}_{\text{int}} = -J^\mu A_\mu, \tag{1.14}$$

in which $J^\mu = q\bar{\psi}\gamma^\mu\psi$ is the conserved vector current associated with the interacting charged particle. Noether's Theorem theorem states that the local gauge invariance of Equation 1.12 leads to conservation of charge. That is, because the Equation 1.12 remains unchanged when one substitutes

$$\psi \Rightarrow e^{iq\alpha(x)}\psi, \tag{1.15}$$

$$A^\mu \Rightarrow A^\mu - iq\partial^\mu\alpha(x), \tag{1.16}$$

it follows that

$$\partial_\mu q\bar{\psi}\gamma^\mu\psi = 0, \tag{1.17}$$

which states mathematically that charge is neither created nor destroyed. $\vec{E}$ and $\vec{B}$ can be expressed in terms of the components $(A^0, \vec{A})$ of A^μ,

$$\vec{E} = -\vec{\nabla}A^0 - \frac{\partial\vec{A}}{\partial t}, \tag{1.18}$$

$$\vec{B} = \vec{\nabla} \times \vec{A}, \tag{1.19}$$

then Maxwell's Equations follow from the Euler-Lagrange Equations applied to Equation 1.12 for the vector field,

$$\frac{\partial\mathcal{L}_{\text{QED}}}{\partial A^\mu} = \partial_\nu\frac{\partial\mathcal{L}_{\text{QED}}}{\partial^\nu A^\mu}. \tag{1.20}$$

Expressing the matrices in terms of their components, $\gamma^\mu = (\gamma^0, \vec{\gamma})$, the components of $\mathcal{L}_{\text{int}}$ are also invariant under a change of parity:

$$\begin{aligned} &\Pi : \gamma^0 A^0 \Rightarrow \gamma^0 A^0 \\ &\Pi : \vec{\gamma} \cdot \vec{A} \Rightarrow (-\vec{\gamma}) \cdot (-\vec{A}) = \vec{\gamma} \cdot \vec{A}. \end{aligned} \tag{1.21}$$

So $\mathcal{L}_{\text{int}} \propto (\gamma^0 A^0 - \vec{\gamma} \cdot \vec{A})$ is identical to its reflection. QED conserves parity.

The parity-violating correlation between the beta particles and the polarization of the ^{60}Co nuclei shows a preference for the vector, $\vec{p}_e$, based on the (pseudovector) spin angular momentum associated with the decaying nucleus, $\vec{s}$. The direction of a particle's spin with respect to its *own* momentum is referred to as its helicity,

$$\mathcal{H} = \frac{\vec{p} \cdot \vec{\sigma}}{|\vec{p}|}, \tag{1.22}$$

and any wave function can be decomposed into two components that are eigenstates of helicity,

$$\psi = \psi_+ + \psi_- = \frac{1 + \mathcal{H}}{2}\psi + \frac{1 - \mathcal{H}}{2}\psi. \tag{1.23}$$

Because $\mathcal{H}^2 = 1$, we have the two identities

$$\mathcal{H}\psi_\pm = \pm\psi_\pm. \tag{1.24}$$

$P_\pm \equiv (1 \pm \mathcal{H})/2$ are projection operators, because they project a general wave function into components that are eigenstates of helicity. The functional form of the projection operator P_- is reminiscent of the functional form of the spin-momentum correlation expressed in Equation 1.9. However, it it not possible to write a Lorentz-invariant interaction in terms of helicity states; for any massive particle, it is possible to perform a boost such that the momentum is reversed and $\psi_\pm \rightarrow \psi_\mp$.

The Lorentz-invariant projection operators with the same transformation properties under parity are referred to as the chiral projection operators:

$$\Pi : \frac{1 \pm \gamma_5}{2} \Rightarrow \frac{1 \mp \gamma_5}{2}. \tag{1.25}$$

The weak interaction can be represented by a current-current interaction between

fields, similar to the interaction term from the QED Lagrangian density in Equation 1.14,

$$\mathcal{L}_{\text{weak}} = \frac{G_F}{\sqrt{2}}(J_i)^\mu (J_j)_\mu, \tag{1.26}$$

in which i and j can refer to any two weak-interaction doublets. But now the parity-violating current projects only one chiral component from the fields; for example, the form of the lepton current for the (e, ν_e) doublet of beta decay is

$$J^\mu = \overline{e}(p_e)\frac{(1+\gamma_5)}{2}\gamma^\mu\frac{(1-\gamma_5)}{2}\nu(p_\nu), \tag{1.27}$$

in which $\overline{e}(p_e)$ represents the field creation operator for the beta particle, $\nu(p_\nu)$ represents the anti-neutrino field creation operator, and the projection operators $(1 \pm \gamma_5)/2$ pick the components of the fields preferred by the weak interaction. The projection operator next to $\overline{e}(p_e)$ has a different sign because the gamma matrices anticommute. To avoid confusion, all references to helicity will be made in terms of negative and positive *helicity*,

$$\frac{1-\mathcal{H}}{2}\psi = \psi_- \quad \text{and} \quad \frac{1+\mathcal{H}}{2}\psi = \psi_+, \tag{1.28}$$

and all references to chirality will be made in terms of left- and right-*handedness*,

$$\frac{1-\gamma_5}{2}\psi = \psi_L \quad \text{and} \quad \frac{1+\gamma_5}{2}\psi = \psi_R. \tag{1.29}$$

The projection operator $P_L = (1-\gamma_5)/2$ actually picks left-handed particles and right-handed *anti*particles (see Equation C.17). If we rearrange the matrices in Equation 1.27, leave the flavor of the current unspecified, and ignore a factor of 2, we can write a simplified form of the weak interaction current:

$$J^\mu = \bar{\psi}\gamma^\mu(1-\gamma_5)\psi. \tag{1.30}$$

The form of the weak current is referred to as $V-A$, because the first term transforms like a vector and the second term transforms like an axial vector. We call the weak current left-handed, because all observed weak processes (to date) involve only left-handed *particles* and right-handed *antiparticles*.

The ^{60}Co experiment that gave the first indication of parity violation had been performed based on suggestions from Lee and Yang, who posited scalar and tensor currents [59] for the weak interaction. Marshak and Sudarshan suggested a $V-A$ interaction current [80], based on mounting experimental evidence. In addition to the assumption of a universal $V-A$ current, Feynman and Gell-Mann proposed that the vector portion of the weak current could be conserved [30], in analogy with the vector current of QED. This hypothesis is known as Conservation of Vector Current (CVC). The CVC hypothesis explained why the value of G_F extracted from the Fermi (super-allowed, $J^\pi = 0^+ \rightarrow 0^+$, strictly vector current) β^+ decay of ^{14}O should agree so closely with the value extracted from the muon lifetime, τ_μ, based on a $V-A$ current. The two independent determinations of G_F agreed to within the experimental uncertainties at the time, which they explained by suggesting that the vector portion of the weak interaction current was not renormalized within the nuclear medium, just like that of QED.

The $V-A$ form of the weak interaction specifies that high-energy electrons from the pion decay sequence $\pi \rightarrow \mu \rightarrow e$,

$$\begin{aligned} \pi^- &\rightarrow \mu^- + \bar{\nu}_\mu \\ &\rightarrow e^- + \bar{\nu}_e + \nu_\mu + \bar{\nu}_\mu, \end{aligned} \tag{1.31}$$

must be emitted opposed to the muons. The pion has no spin. In the rest frame of the pion, conservation of angular momentum and momentum require that the muon and its antineutrino have equal and opposite momenta and spins. The muon antineutrino is highly relativistic and has positive helicity. Conservation of momentum then requires the muon to have positive helicity; given the chirality of the weak current, this is only possible because the muon mass mixes positive helicity in with the state of left-handed chirality. Now the muon decays and we consider only high-energy electrons, for which $E_e \gg m_e$. The high-energy, left-handed electron has negative helicity. If the electron has the largest momentum of the decay products, then the two neutrinos must both go in the same direction, opposite to that of the electron, to conserve momentum. But the neutrino and antineutrino are both highly relativistic and have opposite he-

licities. Because of this, the only way to conserve angular momentum from the muon's decay is for the electron to have its spin in the same direction as the muon's spin. But for the reasons explained above, the muon has positive helicity and the electron has negative helicity. Therefore the two must go in opposite directions.

Neglecting radiative corrections, the $V - A$ form of the weak interaction predicts the branching ratio for the two modes of pion decay:

$$\frac{\Gamma(\pi^- \to e^- + \bar{\nu}_e)}{\Gamma(\pi^- \to \mu^- + \bar{\nu}_\mu)} = \frac{m_e^2}{m_\mu^2} \frac{(1 - m_e^2/m_\pi^2)}{(1 - m_\mu^2/m_\pi^2)} = 1.30 \times 10^{-4}, \tag{1.32}$$

which disagreed with the experimental results available in the late 1950s, but has since been verified. Note that the phase space is larger for the smaller mass of the electron, but the muon decay channel dominates because of enhancement proportional to the muon mass squared. This enhancement occurs because, as described for $\pi \to \mu$ above, combined conservation of angular momentum and momentum require the lepton and neutrino to have the same helicities. The amount of positive helicity in a left-handed lepton wave function is proportional to the lepton's mass. Appendix D presents a calculation of this branching ratio and explains the proportionality to the lepton mass.

Parity violation raises interesting questions. Why should the weak interaction exclusively create particles of one chirality? This could be compared to an imaginary world where all people are born left-handed. This preference is just a feature of the theory for the moment. It is worth noting that chirality is present elsewhere in nature. All the nucleotides that compose DNA are right-handed optical isomers and it is this right-handedness that leads to the double-helix structure of DNA. We are all genetically "right-handed"; there could just as well be another world full of genetically "left-handed" people.

1.5 Hadronic Complications

The hadrons in semileptonic beta decay provide a source of complication due to misalignment between quark eigenstates, the intrinsic structure of protons and neutrons, and the many-body system of the nucleus. It can be viewed as a lucky coincidence

that the CVC hypothesis initially worked so well to explain the agreement between the value of G_F determined from the superallowed β^+ decay of ^{14}O and the value extracted from the muon lifetime, since the quark eigenstates that participate in the weak interaction are not perfectly aligned with the quark mass eigenstates. Nuclear beta-decay rates are suppressed by this misalignment.

Nuclear beta decay involves the (u, d) quark doublet, so the coefficient that accounts for the misalignment between the mass eigenstates and the weak eigenstates for quarks in nuclear beta decay is called V_{ud}. The misalignment between the mass eigenstates and weak eigenstates across all three generations of quarks is described by a matrix, known as the CKM matrix:

$$\begin{pmatrix} V_{ud} & V_{us} & V_{ub} \\ V_{cd} & V_{cs} & V_{cb} \\ V_{td} & V_{ts} & V_{tb} \end{pmatrix} \begin{pmatrix} |d\rangle \\ |s\rangle \\ |b\rangle \end{pmatrix} = \begin{pmatrix} |d'\rangle \\ |s'\rangle \\ |b'\rangle \end{pmatrix}. \tag{1.33}$$

This matrix operates on the mass eigenstates $(|d\rangle, |s\rangle, |b\rangle)^T$ to give the weak eigenstates $(|d'\rangle, |s'\rangle, |b'\rangle)^T$. The agreement between G_F from superallowed nuclear beta decays and muon decay would have been rather poor if V_{ud} were farther from unity. Because $V_{ud} \approx 0.974$, there was apparent agreement, but there is no *a priori* reason why V_{ud} should be so close to unity.

The CKM matrix should be unitary if there are only three generations of quarks and the weak interaction features only left-handed currents. Departures from unitarity could signal right-handed weak currents or the existence of more quarks. The measurement of V_{ud} is important because it can be used in conjunction with measurements of V_{us} and V_{ub} (obtained from K and B meson branch measurements, respectively) to test whether the first row satisfies unitarity, that is, to see if $|V_{ud}|^2 + |V_{us}|^2 + |V_{ub}|^2 = 1$. The set of all precisely measured superallowed nuclear beta decays currently yields the most precise value of V_{ud}, which is only possible because the nuclear beta-decay vector coupling, G_V, is constant to a few parts in 10^4. To emphasize the complications associated with the hadronic processes, we note that such a precise determination of G_V and subsequently V_{ud} [42] is only possible with carefully-calculated isospin-symmetry-

breaking corrections and nuclear-structure dependent radiative corrections.

Another example of nuclear complications comes from the CVC hypothesis, which predicts a shift in beta-decay energy spectra for transitions that are analogous to $M1$ electromagnetic transitions in nuclei. The electromagnetic interaction of an $M1$ transition has the form

$$-i\frac{\mu e}{2M}\sigma^{\mu\nu}A_\mu q_\nu T_z, \tag{1.34}$$

in which $\sigma^{\mu\nu} = (i/2)[\gamma^\mu\gamma^\nu - \gamma^\nu\gamma^\mu]$, μ is the magnetic moment of the transition, q_ν is the four-momentum of the photon, and $T_z = \sum_i \tau_z(i)$ is the total z component of the isospin. By the CVC hypothesis, the analogous weak interaction matrix elements are determined by substituting $T_z \rightarrow T_\pm$ and $A_\mu \rightarrow J_\mu(q_\nu)$, such that the electromagnetic vector field becomes the weak lepton current. The isospin-rotated analog of the $M1$ transition is observable for certain Gamow-Teller tansitions. Since the isospin rotation is equal and opposite for β^+ versus β^- decays, the form of the correction is equal and opposite for β^+ versus β^- decays. Gell-Mann predicted the magnitude of the effect based on a measured $M1$ γ-ray intensity in ^{12}C and suggested a measurement [38] of two mirror beta decays to the ground state of ^{12}C, the β^- decay of ^{12}B and the β^+ decay of ^{12}N, so that additional corrections and systematic errors could be avoided. This effect, known as the weak magnetism, was subsequently observed.

Whereas $g_A = g_V = G_F$ for the leptonic portion of the weak current, leading to the relative simplicity of the $V - A$ current as expressed in Equation 1.30, the hadronic portion of the weak current takes a more complicated form. The weak magnetism is just one of several possible recoil-order currents. Writing the most general Lorentz-invariant, $V - A$ form of the hadronic current for the simplest beta-decay process, neutron beta decay, we find

$$\langle p(p')|J^\mu|n(p)\rangle = \overline{p}(p')\Big[f_1\gamma^\mu - i\frac{f_2}{m_n}\sigma^{\mu\nu}q_\nu + \frac{f_3}{m_n}q^\mu - g_1\gamma^\mu\gamma_5 + i\frac{g_2}{m_n}\sigma^{\mu\nu}\gamma_5 q_\nu - \frac{g_3}{m_n}\gamma_5 q^\mu\Big]n(p). \tag{1.35}$$

CVC implies $f_1 = 1$, $f_2 = (\mu_p - \mu_n)/2$, and $f_3 = 0$. μ_p and μ_n are anomalously large because of the strong interaction. Complications due to the strong interaction also result in a change from $g_1 = 1$ to $g \approx 1.25$ in light nuclei. g_2 and g_3 are generally small,

but not necessarily zero. The point is that compared to the simplicity of Equation 1.30, even the simplest weak process involving hadrons includes the added complication of the renormalization of g_1. The interaction current becomes more complicated because the (u, d) quark doublet that participates in the weak interaction is bound inside the hadron. Nuclei are more complex, with multiple neutrons and protons, and all the complications associated with the many-body problem. Calculations of matrix elements for large nuclei can be very difficult. Studies of the weak interaction using neutrons offer some advantages due to the fact that the neutron is the simplest hadron. Chapter 6 includes a calculation of the contributions of all the recoil-order hadron currents to the correlation between the decay proton's momentum and the decaying neutron's spin.

1.6 Massive Neutrinos

Neutrinos were originally assumed to be massless. It is now widely accepted that there are at least two non-zero neutrino masses. The mass eigenstates, by which free neutrinos propagate, are not exactly the same as the weak eigenstates by which they interact. This situation is analogous to that of the quarks and the CKM matrix discussed in the previous section.

What began as efforts to study solar processes using neutrinos evolved into studies of neutrinos using the sun. Non-zero neutrino masses answered a great puzzle that emerged from efforts to study solar neutrinos. Beginning with measurements [68] pioneered by Ray Davis at the Homestake Mine in Lead, South Dakota, several experiments over the course of decades observed a large deficit in the neutrino flux from the sun, when compared with the flux expected from calculations. The Homestake Experiment detected solar neutrinos using a 100,000 gallon tank of perchloroethylene (C_2Cl_4) in the Homestake mine, nearly a mile underground. Neutrinos produced by fusion in the sun, with energies greater than the threshold of $E_\nu = 814$ keV, would cause the reaction

$$\nu_e + {}^{37}\text{Cl} \rightarrow e^- + {}^{37}\text{Ar}. \tag{1.36}$$

The argon produced by this reaction was captured by periodically bubbling helium gas

through the tank. The experiment measured approximately one third of the flux expected from solar models. The results from both experiment and theory were rechecked and the disagreement persisted. The recurring puzzle of the missing flux, known as the "solar neutrino problem," was solved by the physics of massive neutrinos.

The explanation for the missing electron neutrinos was that they had oscillated into other types of neutrinos. Consider the matrix in Equation 1.33 again, but imagine that it applies to neutrinos instead. We refer to the elements of the neutrino-mass-mixing (MNS) matrix as $U_{\alpha i}$; the mass eigenstates are denoted by $i = 1, 2, 3$, with ν_i having mass m_i, while the flavor eigenstates are denoted by the subscript $\alpha = e, \mu, \tau$, corresponding to the three weak lepton doublets. This section uses notation in which $\hbar = c = 1$ for simplicity. An electron neutrino created by fusion is a superposition of the three mass eigenstates,

$$|\nu_e\rangle = U_{e1}|\nu_1\rangle + U_{e2}|\nu_2\rangle + U_{e3}|\nu_3\rangle. \tag{1.37}$$

After creation, each mass component of the neutrino propagates according to

$$|\nu_i(t)\rangle = e^{-im_i\tau}|\nu_i\rangle, \tag{1.38}$$

in which m_i is the mass of ν_i and τ is its proper time. In the lab frame, the phase for each mass eigenstate is given by

$$\phi_i = m_i\tau = Et - px, \tag{1.39}$$

and to determine the observable oscillation probabilities it is necessary to evaluate the relative phases,

$$\delta\phi_{ij} = \phi_i - \phi_j = (E_i - E_j)t - (p_i - p_j)x. \tag{1.40}$$

If the neutrino interacts at distance L, we can assume that the time is given by the distance divided by the average velocity of the two mass components $T = i(E_i + E_j)L/(p_i + p_j)$. Corrections to this approximation only enter at $\mathcal{O}([(m_i^2 - m_j^2)^2/E^2]^2)$ [61]. Then one finds

$$\delta\phi_{ij} = \left(\frac{E_i^2 - E_j^2}{p_i + p_j} - \frac{p_i^2 - p_j^2}{p_i + p_j}\right) L \approx \left(\frac{m_i^2 - m_j^2}{2E}\right) L, \tag{1.41}$$

where the approximation $\bar{p} = E$ has been used in the last step. So for each mass eigenstate, we multiply by a relative phase at distance L,

$$|\nu_i(L)\rangle = e^{-i(m_i^2/2E)L}|\nu_i\rangle, \tag{1.42}$$

and substitute these relative phases into Equation 1.37 for two flavors, α and β. The probability for a neutrino created with flavor α to interact with flavor β depends on the distance from its source:

$$\begin{aligned} P(\nu_\alpha \to \nu_\beta) = &\quad |\langle\nu_\beta(L)|\nu_\alpha(L)\rangle|^2 \\ = &\quad \delta_{\alpha\beta} - 4\sum_{i>j} \mathbf{Re}(U^*_{\alpha i}U_{\beta i}U_{\alpha j}U^*_{\beta j})\sin^2[1.27\Delta m^2_{ij}(L/E)] \\ &\quad +2\sum_{i>j} \mathbf{Im}(U^*_{\alpha i}U_{\beta i}U_{\alpha j}U^*_{\beta j})\sin[2.54\Delta m^2_{ij}(L/E)]. \end{aligned} \tag{1.43}$$

The coefficients 1.27 and 2.54 are derived from reinsertion of $\hbar$ and c, with $\Delta m^2_{ij} \equiv m^2_i - m^2_j$ in units of eV^2, L in km, and E in GeV. The important feature of this equation is that a mass difference Δm^2_{ij} and an energy E_ν determine the length scale L over which neutrino oscillations are observable.

Matter effects are also important for the description of neutrino oscillations. Dubbed the MSW effect for Mikheyev, Smirnov, and Wolfenstein, charged-current interactions within matter affect only electron neutrinos and alter the components of the MNS matrix that couple to electron neutrinos. Because of high densities of electrons in the interior of the Sun (or Earth), electron neutrinos gain an effective mass, similar to light in a medium with a high index of refraction. The effective mass of the electron neutrinos is proportional to the density of electrons in the medium. Assuming that the electron neutrino in vacuum involves two components, a large amplitude of a light component $|\nu_L\rangle$ and a smaller amplitude of a heavy component $|\nu_H\rangle$, for high values of the electron density it is possible for the electron neutrino's effective mass to correspond to the mass of the heavy neutrino, such that $m_{\nu_e}(\rho_e) \sim m_H$ and $|\nu_H(\rho_e \to \infty)\rangle \sim |\nu_e\rangle$. If the electron neutrino is created in a high-density medium, like the interior of the sun, and it propagates through the medium to lower electron densities adiabatically, then it can emerge as a heavy neutrino at the low-density exterior. The heavy neutrino results in flavor change if, for oscillation into muon neutrinos, $|\nu_H(\rho_e \to 0)\rangle \sim |\nu_\mu\rangle$.

Adiabaticity of the level crossing requires that the density of the Sun be smooth on the scale of the neutrino oscillation length. These matter-enhanced neutrino oscillations offer an explanation of the missing solar neutrinos, even if the mixing angles in the MNS matrix are too small for vacuum oscillations to explain the missing neutrino flux.

Apparently, the missing neutrinos changed flavor. Recently, measurements [18] from the Sudbury Neutrino Observatory (SNO) experiment confirmed this answer, by measuring the total neutrino flux of all flavors using neutral current detectors (NCDs). The SNO experiment measured the neutrons generated when solar neutrinos (of any flavor) inelastically scattered from deuterons by exchange of neutral Z bosons, breaking the deuterons into their constituent neutrons and protons. The neutrons were then detected in the ^{3}He-filled NCDs, which detected the 764 keV released to the p and ^{3}He from the reaction $^3\mathrm{He}(n,p)^3\mathrm{H}$. The NCD measurements agreed with the predicted ^{8}B neutrino flux, confirming that approximately 2/3 of the ^{8}B neutrinos created in the sun reach the Earth with a different flavor.

Another piece of information about (and in fact, the first signal for) massive neutrinos came from atmospheric neutrinos created by cosmic rays. For cosmic rays with energies ≤ 1 GeV, pions and kaons created by cosmic rays subsequently decay into muons then electrons before reaching the surface of the earth. For the decay chain $\pi^{\pm} \rightarrow \mu^{\pm} \rightarrow e^{\pm}$, one expects two muon neutrinos and one electron neutrino (see Equation 1.31). Detection of the ratio of atmospheric neutrinos, differing from the expected ratio of muon to electron neutrinos of $N_{\nu_\mu}/N_{\nu_e} \approx 2$, has provided a probe for another set of neutrino mass parameters. In this case, the oscillation is observed for distances between zero and the diameter of the Earth, with different oscillation parameters as a function of the neutrino's zenith angle and energy. Incoming neutrinos can inelastically interact to produce muons or electrons, depending on the neutrino's flavor. The muons and electrons produce Cerenkov radiation, which leaves a signal for the incoming neutrino's flavor and direction. A direction-dependent deficit in muon neutinos is observed. Once again, the deficit can be explained by flavor change, but this time the neutrinos are posited to have changed into tau neutrinos, which lack enough energy to produce the much heavier τ particle. Whereas the solar-neutrino mixing described

yielded information about neutrinos at energies $E_\nu \approx 5 - 15$ MeV for a mass difference $\Delta m^2_{12} \sim 8 \times 10^{-5}$ eV^2 from the Sun, observations of atmospheric neutrinos at energies ≤ 1 GeV indicate $\Delta m^2_{23} \sim 2 \times 10^{-3}$ eV^2. The two mass differences allow two possible arrangements of neutrino masses for three generations of neutrinos.

Neutrino oscillations have yielded information about neutrino mass differences and mixing angles. It is also possible to directly measure the mass expectation value of the electron neutrino by careful measurements of low-energy beta decays. The Karlsruhe Tritium Neutrino (KATRIN) experiment aims to probe the electron neutrino mass by carefully analyzing the beta-energy spectrum near the endpoint of tritium beta decay, with projected sensitivity to a neutrino mass as low as 0.2 eV. Such a measurement would fix the absolute scale of the neutrino masses.

The MNS matrix is of great interest, but determining its properties presents challenges. In addition to being characterized by mixing angles, there could also be CP-violating phases. These CP-violating phases could help explain the matter-antimatter asymmetry of the universe. Double-beta decay, which is described in the next section, could lead to observations of two possible CP-violating phases in addition to the one that could be observed by the conjugate neutrino oscillations $\nu_e \rightarrow \nu_\mu$ and $\bar{\nu}_\mu \rightarrow \bar{\nu}_e$. Should the MNS matrix fail to be unitary, it might indicate a fourth generation of neutrinos. The prospect of unknown neutrinos is interesting because of the roles they would play in the missing mass of the universe and a host of astrophysical processes [45]. We now turn to double-beta decay, which holds the potential to probe neutrino mass, lepton number conservation, CP violation, and right-handed weak currents all at once.

1.7 Double-Beta Decay

While the existence of non-zero neutrino masses is now established, the fundamental nature of the neutrino is still an open question. It cannot be excluded at present that the neutrino could be its own anti-particle. This is a conspiracy between the chirality of the weak interaction and the fact that the neutrino carries no charge. If the neutrino

carried charge, then its antiparticle would have to carry the opposite charge. Furthermore, were the weak interaction parity-conserving, the rarity of $0\nu\beta\beta$ decay would already exclude the neutrino being its own antiparticle. But the parity-violating structure of the weak interaction allows the nature of the neutrino to remain ambiguous for the moment. We now explore how double-beta decay might resolve this issue.

The process of $0\nu\beta\beta$ decay is only possible if the neutrino is its own antiparticle. For instance, $0\nu 2\beta^-$ decay can be considered in terms of two virtual interactions,

$$n \rightarrow p + e^- + \bar{\nu}_e, \tag{1.44}$$

$$\text{followed by} \qquad \nu_e + n \rightarrow p + e^-. \tag{1.45}$$

in which the neutrino produced as an antiparticle in the first virtual interaction must act as a neutrino for the second virtual interaction. This process violates conservation of lepton number. Even if we assume that the neutrino and antineutrino are identical, the chirality of the weak interaction forbids $0\nu\beta\beta$ if the neutrino is massless. The first virtual reaction produces a right-handed antineutrino. There will be zero overlap between the left-handed neutrino required for the second virtual transition and the right-handed neutrino produced in the first if the neutrino is massless.

Before discussing $0\nu\beta\beta$ decay in more detail, it is worth reviewing its well-established relative, $2\nu\beta\beta$ decay. Experiments searching for $0\nu\beta\beta$ decay naturally measure $2\nu\beta\beta$ decay in the process. $2\nu\beta\beta$ decays are among the rarest phenomena that have been observed in nature. We can attribute the rarity of these decays to the fact that they are described by a second-order perturbation in the weak interaction. Given the value of G_F,

$$G_F \approx \frac{10^{-5}}{m_p^2}, \tag{1.46}$$

in which m_p is the proton mass, and the neutron lifetime,

$$\tau_n \approx 900 \text{ s}, \tag{1.47}$$

which will serve as the canonical beta-decay lifetime, we make a rough estimate of double-beta decay lifetimes. Consider the $2\nu\beta\beta$ decay diagram shown on the left side

Table 1.1: Selected $2\nu\beta\beta$ decay half-life measurements from Reference [25]

Isotope	$T^{2\nu}_{1/2}$ (years)
^{76}Ge	$(1.7 \pm 0.2) \times 10^{21}$
^{82}Se	$(10.3 \pm 0.8) \times 10^{19}$
^{100}Mo	$(7.3 \pm 0.4) \times 10^{18}$
^{116}Cd	$(2.9 \pm 0.4) \times 10^{19}$
^{150}Nd	$(6.8 \pm 0.7) \times 10^{18}$

of Figure 1.4. It contains two vertices which each yield a factor of G_F^2, so overall there is an extra factor of G_F^2 compared to single-beta decay. To make this constant dimensionless, a factor of Q^4 is necessary. Assuming $Q = 1$ MeV, the rate should be suppressed compared to single-beta decay by a factor of $|G_F|^2 Q^4 \approx 10^{-22}$, from which one would guess a lifetime

$$\tau_{2\nu\beta\beta} \approx 10^{22} \tau_n \approx 10^{18} \text{ years}. \tag{1.48}$$

Actual lifetimes tend to be longer, primarily because the four free final-state particles of $2\nu\beta\beta$ put it at a disadvantage in terms of phase space. Nuclear matrix elements must be less than unity, so they will tend to increase lifetimes too. Table 1.1 shows some $2\nu\beta\beta$ half-lives that have been experimentally measured.

These lifetimes are large compared to the estimated age of the universe since the big bang, $t_0 \approx 14 \times 10^9$ years [47]. How can such a rare process be observed? Nuclear physics provides several possibilities. For a given mass number A, neighboring nuclei with even numbers of both neutrons ($N = A - Z$) and protons (Z), known as "even-even" nuclei, often both have lower ground-state energies than the intermediate odd-odd nucleus. This recurring arrangement can be explained by the nuclear pairing phenomenon. Even-even nuclei always have ground state spin zero; like nucleons form pairs with net angular momentum zero, minimizing the magnetic moment of the nucleus and resulting in a lower ground-state energy. Because the intermediate nu-

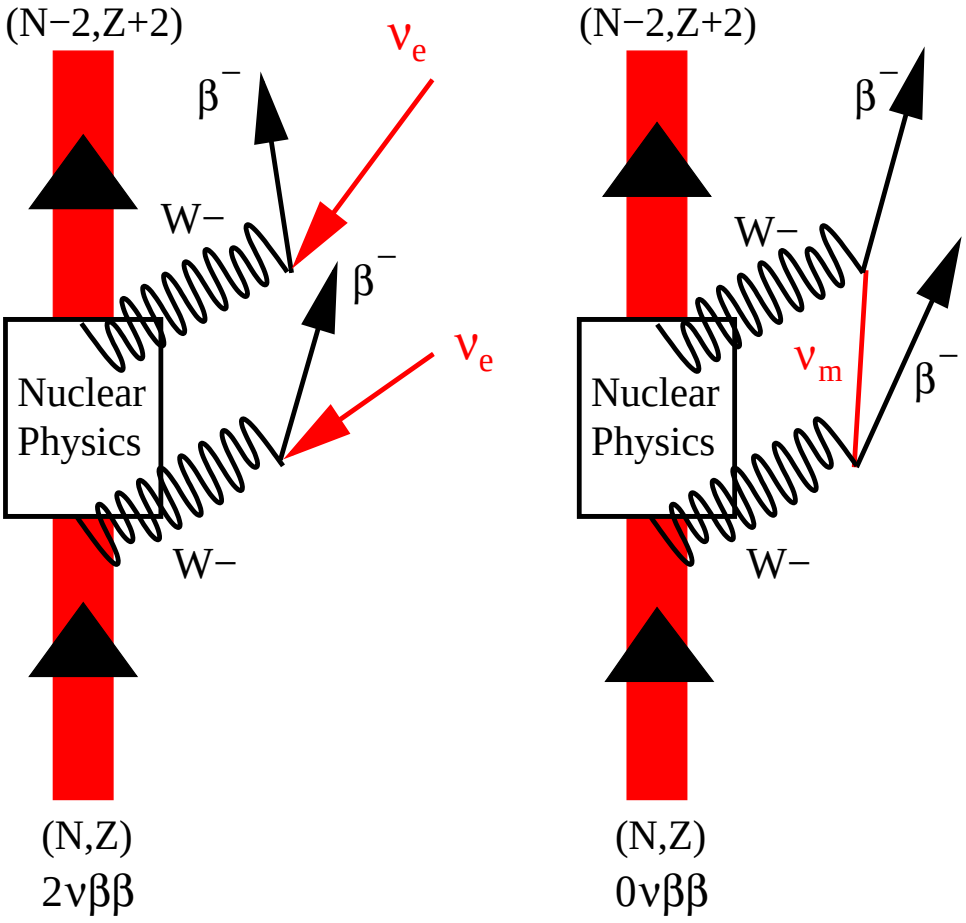

Figure 1.4: Diagram for $2\nu\beta\beta$ decay (left) and $0\nu\beta\beta$ decay (right). Calculations for the $0\nu\beta\beta$ process are much more complicated because of the loop created by the Majorana neutrino, ν_m

cleus has a higher energy, the even-even parent nucleus is not susceptible to first-order beta decay. Double-beta decay is the mechanism which connects the higher energy, or mother, even-even nucleus with the lower energy, or daughter, even-even nucleus. See Figure 1.1 for the $A = 100$ example of this scenario.

Without the stability of the parent isotope with respect to single-beta decay in these double-beta decay scenarios, the detection of double-beta decay would be more difficult. Even with the relative stability of the parent isotopes, double-beta decay experiments seeking to place limits on or detect $0\nu\beta\beta$ decay must employ sophisticated background-reduction techniques, including the placement of experiments deep underground to shield them from cosmic radiation, high-purity fabrication techniques for detector components, and techniques to refine discriminating power such as segmented detectors and pulse-shape analysis (for example, see Reference [1]). There is much ongoing experimental effort toward measurements of double-beta decays, aiming to eventually exclude or observe the neutrinoless mode.

For $2\nu\beta\beta$ decay, the decay rate can be obtained from Equation 1.4 with $\mathcal{M}_{fi}$ given by

$$\mathcal{M}_{fi} = \sum_m \frac{\langle {}^{100}\mathrm{Ru}|V|{}^{100}\mathrm{Tc}^m\rangle\langle {}^{100}\mathrm{Tc}^m|V|{}^{100}\mathrm{Mo}\rangle}{M_{\mathrm{Mo}} - E_{\beta 1} - E_{\bar{\nu}_e 1} - E_{\mathrm{Tc}^m}}, \tag{1.49}$$

where the sum is over all states of the intermediate nucleus, in our case ^{100}Tc. We have written the decay rate in terms of the $A = 100$ system, but an analogous formula applies very generally to systems that exhibit double-beta decay. The only allowed transitions to first order in the weak current are Gamow-Teller decays, in which $V \propto \tau^+\sigma^+$, so that transitions to states in the intermediate nucleus other than the 1^+ states are suppressed by selection rules for isospin and spin. Additionally, the contributions from the excited states of the intermediate nucleus will be suppressed by the growing denominator in Equation 1.49. For these reasons, the single-state dominance (SSD) hypothesis [24] suggests that for $2\nu\beta\beta$ decays in which the intermediate nucleus has a ground state with spin-parity $J^\pi = 1^+$, the single-beta transitions involving the ground state of the intermediate nucleus dominate the total $2\nu\beta\beta$ decay rates. There is no special reason to expect the SSD hypothesis to be exactly true, but any destructive

interference between the 1^+ excited states of the intermediate nucleus would enhance the dominance of the intermediate nucleus's ground state in addition to the enhancement due its smaller energy denominator. In the context of the SSD hypothesis, the EC branch of the intermediate nucleus is very important, because it also determines the matrix element for the first virtual transition in Equation 1.49. To the extent that SSD is satisfied, it can be used to predict $2\nu\beta\beta$ decay rates to excited states of the daughter nucleus that have not been measured.

Now we discuss the mechanisms that would give rise to $0\nu\beta\beta$ decay at a more technical level. Consider the diagram for $0\nu\beta\beta$ decay on the right-hand side of Figure 1.4. The first vertex in the $0\nu\beta\beta$ decay corresponds to the standard weak electron current, like the one given in Equation 1.27 during the discussion of parity violation. The second vertex, however, requires the neutrino to interact as an antineutrino. Such a neutrino is called a Majorana neutrino, because Ettore Majorana first explored the possibility that neutrinos could be their own antiparticles. These neutrinos arise in various grand-unification theories and supersymmetric extensions to the Standard Model. In terms of the Lagrangian density, such an interaction would require mass terms that look like

$$\mathcal{L}_M \propto M_L[\bar{\psi}_L^c \psi_L + \bar{\psi}_L \psi_L^c] + M_R[\bar{\psi}_R^c \psi_R + \bar{\psi}_R \psi_R^c], \tag{1.50}$$

compared to Dirac mass terms of the form

$$\mathcal{L}_M \propto M_D[\bar{\psi}_R \psi_L + \bar{\psi}_L^c \psi_R^c]. \tag{1.51}$$

The mass terms of Equation 1.50 are forbidden for all other known fermions because they violate conservation of charge.

The amplitude for the lepton portion of the $0\nu\beta\beta$ decay matrix element for a Majorana neutrino of mass m_ν is

$$l^{\rho\sigma} \propto \int d^4 p_\nu e^{-i\vec{p}_\nu \cdot (\vec{x}-\vec{y})} \bar{e}(\vec{x}) \gamma^\rho (1-\gamma_5) \frac{\not{p}_\nu + m_\nu}{p_\nu^2 - m_\nu^2} (1-\gamma_5) \gamma^\sigma e(\vec{y}), \tag{1.52}$$

where the integral is over the virtual neutrino's four-momentum p_ν and $e(\vec{y})$ and $\bar{e}(\vec{x})$ represent the first and second electron-creation operators. Only the neutrino mass can contribute to this decay amplitude, which follows from the anticommutation of the

gamma matrices. If we move the projection operator on the left through the neutrino propagator, the $\not{p}_\nu$ term changes the sign in front of γ_5 and the product of the projection operators on the right becomes $(1+\gamma_5)(1-\gamma_5) = 0$. The mass term involving m_ν, on the other hand, does not change the projection operator and the product on the right is $(1-\gamma_5)(1-\gamma_5) = 2(1-\gamma_5)$; thus the decay amplitude is directly proportional to the neutrino mass.

The denominator in Equation 1.52 can be rewritten and factored:

$$p_\nu^2 - m_\nu^2 = E_\nu^2 - |\vec{p}_\nu|^2 - m_\nu^2 = (E_\nu - \sqrt{|\vec{p}_\nu|^2 + m_\nu^2})(E_\nu + \sqrt{|\vec{p}_\nu|^2 + m_\nu}). \tag{1.53}$$

The integral over E_ν leaves only the residue $1/\sqrt{|\vec{p}_\nu|^2 + m_\nu^2}$, ignoring multiplicative constants, so the amplitude takes the form

$$l^{\rho\sigma} \propto \int d^3\vec{p}_\nu e^{-i\vec{p}_\nu\cdot(\vec{x}-\vec{y})}\bar{e}(\vec{x})\gamma^\rho \frac{m_\nu}{\sqrt{|\vec{p}_\nu|^2 + m_\nu^2}}(1-\gamma_5)\gamma^\sigma e(\vec{y}). \tag{1.54}$$

This form shows explicitly that $0\nu\beta\beta$ decay amplitudes are proportional to m_ν/E_ν. An average nucleon-nucleon separation of 2 fm implies, via the uncertainty principle, an average neutrino momentum of $\langle|\vec{p}_\nu|\rangle \sim 100$ MeV. For light neutrinos (corresponding to the scale of the Δm_{ij}^2s observed from neutrino oscillations as described in Section 1.6), this implies $m_\nu^2 \ll |\vec{p}_\nu|^2$, and decay amplitudes for this mechanism are heavily suppressed because $m_\nu/E_\nu \sim \mathcal{O}(0.1 \text{ eV}/100 \text{ MeV}) \sim 10^{-9}$. This heavy suppression of the decay amplitude is why $0\nu\beta\beta$ decay is not yet excluded (or alternatively better observed, except for one claim [54]). The total decay amplitude includes the sum over all massive neutrinos. If they are all light relative to the virtual neutrino momentum, the denominator for each mass is approximately equal, and the mass in the numerator can be factored from the integral. The integral over the angular variables results in a potential due to the virtual neutrino,

$$V_\nu(|\vec{x}-\vec{y}|) \propto \frac{\langle m_\nu\rangle}{|\vec{x}-\vec{y}|}\int_0^\infty d|\vec{p}_\nu| \frac{|\vec{p}_\nu|\sin(|\vec{p}_\nu||\vec{x}-\vec{y}|)}{\sqrt{|\vec{p}_\nu|^2 + m_\nu^2}}. \tag{1.55}$$

This potential must be included in the calculation of the nuclear matrix element, since $\vec{x}$ and $\vec{y}$ are vertex coordinates that involve the nucleons. The $0\nu\beta\beta$ nuclear matrix

element involves the same energy denominator as Equation 1.49. If one completely neglects the other terms ($M_{\mathrm{Mo}} - E_{\beta 1} - E_{\mathrm{Tc}} \ll \langle E_\nu \rangle$) and substitutes $M_{\mathrm{Mo}} - E_{\beta 1} - E_\nu - E_{\mathrm{Tc}} \rightarrow -\sqrt{|\vec{p_\nu}|^2 + m_\nu^2}$, a first approximation to the neutrino potential with this denominator from the matrix element included gives

$$V_\nu(|\vec{x} - \vec{y}|) \propto \frac{\langle m_\nu \rangle}{|\vec{x} - \vec{y}|} \int_0^\infty d|\vec{p}_\nu| \frac{|\vec{p_\nu}| \sin(|\vec{p}_\nu||\vec{x} - \vec{y}|)}{|\vec{p}_\nu|^2 + m_\nu^2} \propto \langle m_\nu \rangle \frac{e^{-m_\nu |\vec{x} - \vec{y}|}}{|\vec{x} - \vec{y}|}, \tag{1.56}$$

which is the famous Yukawa potential for the exchange of mesons, but now in terms of a neutrino! Heavy neutrinos are also possible and not yet excluded, but will not be discussed here.

Because of the non-Standard Model physics it requires, $0\nu\beta\beta$ decay holds great interest as a probe of fundamental symmetries for guidance toward new physics, but its complicated structure introduces interpretive difficulties. Firstly, it is suppressed by the chirality of the weak interaction. Based on the argument given above, the simplest approximation to the decay rate can be written

$$\Gamma(0\nu\beta\beta) = \frac{2\pi}{\hbar} \frac{dN}{dE_f} |\mathcal{M}(0\nu\beta\beta)|^2 \langle m_\nu \rangle^2, \tag{1.57}$$

in which $\langle m_\nu \rangle^2$ is based on the light neutrino approximation. The proportionality to $\langle m_\nu \rangle$ reflects the fact that only a Majorana mass term for the neutrino will contribute to the decay if the interacting current is purely left-handed. Based on the sum over neutrino masses performed to write the potential in Eequation 1.55, $\langle m_\nu \rangle$ is the effective neutrino mass, given by

$$\langle m_\nu \rangle = \sum_i \lambda_i^{c*} U_{ei} U_{ei} (m_\nu)_i. \tag{1.58}$$

The U_{ei} once again mix neutrino masses, but this form for the effective neutrino mass stresses possible CP violation. All λ_i^{c*} can be expressed as ± 1 up to an unimportant overall phase if CP is conserved. In this case, each pair of mass eigenstates would interfere perfectly constructively or destructively. The virtual neutrino forms a loop (see the right-hand diagram in Figure 1.4) and a calculation of the $0\nu\beta\beta$ decay rate requires a sum over its possible spins and an integral over its undetermined momentum. Because of the loop, unlike the $2\nu\beta\beta$ case where the 1^+ states in the intermediate nucleus

dominate, every combination of spin-parity in the intermediate nucleus contributes to the matrix element.

Equation 1.57 demonstrates the necessity of accurate knowledge about the nuclear matrix elements to extract information about the effective neutrino mass and CP phases. The calculation of $\mathcal{M}(0\nu\beta\beta)$ is a formidable task. For large numbers of nucleons and nuclei farther from closed shells, nuclear shell model calulations are unwieldy. The alternative that is widely present in the literature is the proton-neutron quasiparticle random phase approximation (pnQRPA, hereafter referred to as QRPA).

The QRPA includes two interaction parameters that characterize the proton-neutron coupling strengths, the particle-hole coupling strength g_{ph} and the particle-particle coupling strength g_{pp}. g_{ph} is widely used to fix the observed location of the Gamow-Teller giant resonance (GTGR), where most of the transition strength resides. Then g_{pp} is left a free parameter which can be tuned to reproduce experimental observables. The problem is that within this framework, the QRPA is not able to reproduce the β^-, EC, and $2\nu\beta\beta$ decay strengths simultaneously, which raises questions about its reliability for calculations of the more complex $\mathcal{M}(0\nu\beta\beta)$, which involves states of all J^π in the intermediate nucleus instead of only $J^\pi = 1^+$. There are also arguments that none of the J^π terms except for $J^\pi = 1^+$ show much dependence on g_{pp} and that other J^π terms dominate $\mathcal{M}(0\nu\beta\beta)$. Nevertheless, it is important to test these models as much as possible to ensure reliable limits on, or extractions of, new physics parameters from $0\nu\beta\beta$ decay experiments.

In terms of the $A = 100$ system, a recent experiment [5] placed a limit for ^{100}Mo of $T(0\nu\beta\beta) > 4.6 \times 10^{23}$ yr, from which a limit was placed on the effective neutrino mass of $\langle m_\nu \rangle < 0.7 - 2.8$ eV. The broad range in the corresponding effective neutrino mass is due to uncertainties in the nuclear matrix element. The heavy interest in the search for $0\nu\beta\beta$ decay requires equivalent efforts from the nuclear structure side for maximum insight into the results of double-beta decay experiments.

1.8 Solar Neutrino Detector

The Sun frees the energy that sustains life on our planet by converting protons into strongly-bound helium nuclei. This energy is transferred to the Earth by electromagnetic radiation. The pp chain (see Figure 1.5) is responsible for most of the energy released in our Sun, and its net effect is

$$4p + 2e^- \rightarrow {}^4\text{He} + 2\nu_e + 26.7\ \text{MeV}. \tag{1.59}$$

Although the energy transferred to the Earth is mostly electromagnetic, neutrinos provide the best test of our understanding of the Sun. This is because the Sun emits light as a blackbody; on average, a photon near the center of the Sun takes tens of thousands of years to make the random walk to the surface. Neutrinos, on the other hand, exit the sun (effectively) at the speed of light, with a total flux of approximately 10^{11} cm^{-2} s^{-1} neutrinos reaching the Earth.

The neutrinos that comprise $> 99\%$ of the neutrino flux from the sun come with energies $E_\nu < 5$ MeV. These neutrinos have been observed with radiochemical techniques, but real-time spectroscopic observations are just beginning. The Borexino detector [17] at Gran Sasso is now taking data on the ^{7}Be neutrino flux from the ppII chain. The detection of the lower energy ($E_\nu^{\text{max}} = 860$ keV) neutrinos will provide a test of the (MSW) matter effects that have been used to explain the missing ^{8}B neutrino flux. There could be surprises waiting at the lower energies of the pp chain neutrino spectrum.

The small Q value for ^{100}Mo neutrino capture, $Q_{\text{EC}} = 168$ keV, is ideal for detecting low-energy neutrinos, with the potential to detect even the $E_\nu^{\text{max}} = 420$ keV neutrinos from the $p + p \rightarrow {}^2\text{H} + e^+ + \nu_e$ reaction. This detection would take place via the coincidence between the electron released upon neutrino capture,

$$\nu_e + {}^{100}\text{Mo} \rightarrow {}^{100}\text{Tc} + e^-, \tag{1.60}$$

and the subsequent beta-decay electron from ^{100}Tc:

$${}^{100}\text{Tc} \rightarrow e^- + \bar{\nu}_e + {}^{100}\text{Ru}. \tag{1.61}$$

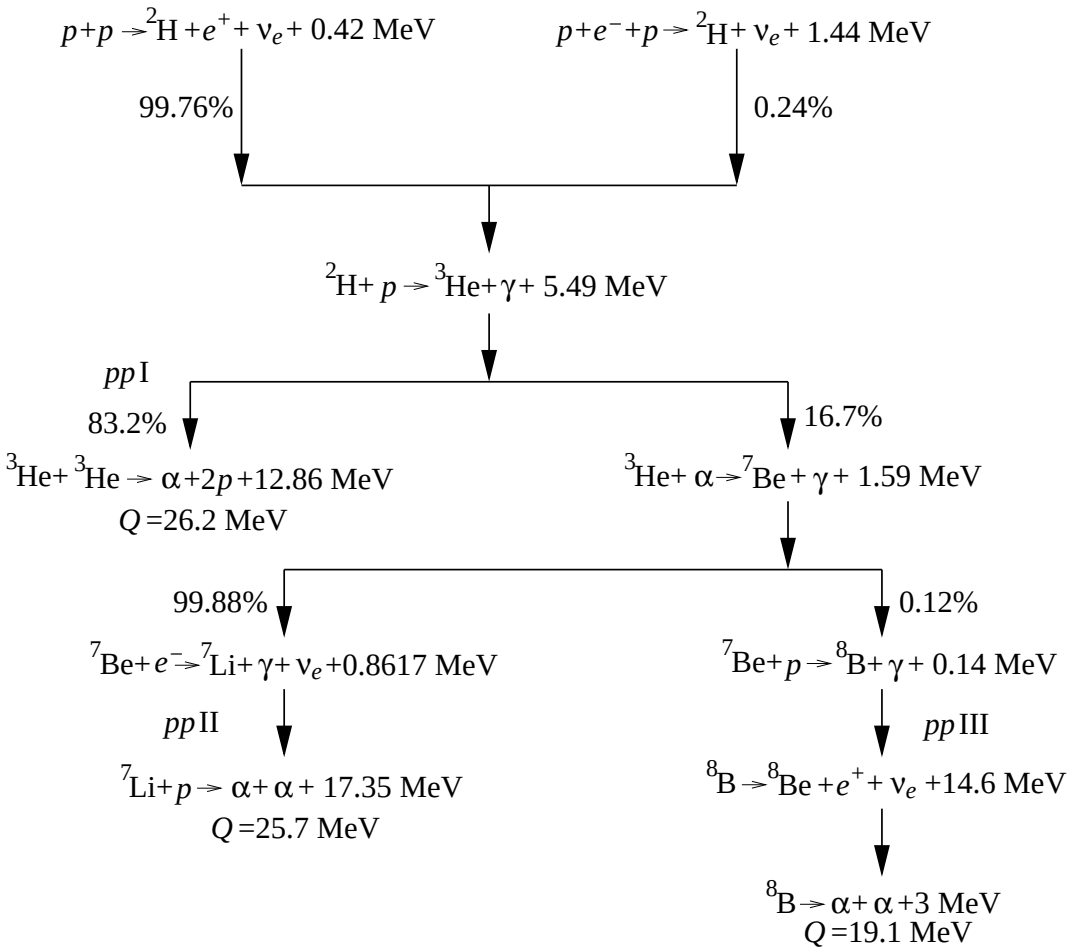

Figure 1.5: Schematic of pp chain reactions based on Reference [7]

Currently, we know of no plans to build such a detector. One obstacle is the large $2\nu\beta\beta$ decay background (see Table 1.1). It is not possible to avoid the background associated with $2\nu\beta\beta$ decay by means of shielding. Nevertheless, our measurement of $B(\mathrm{EC})$ provides useful information should someone devise a viable method to separate double-beta decay events from neutrino-capture events in a Mo detector.

Chapter 2

DESIGN AND APPARATUS

A measurement of the EC branch of ^{100}Tc presents several difficulties. Its short half-life, $t_{1/2} \approx 15$ s, makes it necessary to create it via a nuclear reaction, extract it from the various reaction products, and measure its decay quickly. The same nuclear physics mechanisms used to create ^{100}Tc also result in contaminants that complicate the measurement. The predominant mode of beta decay to ^{100}Ru (see Figure 2.1), occurring $> 99.99\%$ of the time, results in low-energy backgrounds associated with beta particles and electrons from Compton scattering of γ rays. These backgrounds make it more difficult to observe the x rays emitted by ^{100}Mo after EC decays.

2.1 Contaminants

Our production mechanism for ^{100}Tc is the reaction $^{100}\mathrm{Mo}(p,n)^{100}\mathrm{Tc}$. Competing reactions, for example $^{100}\mathrm{Mo}(p,2n)^{99}\mathrm{Tc}$, create unwanted contaminants.

The only direct measurement of the EC branch of ^{100}Tc published to date [36] used a He-jet system to move the reaction products to a tape, monitored γ rays from several contaminating radioactive Tc isotopes, then subtracted their calculated contribution to the Mo x rays, which are the signature for the EC of ^{100}Tc, but can also be generated by the decays of numerous contaminants. The precision of such a procedure is limited by the precision of the branch measurements in the decay schemes of the contaminants.

Figure 2.2 shows a γ-ray spectrum from a previous experiment that attempted to avoid contamination with the mass-resolving power of a dipole magnet, plus periodic movement of a tape-drive target to keep long-lived contaminants to a minimum. The $E_\gamma \approx 140$-keV γ ray from the $t_{1/2} \approx 6$ h isomer of ^{99}Tc is visible.

Figure 2.3 shows an x-ray spectrum from the same experiment. The spectrum has been vetoed with a planar scintillator placed between the target and the Ge detector,

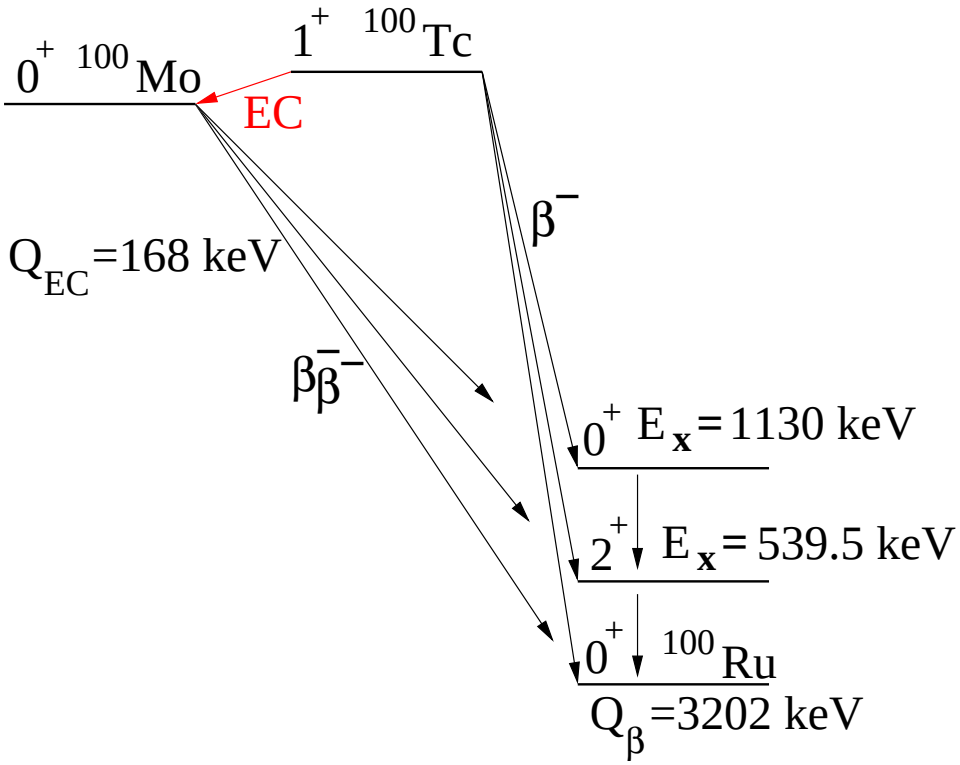

Figure 2.1: ^{100}Tc decay scheme: there is a large low-energy background due to energy deposition by beta particles from decays to ^{100}Ru, bremsstrahlung from the beta particles, Ru x rays created by internal ionization and excitation from beta decays and internal conversion of γ rays, and Compton scattering of the γ rays.

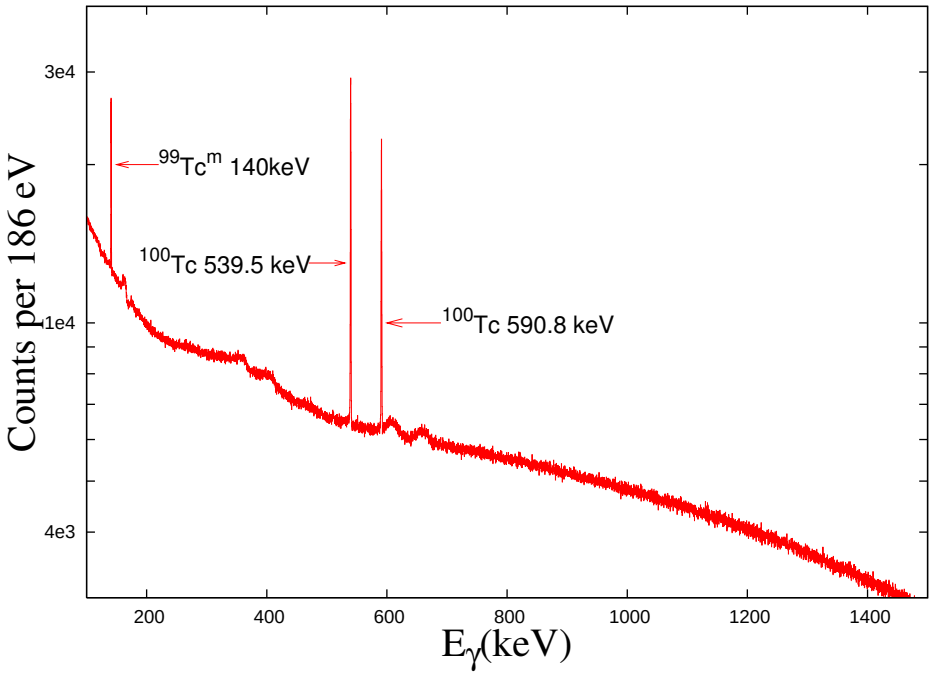

Figure 2.2: ^{100}Tc γ-ray spectrum with ^{99}Tc contamination. The funny bumps above all three γ rays in the spectrum are from summing that came with overflow from the ADC channel receiving the more amplified x-ray signals. Their problematic presence was removed in later experiments by adding a Zener diode in parallel to the signal.

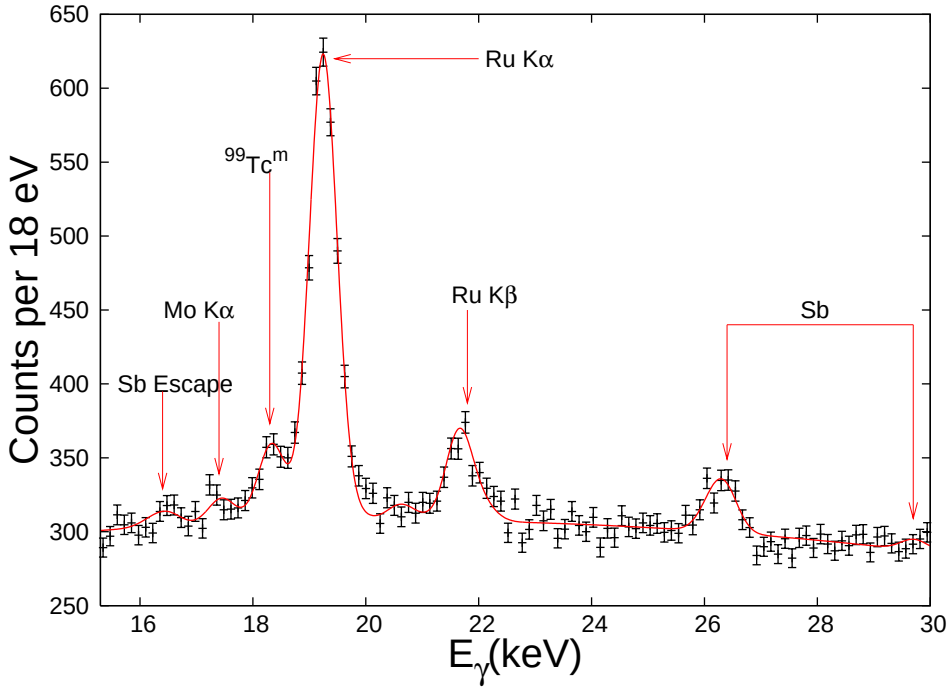

Figure 2.3: ^{100}Tc x-ray spectrum with ^{99}Tc contamination: the dominant Ru and Tc x rays are present despite beta-decay veto with a planar scintillator to reduce Ru decays and periodic movemement of the tape upon which the activity was deposited to reduce the presence of $t_{1/2} \approx 6$ h ^{99}Tc^m.

but such a geometry can veto 50% of the beta-decay events at most. The Ru and Tc x rays make it more difficult to resolve the Mo x rays by which we want to measure the EC branch.

To avoid all possible contaminants, we opted to use the resolving power of a Penning trap. The experiment was performed using the IGISOL [6, 50] facility at the University of Jyväskylä in Finland. A proton beam delivered from the K130 Cyclotron with kinetic energy $E_p = 10$ MeV and intensity of $I \approx 24$ μA impinged on a $\rho \approx 500$ μg/cm^2-thick, 97.4%-enriched ^{100}Mo target which was placed in an ion guide with helium at $p \approx 100$ mbar. The ^{100}Tc ions recoiled into the helium where they thermalized and the fraction that remained ionized were subsequently extracted from the gas cell. All ions were electrostatically guided through an RF sextupole ion beam guide while the

neutral gas was differentially pumped away. Finally, the ions were accelerated toward the mass separator at an electrostatic potential of $\phi \approx 30$ kV.

The $A = 100$ component of this beam was roughly separated by a magnet with a mass resolving power of $M/\Delta M \approx 250$, after which it was cooled and bunched in a linear segmented RFQ trap [63]. The bunched beam was introduced into a Penning trap in a 7-T magnetic field with a helium buffer gas, in which isobaric purity was achieved by means of a mass-selective buffer gas cooling technique. These separation and purification techniques are explained with greater detail in Chapter 3.

2.2 4π Scintillator

To minimize backgrounds, the goal was to make a scintillator that would veto all beta-decay events. Another goal was to maximize the number of events detected by the Ge detector. It was possible to achieve these two goals simultaneously by introducing the $^{100}Tc^{+}$ ions directly into a scintillator with a cylindrical bore. The hollow cylinder was given a length (≈ 4.8 cm) much longer than its diameter (≈ 0.95 cm) to maximize the scintillator's geometrical efficiency. A thin wall at the closed end of the cylinder allowed the activity to be placed very close to the Ge detector, maximizing photon-detection efficiency.

Figure 2.4 shows the setup. The purified $A = 100$ beam was extracted from the trap and implanted inside a scintillator designed to achieve $> 99\%$ coverage while allowing the target to be as close as ≈ 0.32 cm to a Ge detector. A hollowed cylinder within the scintillator held vacuum as part of the same volume as the Penning trap. Ions from the trap stopped in a ≈ 25 μm-thick aluminum foil that was inserted into the scintillator. A 6 mm-diameter collimator mounted on the foil holder prevented deposition of ions onto the sidewalls of the cylinder inside the scintillator.

The thickness of the thin plastic scintillator wall at the end of the cylinder was more than enough to withstand stresses due to vacuum on the inside of the cylinder and atmospheric pressure on the outside, but was very small compared to the ≈ 2.5-cm diameter of the Ge crystal. In this geometry, the front of the Ge crystal can cover

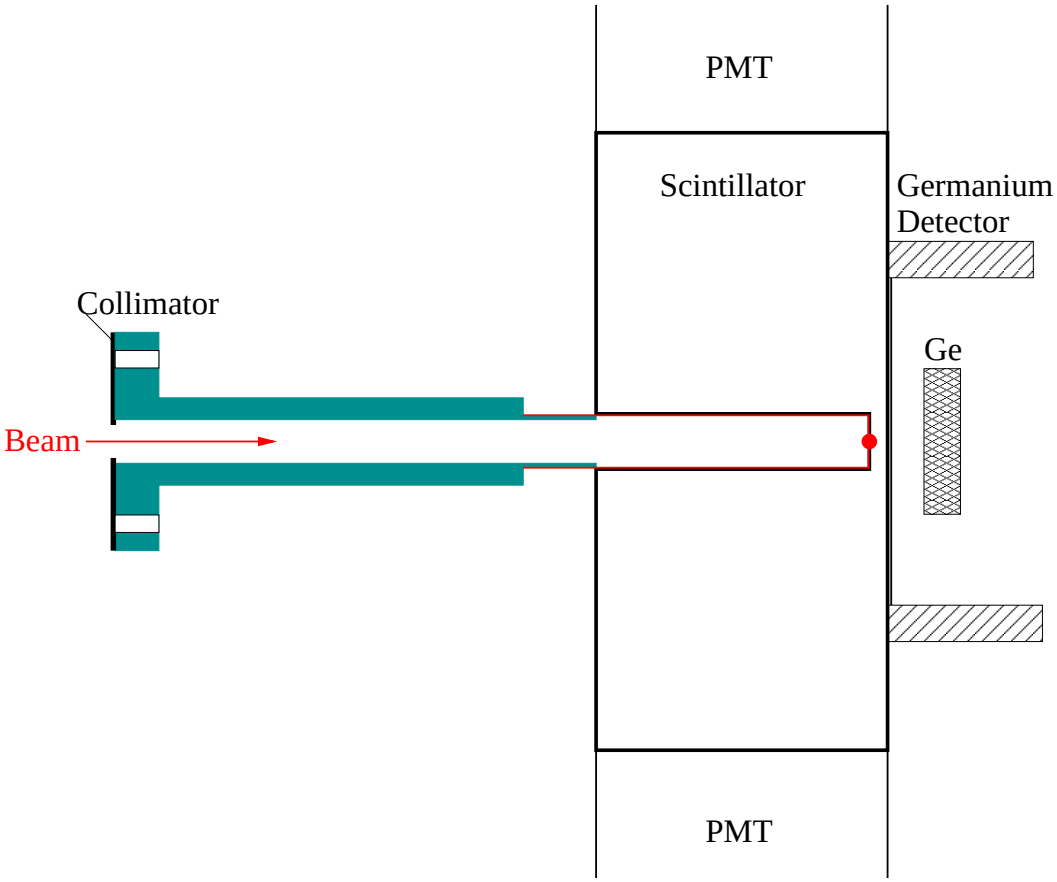

Figure 2.4: Experimental setup: ^{100}Tc ions were deposited onto an aluminum foil inside the scintillator. The beam was tuned by triggering on the scintillator. The scintillator allowed veto of $> 90\%$ of beta-decay events. The foil target in which the ions stopped was only separated from the Ge detector by the ≈ 0.32 cm-thick face of the scintillator to maximize photon-detection efficiency.

$\approx 17.7\%$ of 4π steradians. Design drawings of the scintillator and its support apparatus are included in Appendix E.

The scintillator was machined from a 2-in. thick sheet of organic plastic scintillator. We chose BC-408 (polyvinyltoluene-based plastic) scintillator from Saint-Gobain based on cost and performance. The two casted surfaces of the scintillator came with a very fine polish. Our machinists at CENPA took great care not to damage the delicate plastic of the scintillator while machining it. Precautions employed for handling the scintillator included the use of gloves to avoid contamination by harmful oils from the skin, the use of deionized water with soap in place of machining oil, and very slow machining to prevent creating too much heat and causing crazing in the plastic.

To maximize the scintillator's efficiency, we hand-polished the five surfaces that had been machined to optimize internal reflection of light created within the scintillator. The scintillator was polished by hand in eight steps, using progressively finer grits of Micro-Mesh cushioned abrasive polishing cloths. A smooth, clean granite slab provided a flat surface for polishing. Diluted detergent in deionized water provided lubrication. The cloths and polishing slab were rinsed several times during each step in the process, to remove the slurry created by the polishing process. The scintillator was also rinsed with deionized water and examined under a lens to monitor progress along with each rinse. The final polish produced a reflective surface of only slightly lower quality than the sole unmachined surface of the scintillator, which retained its polish from casting. Figure 2.5 shows the scintillator after polishing.

2.3 Phototube Mounts

A preliminary version of the experiment used optical glue to couple the PMTs to the scintillator. We glued the PMTs to the scintillator in Seattle before performing tests on the electronics and scintillator. The bonds failed during shipment to Finland, the PMTs had to be reglued at Jyväskylä, and we found that one PMT was not functioning during the preliminary run in November 2006.

To prevent the recurrence of this catastrophe, we designed a support system for the

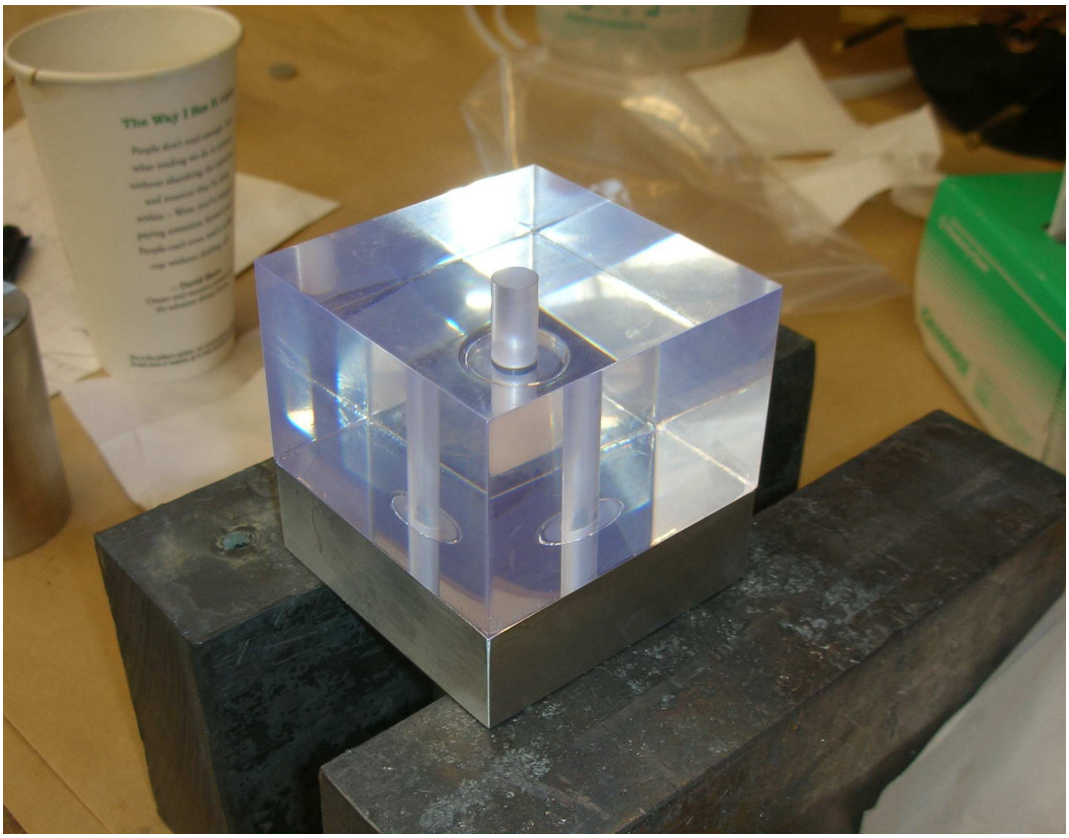

Figure 2.5: The scintillator, freshly polished and glued to its aluminum backing. Note the two reflections of the central cylindrical bore.

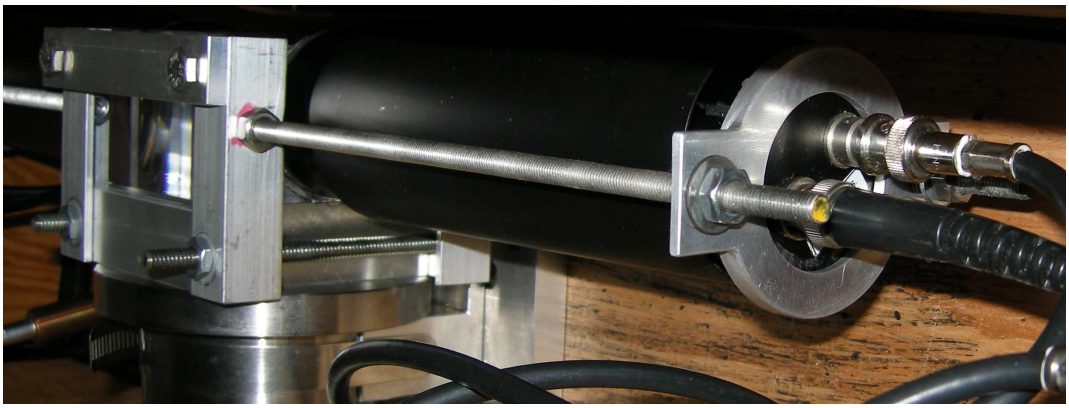

Figure 2.6: PMT mounting setup: the annular backing (far right) holds the PMT in place and fits over the BNC and SHV connections, while still allowing the base to have rotational freedom.

PMTs and achieved optical coupling with optical grease instead of glue, so that PMTs could be easily removed and replaced, if necessary. This detachable system also made the experiment more modular for shipment.

Figure 2.6 shows the PMT mounting system. The PMT mounting system was based on a frame mounted to the scintillator's aluminum backing with two threaded rods. Two more threaded rods held each PMT in place with backings designed for the PMT bases. Each PMT backing consisted of an annulus with an outer lip on one side and two tabs with holes for the threaded rods. The annuli were necessary to give the PMTs rotational freedom with the backing in place, while maintaining accessibility to the BNC signal outputs and SHV connections for the bases. Better optical coupling could be achieved by rotating the PMTs under pressure to remove bubbles from between the PMT and scintillator. Springs were placed between washers between the PMT backings and the nuts that tighened them, to keep the support from being too rigid for the possibly fragile glass PMTs. The support system is visible as part of the experimental setup in Figure 2.7.

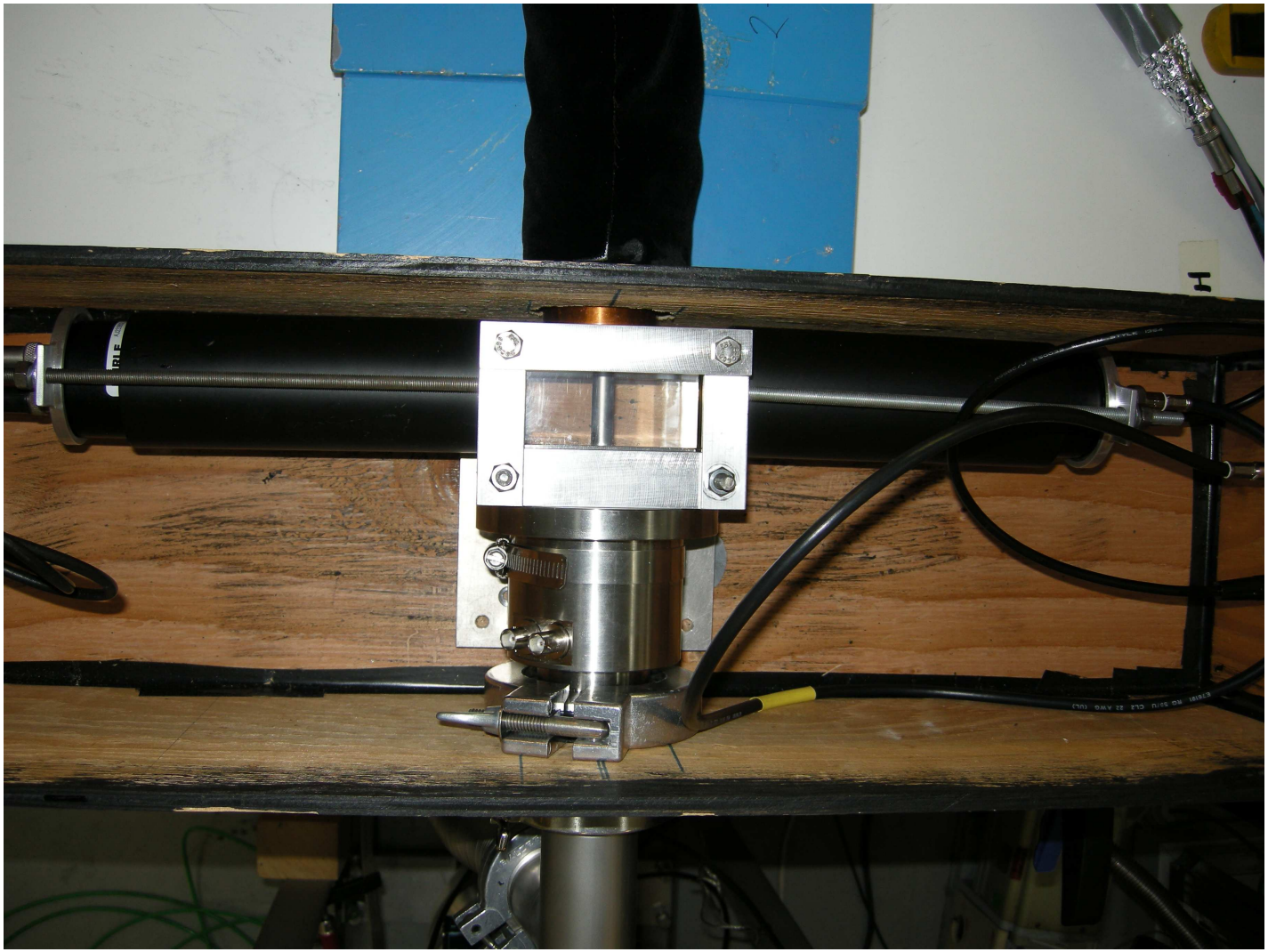

Figure 2.7: This picture shows the fully assembled experimental apparatus. The foil is visible in the scintillator. The scintillator is attached to the vacuum system from the Penning trap. The Ge detector abuts the front of the scintillator. The assembly is contained in a box built to prevent background light from reaching the phototubes.

2.4 Foil System

A special foil-holding system prevented possible contamination of the scintillator and allowed a diagnostic check on beam deposition into the scintillator. A copper guide, machined to snugly slide into the scintillator's aluminum backing, guided aluminum foils into the scintillator. Aluminum foils were cut using a template. An aluminum dowel turned on a lathe provided support to roll the foils into cylinders, then glue them together with a circular end piece in place. This process required finesse. It was important for the dowel to be significantly longer than the foil, not to give the foil too much tension before gluing, and to place the foil on the copper guide squarely so that it would enter the scintillator without getting caught on the constriction in the aluminum backing. Figure 2.8 shows a foil being prepared with a radioactive solution of ^{134}Cs on it. Figure 2.9 shows the same foil on the copper guide.

Options to wrap the scintillator with reflective alumized mylar or coat it with some type of paint to make it light proof were considered initially, but the delicate foils required monitoring upon insertion to be sure that they reached the end of the bore in the scintillator. Instead, we built a wooden box to sheild the scintillator from light. It was painted black and the lid was covered with black velvet to provide more shielding from light.

There were concerns that light would not reach the phototubes efficiently from the thin wall at the end of the cylindrical bore in the scintillator. To test this, a collimated ^{134}Cs source was placed between the scintillator and the Ge detector. Coincidence spectra were taken, requiring a γ ray in the Ge detector. No difference was observed between coincidence spectra taken with the source directly in front of the thin portion of the scintillator and coincidence spectra taken with the source placed to either side of the thin portion of the scintillator.

In Chapter 4, we will show that the scintillator was $> 95\%$ efficient for detection of beta decays from ^{100}Tc, so the polish and light-tight box were adequate. Figure 2.10 shows the output from one of the PMTs for two beta-decay spectra obtained during the experiment.

Figure 2.8: ^{134}Cs calibration source foil preparation. First, the aluminum foil was cut to a template made for the scintillator. Then a small amount of solution with ^{134}Cs was carefully placed on the foil in a fume hood (seen here), where the solution evaporated, leaving ^{134}Cs on the foil. Tape was placed over the radioactivity left from the solution, then checked to determine that the source was safely sealed. Then the foil was rolled on a specially-turned dowel and placed on a copper guide, as shown in Figure 2.9.

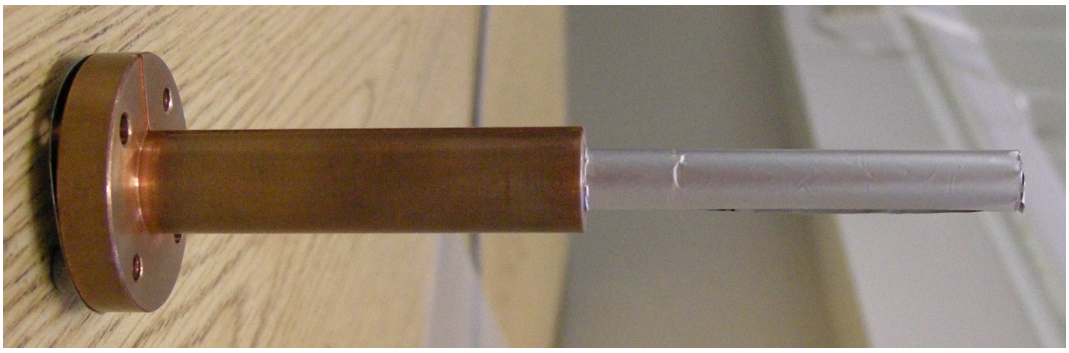

Figure 2.9: An aluminum foil rolled and placed on the copper guide. The foil fits into the hollow cylinder in the scintillator. The diameter of the copper fits snugly into the scintillator's aluminum mount to guide the foil into place.

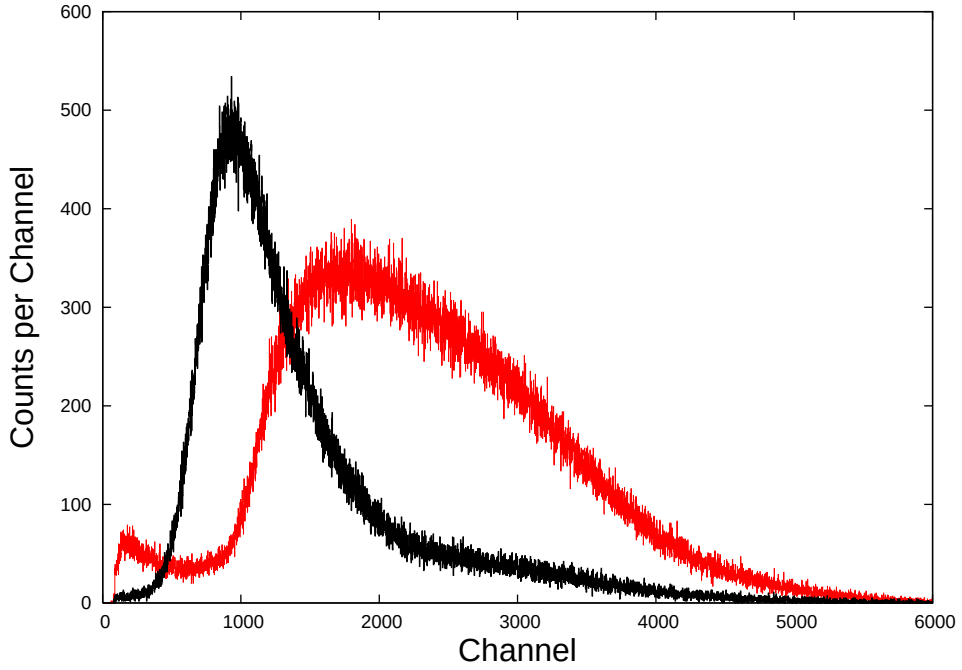

Figure 2.10: Spectra from one PMT for ^{100}Tc and ^{92}Tc. The ^{100}Tc spectrum, in black, is dominated by beta decays with endpoint $E_0 = 3.2$ MeV and intensity $I_\beta = 93\%$. The ^{92}Tc spectrum, in red, is dominated by 4.1 MeV positrons with $I_\beta = 88\%$. In addition to the larger endpoint energy, the positrons are shifted to higher energies by the Coulomb interaction, while the ^{100}Tc beta particles are shifted to lower energies by the Coulomb interaction.

Prior to the preliminary run, there were concerns that the ≈ 7.6 mm diameter of the copper guide for its ≈ 8.4 cm length would not allow the beam to pass into the scintillator. Depositing the beam into the scintillator from the trap posed no problem. The scintillator itself proved to be an ideal tuning mechanism, because of its highly efficient detection of beta-decay events. The beam optics between the trap and scintillator could be tuned to maximize the decay rate observed by the scintillator.

The foils could be removed should accidental contamination of the beam occur. The foils also allowed us to check that the activity was only being deposited at the end of the cylindrical bore. Activity spread along the sides of the cylindrical bore would make calibrations more difficult and less dependable.

The distribution of the deposited activity was tested by implantion ^{99}Tc. After implantation, the foil was removed, cut into pieces, then the end and sides of the foil were monitored for the $E_\gamma \approx 140$-keV γ rays from the $t_{1/2} = 6.02$ h isomeric state. With a 6 mm-diameter collimator in place, activity was only found on the end of the foil.

2.5 Data Acquisition

A sketch of the counting setup is shown in Figure 2.4. A p-type, 1 cm-thick, 25 mm-diameter Ge (LEPS) detector abutted the scintillator. The LEPS detector had an energy resolution of FWHM≈ 420 eV at $E_\gamma \approx 17$ keV and a solid angle of 17.7% of 4π with the Ge detector abutting the scintillator. The scintillator detector, which produced signals from beta particles emitted in the decay to ^{100}Ru, enabled efficient veto of backgrounds from low-energy beta particles and Ru x rays in the x-ray detector. Signals from the scintillator were read with two PMTs optically coupled to opposite faces of the scintillator perpendicular to the beam axis.

We produced two amplifications of the Ge detector signal: one with high gain, to observe the x rays with sufficient resolution, and one with low gain to measure γ rays. With every event, we recorded these two signals, the amplitudes of the signals from two phototubes on the scintillator, and TAC signals between x rays and either phototube. Any signal with amplitude larger than 2.4 keV in the x-ray detector triggered

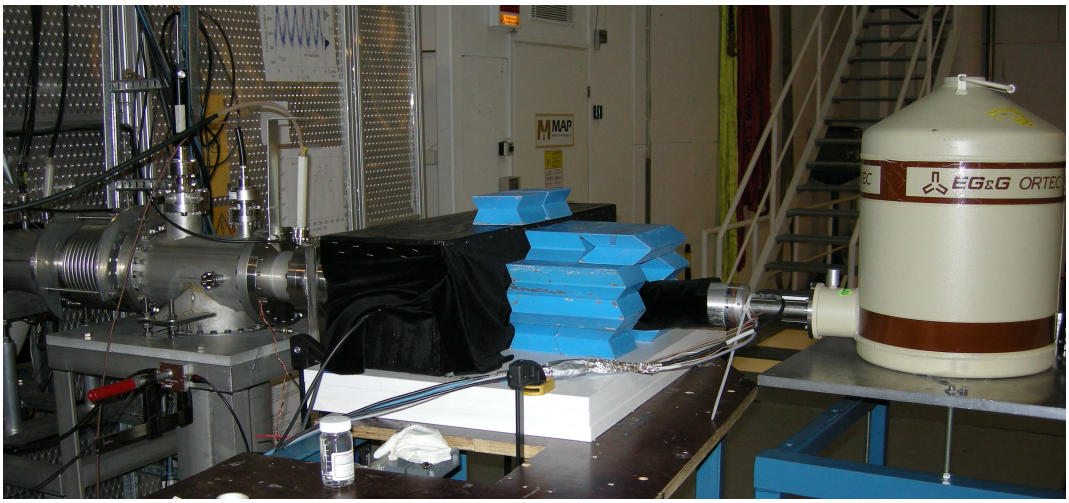

Figure 2.11: This is a picture of the full setup assembled and taking data in Finland. The beam comes from the Penning trap on the left. The scintillator and phototubes are in the light-tight box. The Ge detector enters the box and abuts the scintillator. Lead shielding is placed around the Ge detector to minimize backgrounds.

data acquisition. One signal from every 999 scintillator signals also triggered data acquisition, to allow an independent measurement of the number of decays. The apparatus was placed in a box to shield the phototubes from ambient light. Figure 2.11 shows the setup with the experiment in progress.

Figure 2.12 is a schematic diagram of the electronics system for data acquisition. Only one of two PMT signals have been drawn for simplicity. A logical OR was applied between both PMT signals going into the discriminator, which then provided a signal for both the 1 μs TTL and the 19 μs delay. The amplitudes of both PMT signals were also recorded. A 100 μs dead time was imposed upon the gate in hardware to ensure that no later events would interfere while the ADC and computer were busy processing an event. An OR was applied between the signal from the PMTs that was divided by 999 and the raw x-ray triggers, to generate the ultimate gate.

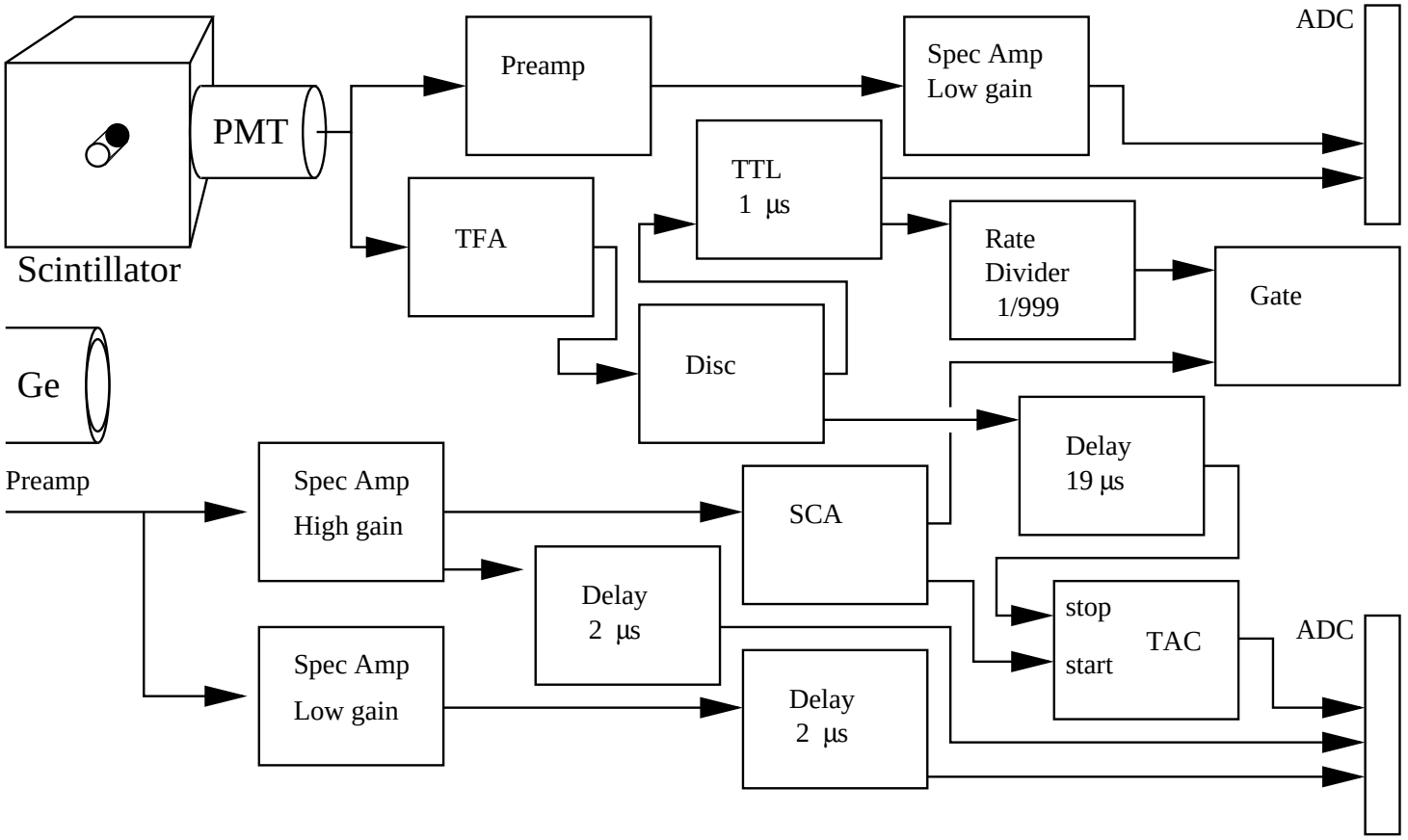

Figure 2.12: Electronics scheme for data acquisition

Chapter 3

ION TRAPPING TECHNIQUES

3.1 Ion Traps

Ion traps use special arrangements of electromagnetic fields to spatially constrain ions. In the absence of a buffer gas, the motion of an ion in such a trap depends solely upon its charge-to-mass ratio, $\frac{q}{m}$. Two ion-trapping techniques provided our experiment with an isobarically pure beam of mass $A = 100$: a radiofrequency quadrupole (RFQ) mass filter (one manifestation of a Paul trap) and a Penning trap. Paul traps use RFQ electric fields to create a potential with a time average that is effectively a binding harmonic well for ions with the selected $\frac{q}{m}$. Penning traps combine a large magnetic field to trap ions in the plane perpendicular to the field with a weak, static electric field to constrain them in the direction of the magnetic field.

Ion traps have numerous applications in science and industry. Residual-gas analyzers (RGAs) ionize gas molecules and use RFQ fields to detect trace amounts of residual gases in vacuum systems. For example, one can locate leaks in vacuum systems by introducting helium gas near possible leak sources while monitoring the amount of helium in the system with an RGA. These RGAs also monitor impurities during semiconductor fabrication. RFQ mass spectrometry techniques are also applied to chemistry, forensics, and quantum computing. The most important RFQ application for our experiment was to take a beam of ions, cool and bunch it in a helium buffer gas, and improve its optical properties for efficient transport in the Penning trap.

Penning traps facilitate high-precision measurements of frequencies. These frequencies are directly related to the trapped particle's mass and magnetic moment. Precise measurements of these quantities lead to cutting-edge tests of physics at the most fundamental level. More precise mass measurements reduce uncertainties in Q values for nuclear beta decay, leading to a reduction of the uncertainty in the value

of the V_{ud} element of the CKM matrix derived from $0^+ \rightarrow 0^+$ transitions [22]. Measurements of multiple eigenfrequencies in Penning traps probe the relative strength of the particle's orbital and spin magnetic moments, giving their g factors; this technique applied to both particle and antiparticle in the same trap tests CPT invariance [53]. A Penning trap experiment is in progress [65] which will reduce the uncertainty in the Q value for ^{3}H$\rightarrow^3$He beta decay, important for the planned direct ν_e mass measurement of the KATRIN experiment [64, 31].

Penning traps are also powerful tools for nuclear spectroscopy, with mass-resolving power that allows for separation of all contaminants, even isomeric states. This chapter only aims to describe the techniques used for isobaric beam purification at IGISOL for the ^{100}Tc EC branch experiment; for more thorough overviews of ion trapping techniques and their applications in nuclear physics, see the references [11, 10].

Another branch of ion-trapping techniques now establishes the most precise standards for chronometry. An atomic clock using laser-cooled ^{87}Sr ions in a lattice recently achieved a frequency standard with a fractional uncertainty corresponding to one second in more than two billion years [12].

3.2 IGISOL Facility

The cyclotron-based facility at the University of Jyväskylä in Jyväskylä, Finland provided us with an isobarically pure beam of mass $A = 100$, with approximately equal amounts of stable ^{100}Mo and the radiactive isotope of interest, ^{100}Tc. This was achieved using both the Ion Guide Isotope Separator On-Line (IGISOL) and the purifaction part of their Penning trap system, which is known as JYFLTRAP. A beam of protons with kinetic energy E_p= 10 MeV from the K130 cyclotron impinged upon a thin molybdenum foil enriched to 97% in ^{100}Mo. Recoil ions from the resulting nuclear reactions, including ^{100}Tc from ^{100}Mo$(p, n)^{100}$Tc, were extracted from a gas cell and electrostatically guided through an ion guide, then delivered to the RFQ mass filter, where they were cooled and bunched. After the RFQ mass filter, the beam was delivered to the purification Penning trap in pulses, from which the isobarically pure beam was ex-

tracted and delivered to our experimental setup. Figure 3.1 shows the layout of the IGISOL/JYFLTRAP facility. The following sections of this chapter describe each part of this process in more detail.

3.3 Ion Guide Isotope Separation

To use the power of ion-trapping techniques, first it is necessary to provide the desired ions. The IGISOL technique provides fast ($\lesssim$ 1 ms) extraction of primary recoil ions from a nuclear reaction. The first development of this technique took place at University of Jyväskylä in the early 1980s [3]. This technique is powerful both because it is chemically insensitive and because it obviates a dedicated ion source by utilizing the natural ionization mechanisms of the nuclear reaction. The resulting rapid extraction enables studies of radioactive isotopes with short half-lives, reaching all the way down to the millisecond level.

Figure 3.2 illustrates the IGISOL technique. An energetic beam of charged particles from the K130 cyclotron impinges upon a thin target and causes nuclear reactions. The reaction products recoil into helium gas, where they undergo collisions and reach thermal equilibrium; a fraction of the reaction products remain singly charged. The helium gas and ions flow through a nozzle toward vacuum due to differential pumping. An extraction electrode on the vacuum side of the separator attracts the ions and a beam of ions emerges with the energy of the extraction potential.

After extraction, the ions pass through an analyzing magnet with mass resolving power $\frac{M}{\Delta M} \approx 250$. This resolving power is enough for significant isobaric separation, but not to the level of purity desired for our ^{100}Tc EC branch measurement. The separated ions pass through an electrostatic lens and enter the two-dimensional Paul trap of the RFQ mass filter.

3.4 RFQ mass filter

The RFQ mass filter prepares the beam for efficient introduction into the Penning trap [63]. The ions undergo cooling in a buffer gas in a linear segmented RFQ trap

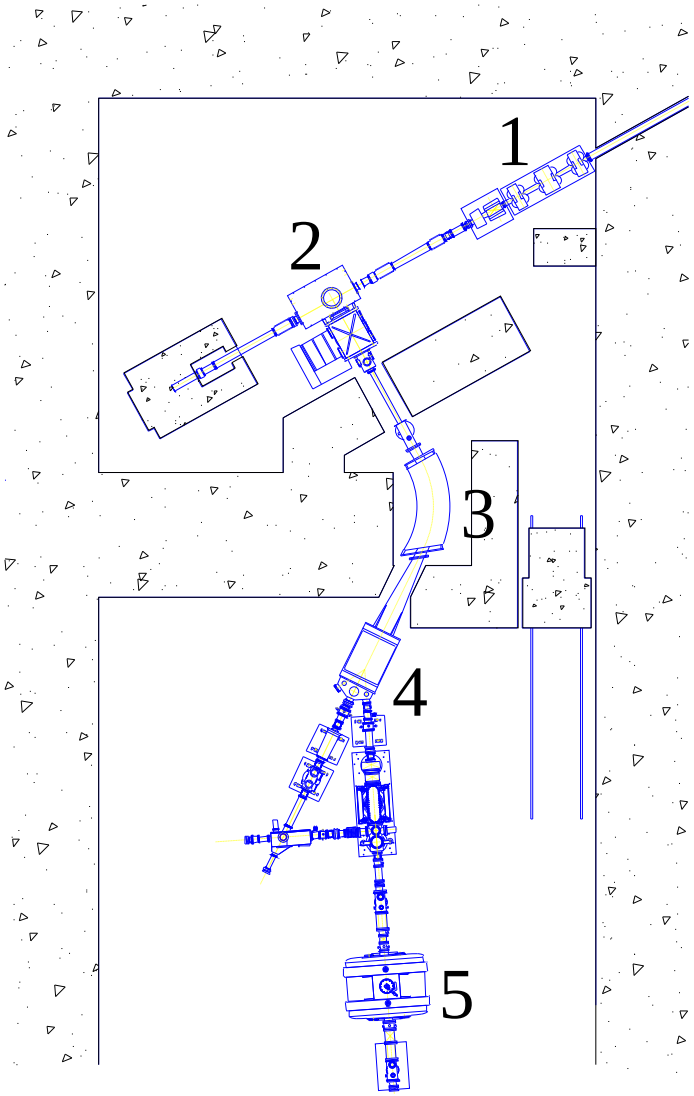

Figure 3.1: The IGISOL/JYFLTRAP layout. Beams from the K130 cyclotron enter via the upper right beamline (1), then impinge on a thin foil target (2). Recoil ions are accelerated perpendicular to the cyclotron beam (down and right in the figure) and bend through a dipole magnet (3). After the first dipole magnet, the beam is either delivered directly to nuclear spectroscopy experiments, or redirected via another dipole magnet (4) to the RFQ mass filter and Penning trap (5).

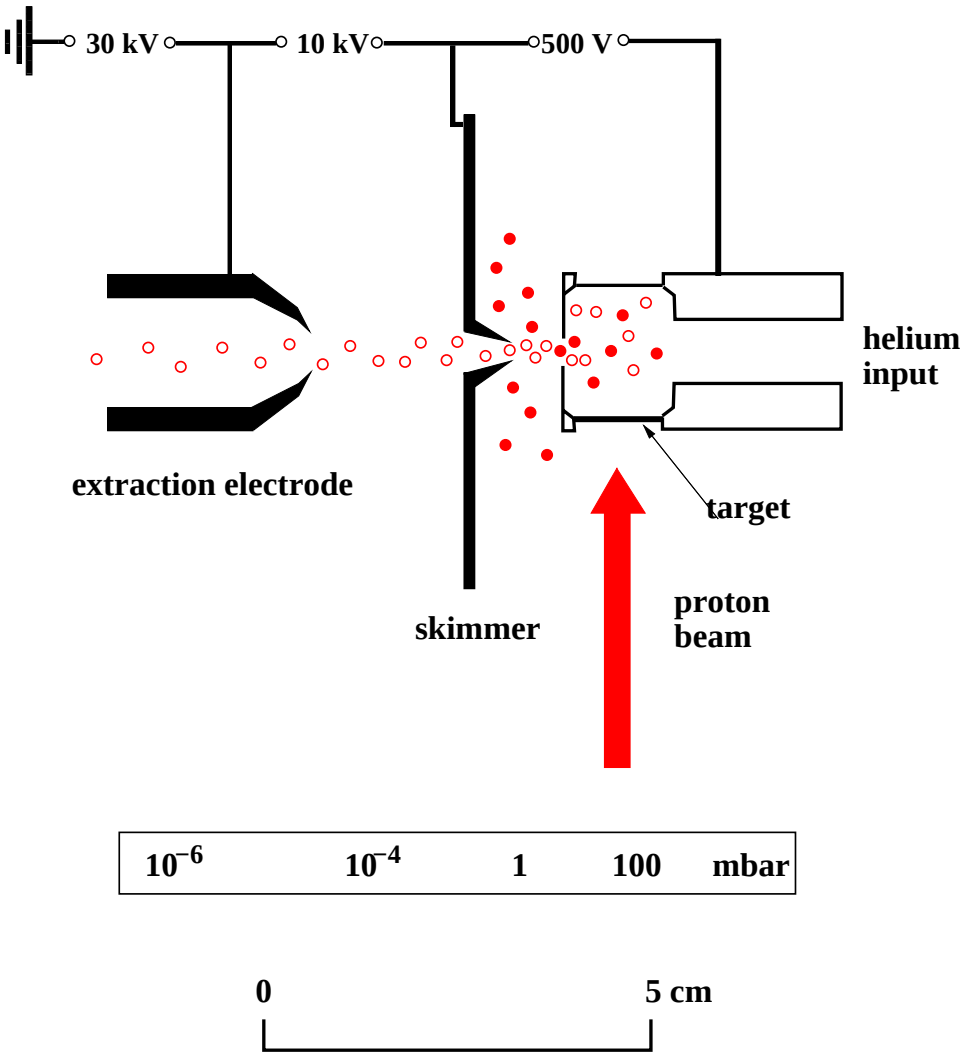

Figure 3.2: Schematic diagram of IGISOL source: solid circles represent helium gas; empty circles represent ions.

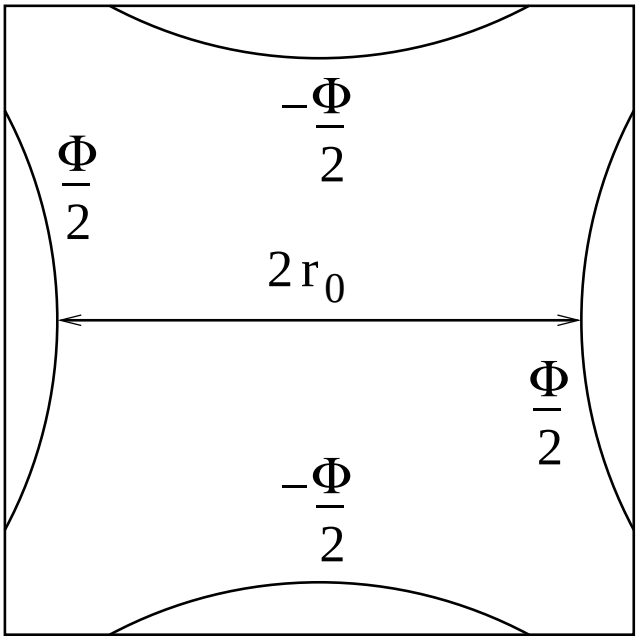

Figure 3.3: Beam's-eye view of RFQ mass filter: The four electrodes shown are cross sections of cylindrical rods.

with three segments to allow for bunching.

The RFQ mass filter has three segments, each a two-dimensional Paul trap with its own DC voltage. Two-dimensional Paul traps consist of four hyperbolic electrodes with cylindrical symmetry. (In practice, circular rods approximate hyperbolae well enough for many applications.) Each electrode is 180° out of phase with its nearest neighbors (Figure 3.3). The ions for which the RFQ filter is tuned see a restoring force; imagine an ion moving in a roughly circular path, being pushed toward the center by one electrode, only to arrive near the next electrode when the potential has oscillated so that it is pushed toward the center again. A time-dependent potential $\Phi_0(t)$ applied to the electrodes as shown in Figure 3.3 leads to an effective harmonic restoring potential for ions with the desired $\frac{q}{m}$:

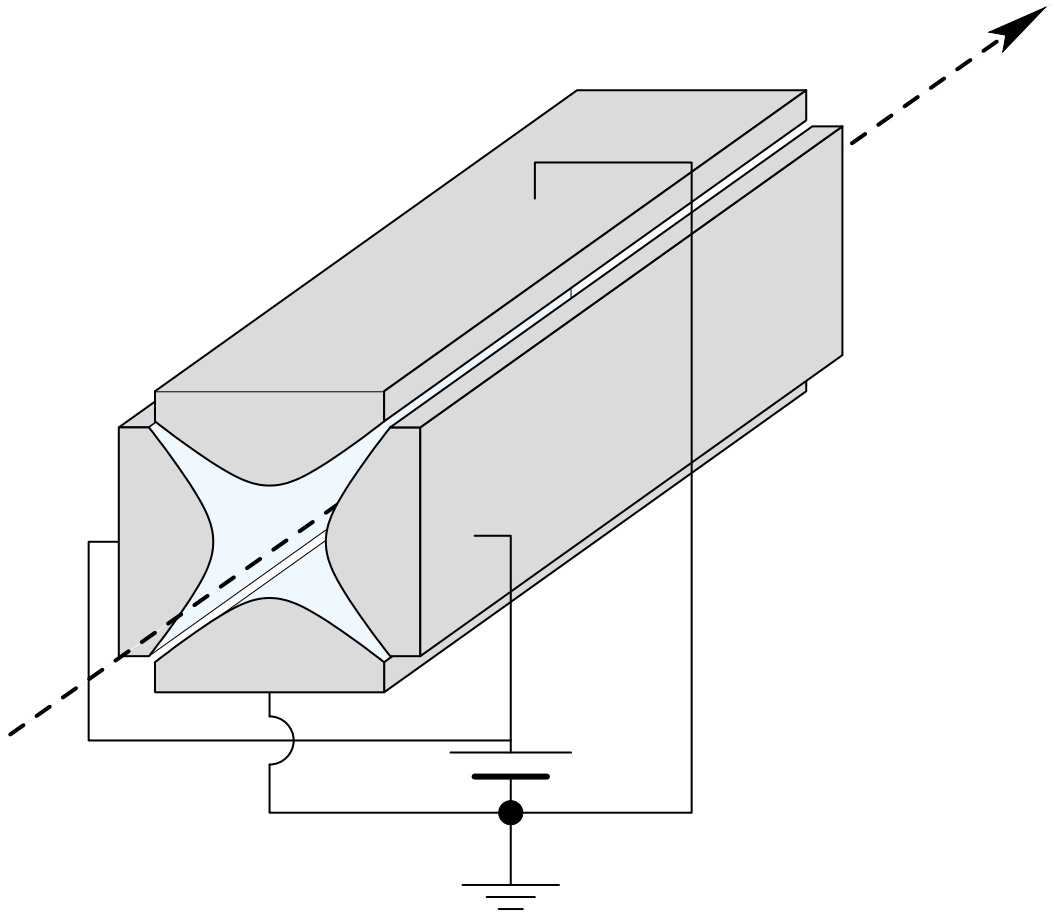

Figure 3.4: 3D view of an RFQ mass filter, taken from [23].

$$\Phi(\vec{r},t) = \frac{\Phi_0(t)}{2}\frac{(x^2-y^2)}{r_0^2}, \tag{3.1}$$

$$\Phi_0(t) = \frac{1}{2}(U_{dc}+V_{rf}cos(\omega_{rf}t)), \tag{3.2}$$

$$V_{eff} = \frac{q}{m}\left(\frac{V_{rf}}{r_0^2\omega_{rf}}\right)^2 r^2. \tag{3.3}$$

V_{rf}, U_{dc}, and ω_{rf} determine which ions stay centered and which ones are deflected to the side of the guide. Only ions with a small range of values of $\frac{q}{m}$ see the harmonic restoring potential V_{eff} (Equation 3.1). Figure 3.4 shows a three-dimensional view of an RFQ mass filter. The ion-focussing properties of a Paul trap are analogous to

those of an optical system with an alternating series of convex and concave lenses. The RFQ frequency and voltage play the same role as the spacing between lenses and their indices of refraction.

The RFQ mass filter segments at JYFLTRAP feature four cylindrical electrodes, with diameters of 2.3 cm and lengths of 40 cm. Amplitudes and frequencies of approximately 100 V and 500 kHz create an effective trapping potential with a depth on the order of 10 V. The ions lose energy in collisions with a helium buffer gas until they come to rest in the axial potential well of the mass filter created by the DC voltages applied to the segmented electrodes (see Figure 3.5). The mass filter reduces the energy spread from 80 to 1 eV in a total time of 1 ms. By creating a bunched beam with very low energy spread, the RFQ makes it possible to load the beam into the Penning trap with very high efficiency.

3.5 Penning trap

Penning traps are relatively simple systems which open many research avenues due to the myriad ion manipulation schemes they afford. The tandem Penning trap system at University of Jyväskylä measures masses and Q-values of rare isotopes with unsurpassed precision. The tandem Penning trap at Jyväskylä also offers rapid ($\sim$10 ms) mass resolution as powerful as $\frac{M}{\Delta M} \geq 10^4$ for spectroscopy experiments, using a mass-selective buffer gas cooling technique. Isobaric purification requires only a short period of time in a buffer gas plus quadrupole excitations; more complex time-dependent excitation schemes can achieve isomeric purification.

It is rewarding to understand the simple elegance of a Penning trap. First consider a classical description of the simplest implementation of a Penning trap. Ions are constrained to cyclotron motion in two dimensions by a large magnetic field. The result is circular motion at the cyclotron frequency, ω_c, with a radius proportional to the ion's radial kinetic energy, E_{kr}.

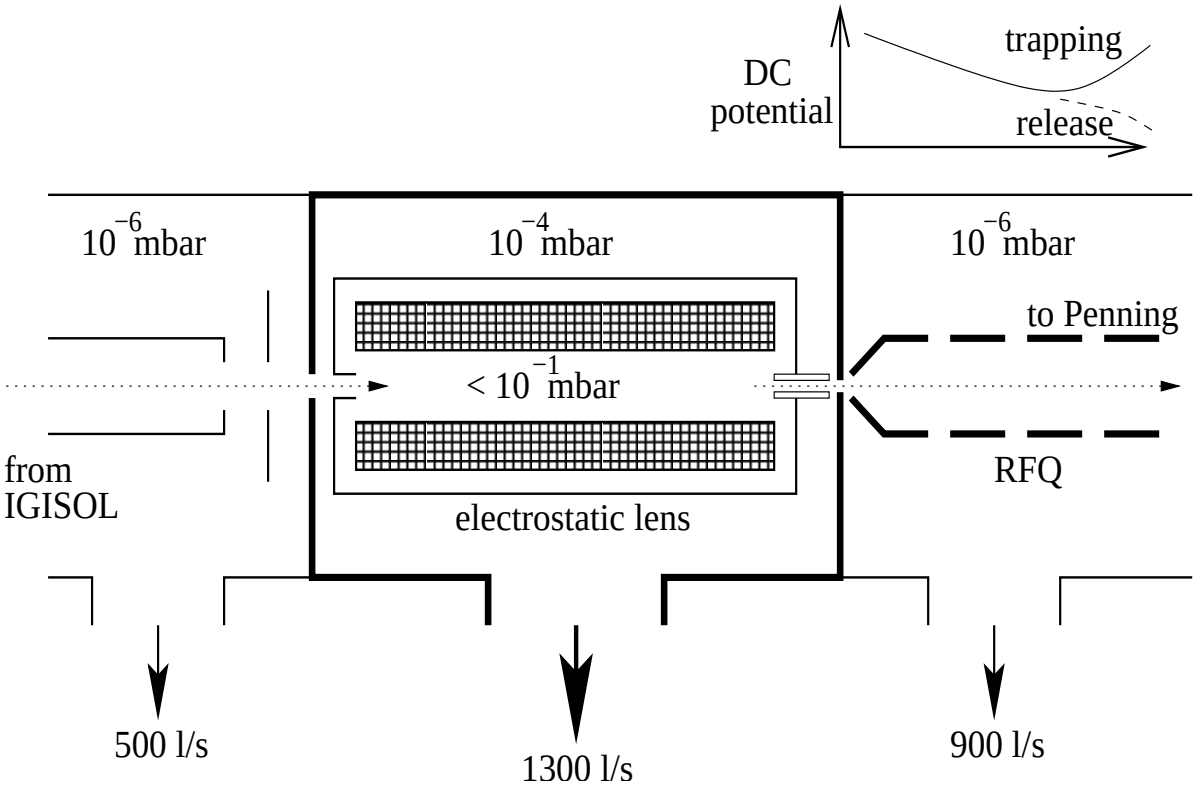

Figure 3.5: An electrostatic lens, held at $\phi \approx$39.9 kV so that the ions enter the RFQ with kinetic energy of approximately 100 eV, injects the ion beam from IGISOL into the RFQ cooler and buncher. A qualitative sketch shows the DC potential on the RFQ segments for both bunching and release.

$$\overrightarrow{B} = B\hat{z} \tag{3.4}$$

$$\omega_c = \frac{q}{m}B \tag{3.5}$$

$$r_c = \sqrt{\frac{2mE_{kr}}{\omega_c}} \tag{3.6}$$

An electrostatic potential traps the ions in the axial (z) direction. Because the potential must satisfy Laplace's equation, the electrostatic field also has an azimuthal component. The equipotentials that meet these criteria are hyperboloids of revolution, which give the desired potential well in the axial direction and retain symmetry in the azimuthal plane.

$$\Phi(z,r) = \frac{\Phi_0}{2d^2}(z^2 - r^2/2) \tag{3.7}$$

$$d = \frac{1}{2}\sqrt{2z_0^2 + r_0^2} \tag{3.8}$$

$$z_\pm(r) = \pm\sqrt{z_0^2 + r^2/2} \tag{3.9}$$

$$r(z) = \sqrt{2z^2 + r_0^2} \tag{3.10}$$

Electrodes of the form $z_\pm(r)$ and $r(z)$ satisfy boundary conditions to create the desired potential, $\Phi(z,r)$. The factor of $2d^2$ in the denominator ensures that the potential difference between the ring electrode, $r(z)$, and the endcaps, $z_\pm(r)$, is equal to the applied potential difference, Φ_0. Figure 3.6 shows a cross-section profile of the hyperboloids of revolution in the ideal Penning trap geometry. JYFLTRAP and other accelerator-based traps now use a more complex cylindrical geometry without endcaps (see Figure 3.7). This geometry is much more convenient for the introduction and extraction of ion beams. Many segments, specially designed with different lengths and potentials, give the ideal field in a small, central volume.

The Lorentz force equation applied to the resulting field gives coupled motion in

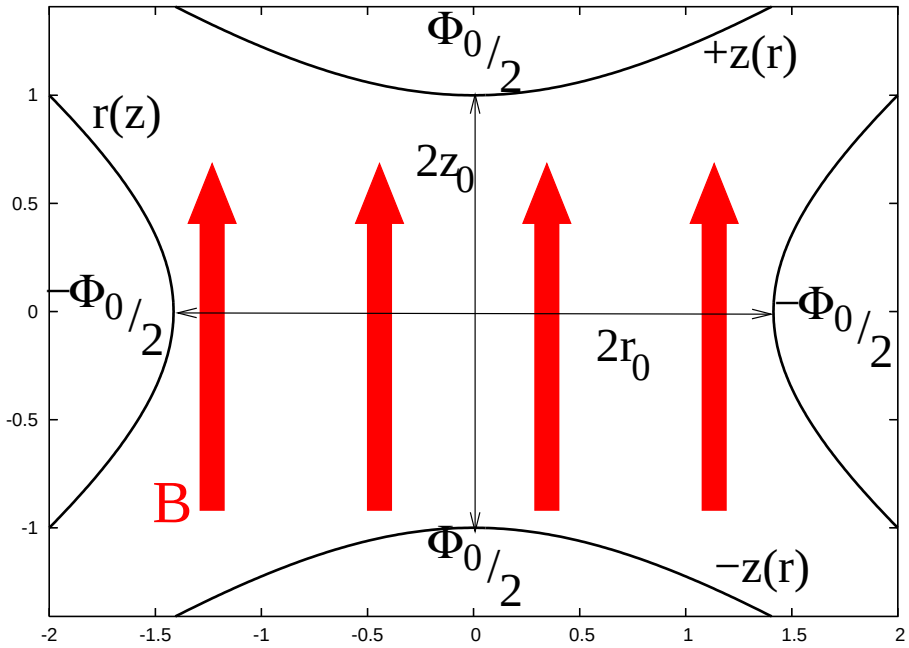

Figure 3.6: Electrode configuration for an ideal Penning trap with electrodes of the hyperbolic from described in Equation 3.7, where z_0=1 cm, r_0=$\sqrt{2}$ cm, and d=1 cm. Real Penning traps feature correction electrodes to account for the fact that the hyperbolic electrodes don't extend to infinity.

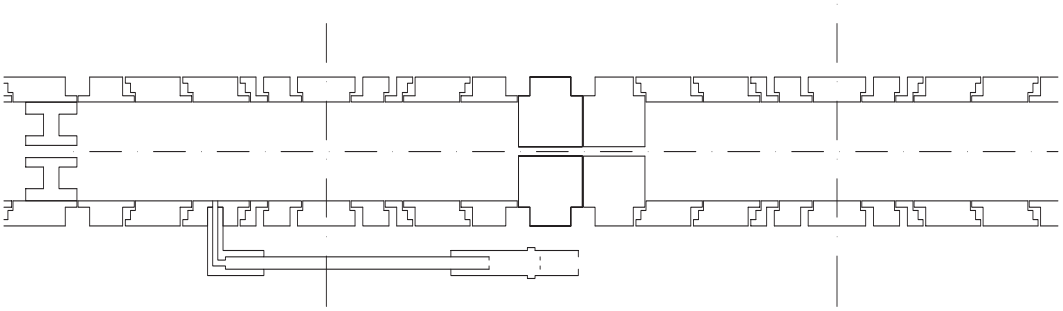

Figure 3.7: The configuration of the cylindrical tandem Penning trap used at JYFLTRAP, adapted from [23]. This configuration allows for easy introduction and extraction of ions. The magnetic field points along the dot-dashed line that is the central axis. Each trap is comprised of one central, eight-fold segmented electrode, a pair of endcap electrodes, and two pairs of smaller correction electrodes between the central electrodes and endcaps. The bunched ion beam from the RFQ cooler enters through the 4 mm diaphragm on the left. The purification trap is centered at the intersection of dot-dashed lines on the left; this region is filled with helium buffer gas at $p \sim 10^{-4}$ mbar. The 2 mm diaphragm between the purificaton trap and the precision trap serves both to keep the buffer gas from diffusing into the precision trap and to prevent contaminant ions at larger orbital radii from exiting the purification trap.

the azimuthal plane and decoupled motion in the axial direction.

$$\ddot{z} \quad = -\frac{q}{m}\left(\frac{\Phi_0}{d^2}z\right) = \quad -\omega_z^2 z \tag{3.11}$$

$$\ddot{x} \quad = \frac{q}{m}\left(\frac{\Phi_0}{2d^2}x + B\dot{y}\right) = \quad \left(\frac{\omega_z^2}{2}x + \omega_c\dot{y}\right) \tag{3.12}$$

$$\ddot{y} \quad = \frac{q}{m}\left(\frac{\Phi_0}{2d^2}y - B\dot{x}\right) = \quad \left(\frac{\omega_z^2}{2}y - \omega_c\dot{x}\right) \tag{3.13}$$

The use of a complex variable to describe the azimuthal motion gives two decoupled solutions. Substitute $\vec{r} = x + iy = re^{-i\omega t}$ into Equation 3.11 and two eigenfrequencies, $\omega_\pm$, emerge. The eigenmode with larger frequency (ω_+) and smaller amplitude is known as reduced cyclotron motion; the eigenmode with smaller frequency (ω_-) and larger amplitude is known as magnetron motion.

$$\ddot{\vec{r}} = \quad -\omega^2\vec{r} \tag{3.14}$$

$$= \quad \ddot{x} + i\ddot{y} \quad = \frac{\omega_z^2}{2}\vec{r} - i\omega_c\dot{\vec{r}} \tag{3.15}$$

$$\rightarrow \omega^2 - \omega\omega_c + \omega_z^2/2 = 0 \tag{3.16}$$

$$\omega_\pm = \frac{\omega_c \pm \omega_1}{2} \tag{3.17}$$

$$\omega_1 = \sqrt{\omega_c^2 - 2\omega_z^2} \tag{3.18}$$

The motion is stable if the magnetic field is large; Equation 3.14 requires $\omega_c^2 > 2\omega_z^2$ for the eigenfrequencies to be real. An ion's motion is characterized by three frequencies, $\omega_+ > \omega_z > \omega_-$, and three corresponding amplitudes, r_+, r_z, and r_-. Figure 3.8 shows the three modes of motion, along with the net motion. The new eigenfrequencies are related to the original eigenfrequencies,

$$\omega_c = \omega_+ + \omega_-,$$

$$\omega_z^2 = 2\omega_+\omega_-, \tag{3.19}$$

and

$$\omega_c^2 = \omega_+^2 + \omega_z^2 + \omega_-^2.$$

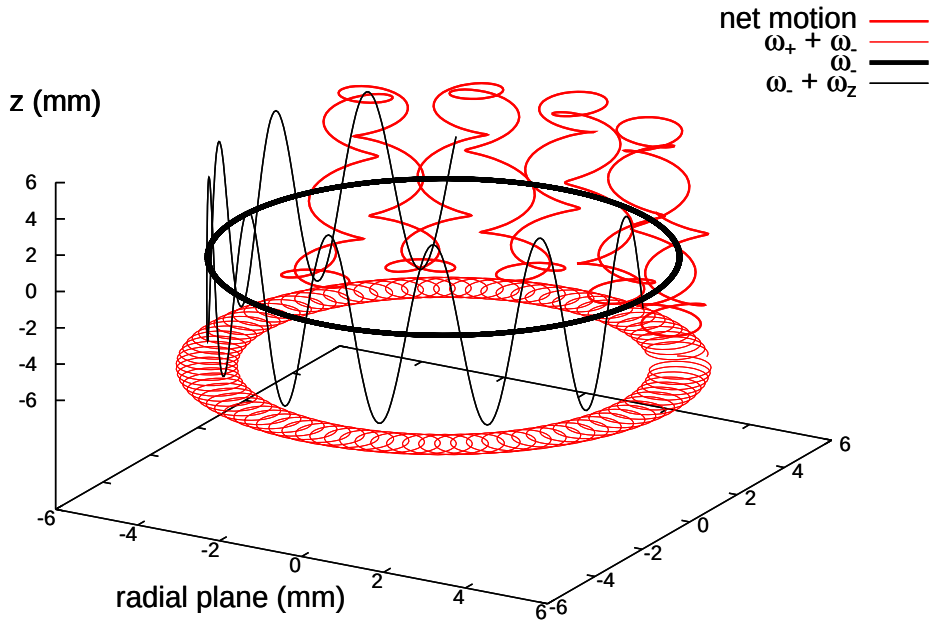

Figure 3.8: Schematic diagram of ion motion in a Penning trap. The size of the reduced cyclotron (ω_-) orbits are exaggerated with respect to the other orbits for clarity.

The last equality is the subject of an important invariance theorem [13, 14]; measuring all three eigenfrequencies allows precision measurements to overcome limitations due to misaligments between the electric and magnetic fields, along with small imperfections in the quadrupole field. In practice, the magnetic field is strong and results in a pronounced heirarchy, $\omega_+ \gg \omega_z \gg \omega_-$. In this case, the eigenfrequencies can be expressed more simply.

$$\omega_- \approxeq \frac{\omega_z^2}{2\omega_c} = \frac{\Phi_0}{2Bd^2} \tag{3.20}$$

$$\omega_+ \approxeq \omega_c - \frac{\Phi_0}{2Bd^2} \tag{3.21}$$

Note that in Equation 3.20 the magnetron frequency, ω_-, is effectively independent of the mass; this property is important for purification techniques. For JYFLTRAP, with $^{100}Tc^+$ ions in a 7 T magnetic field, the approximate values are $\omega_c/(2\pi)$ =1.1 MHz, $\omega_-/(2\pi)$ =1.7 kHz, and $\omega_z/(2\pi)$=61 kHz. These will be the default values used to estimate trap parameters for the remainder of this chapter.

Having solved the equations of motion for an ion in a Penning trap, it is enlightening to use these solutions to write the system's energy. The azimuthal energy takes a simple form if one considers an ion at an instant when the magnetron and reduced cyclotron motions are in phase. Figure 3.9 illustrates these two components of the ion's motion in this scenario. Solving for the corresponding energy in terms of the eigenfrequencies, one finds

$$E_r = \frac{1}{2}m(\vec{r}_+\omega_+ + \vec{r}_-\omega_-)^2 - \frac{q\Phi_0}{4d^2}(\vec{r}_+ + \vec{r}_-)^2 \tag{3.22}$$

$$\rightarrow \quad E_r = \frac{1}{2}mr_+^2\omega_+^2\left(\frac{\omega_+ - \omega_-}{\omega_+}\right) - \frac{1}{2}mr_-^2\omega_-^2\left(\frac{\omega_+ - \omega_-}{\omega_-}\right). \tag{3.23}$$

Thus the net motion is described by three independent simple harmonic oscillators. Two simple harmonic oscillators describe the radial motion. The magnetron motion term is negative, because of the $-r^2$ form of the electrostatic potential in the radial plane.

Having described the ion's motion from a Newtonian perspective for simplicity, it is useful to write its Hamiltonian to discuss perturbations in a quantum mechanical

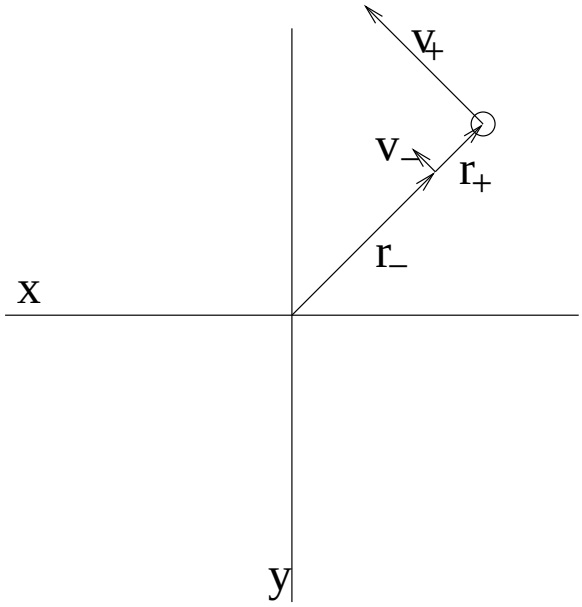

Figure 3.9: Vector diagram of an ion's motion in the azimuthal plane of a Penning trap when the magnetron motion and reduced cyclotron motion are in phase (not to scale). The magnetic field goes into the page.

framework. The homogeneous magnetic field $\vec{B} = B\hat{z}$ can also be represented by a vector potential

$$\vec{A} = \frac{B}{2}x\hat{y} - \frac{B}{2}y\hat{x}. \tag{3.24}$$

Using this potential to write the azimuthal Hamiltonian for a charged particle in a Penning trap in terms of the known eigenfrequencies (see Equation 3.14), one finds

$$H_{xy} = \frac{1}{2m}\left(p_x^2 + p_y^2\right) - \omega_1\left(xp_y - yp_x\right) + \frac{1}{8}m\omega_1^2\left(x^2 + y^2\right), \tag{3.25}$$

which can be rewritten as the Hamiltonian of two independent simple harmonic oscillators with a canonical transformation:

$$q_\pm = \frac{1}{\sqrt{2}}\left(\sqrt{\frac{m\omega_1}{2}}x \pm \sqrt{\frac{2}{m\omega_1}}p_y\right), \tag{3.26}$$

$$p_\pm = \frac{1}{\sqrt{2}}\left(\pm\sqrt{\frac{m\omega_1}{2}}y + \sqrt{\frac{2}{m\omega_1}}p_x\right) \tag{3.27}$$

Note that the canonical coordinates still satisfy the commutation relations $[q_i, p_j] =$

$i\hbar\delta_{ij}$. For symmetry, it is also nice to transform the z coordinates

$$q_z = \sqrt{m\omega_z}z, \qquad p_z \to \frac{p_z}{\sqrt{m\omega_z}},$$

so that we can write a Hamiltonian in terms of three independent simple harmonic oscillators that all have the same form:

$$H = \hbar\omega_+(a_+^\dagger a_+ + 1/2) + \hbar\omega_z(a_z^\dagger a_z + 1/2) - \hbar\omega_-(a_-^\dagger a_- + 1/2), \tag{3.28}$$

$$E(n_+, n_z, n_-) = \hbar\omega_+(n_+ + 1/2) + \hbar\omega_z(n_z + 1/2) - \hbar\omega_-(n_- + 1/2), \tag{3.29}$$

$$n_i = a_i^\dagger a_i, \tag{3.30}$$

$$a_i = \frac{1}{\sqrt{2}}(q_i + ip_i), \qquad i = +, z, - \tag{3.31}$$

$$a_i^\dagger = \frac{1}{\sqrt{2}}(q_i - ip_i). \tag{3.32}$$

The a_is and $a_i^\dagger$s are the familiar raising and lowering operators. The energies of the modes are given by their quantum numbers, n_+, n_z, and n_-. As an example, the ground-state energy of an ion with mass $A = 100$ in a Penning trap with a 7 T magnetic field is $\sim \mathcal{O}(10^{-9})$ eV, corresponding to a temperature of $\sim$10 μK. Quantum effects are generally not important for heavy ions, but they can be for electrons, especially with the lower energy levels of the axial and magnetron motions.

The magnetron motion is unstable and excitations of it decrease the total energy. Figure 3.10 shows an energy-level scheme. Any loss mechanism, or dipole excitations applied in the radial plane at the magnetron frequency, will result in orbits of larger radii. This is crucial for both beam purification and precision mass measurements.

The purification scheme for the ^{100}Tc EC branch measurement used a buffer gas and a quadrupole field in the azimuthal plane. After the bunched, cooled ion beam enters the Penning trap from the RFQ, all ions lose energy to the buffer gas and their magnetron orbits increase. In terms of the quantum numbers, n_+ and n_z decrease until they are in equilibrium with the buffer gas, but n_- will increase continually.

A quadrupole potential is applied to the segmented ring electrode of the Penning trap, as shown in Figure 3.11, at the cyclotron frequency. For small radii, the resulting

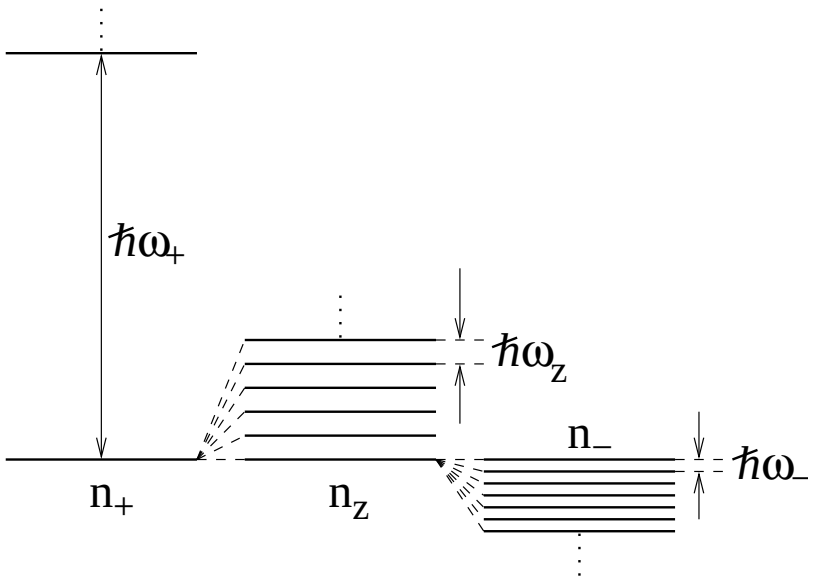

Figure 3.10: Energy level scheme for a proton in an ideal Penning trap; magnetron energy levels are exaggerated. Spin energy levels are of the same order of magnitude as the modified cyclotron levels, but nevertheless unimportant for the mechanisms discussed here.

potential in the azimuthal plane is well approximated by

$$V_q(t) = \frac{\Phi_q}{r_0^2}(x^2 - y^2)\cos(\omega_c t + \phi_q).$$

This can be written as a perturbation to the Hamiltonian in terms of the creation and annihilation operators of Equation 3.28. There are other terms, but the only ones that are important for our purposes have the form

$$H_1 = \frac{e\hbar\Phi_q}{2m\omega_1 r_0^2}\left(e^{-i(\omega_c t+\phi_q)}a_+^\dagger a_- + e^{i(\omega_c t+\phi_q)}a_-^\dagger a_+\right).$$

The cyclotron frequency, $\omega_c = \omega_+ + \omega_-$, connects the energy levels of the magnetron motion and reduced cyclotron motion. See the paper by Kretzschmar [57] for a thorough theoretical treatment of the rich phenomena associated with this perturbation.

Using Fermi's Golden Rule, the transition rates are proportional to the matrix elements of the raising and lowering operators squared, so for the two different terms

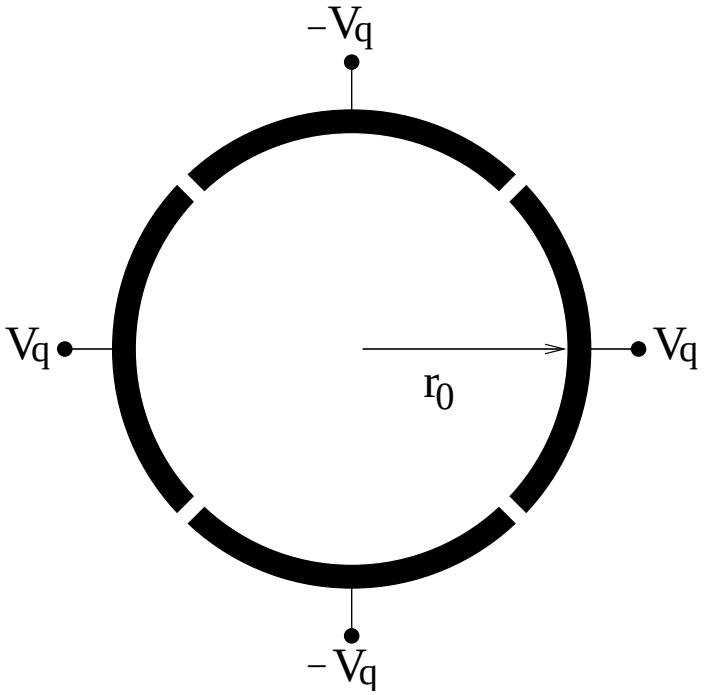

Figure 3.11: Ring electrode configuration for quadrupole excitation: the ring electrode is segmented into four pieces and the voltages V_q and $-V_q$ are applied between the x and y segments at a frequency of ω_c.

connecting the magnetron and cyclotron motion one finds the rates

$$\Gamma(|n_+, n_-\rangle \rightarrow |n_+ + 1, n_- - 1\rangle) = c(n_+ + 1)(n_-), \tag{3.33}$$

$$\text{and} \quad \Gamma(|n_+, n_-\rangle \rightarrow |n_+ - 1, n_- + 1\rangle) = c(n_+)(n_- + 1). \tag{3.34}$$

Because $n_- \gg n_+$ when the quadrupole excitation is initially applied, the ions gain energy in cyclotron motion, which they subsequently lose to the buffer gas.

This process reaches equilibrium when the ions are in a state with $n_+ \approx n_-$ and have the kinetic energy dictated by the temperature of the buffer gas. Thus the ions are driven up the potential hill in the azimuthal direction until they are centered in the trap at a radius defined predominantly by the reduced cyclotron motion. Figure 3.12 illustrates this process schematically. Assuming a temperature of 300 K, this corresponds to $n_+ = n_- \sim \mathcal{O}(10^7)$ and a radius of a few hundred microns for ^{100}Tc with the trap parameters discussed previously.

The applied quadrupole frequency selects ions by mass because the cyclotron frequency, $\omega_c = \omega_+ + \omega_-$, depends upon the ion's charge-to-mass ratio. The resolving power that can theoretically be achieved is equal to the product of the applied frequency and length of time during which the excitation is applied. The frequency of interest is 1 MHz and typical excitation times are on the order of 100 ms, which gives a resolution

$$\frac{M}{\Delta M} = \omega_c T_{rf} \approx 10^5, \tag{3.35}$$

so that for isotopes near mass $A = 100$, mass differences as small as several MeV can be separated. The length of time over which centering takes place depends upon the quadrupole voltage applied and the pressure of the buffer gas.

The selected ions are finally centered in the trap with very little energy. When the potential on the exit side of the trap is lowered, only the centered ions with the selected mass emerge through the 2 mm diaphragm that constricts the exit (see Figure 3.7). The beam has a very small emittance, having been spatially constrained within a few tenths of a millimeter and cooled to energies on the order of tens of meV.

Figure 3.13 shows a mass scan for $A = 100$ from the purification trap that gives a resolving power $M/\Delta M \approx 25,000$, more than enough to prevent contamination from

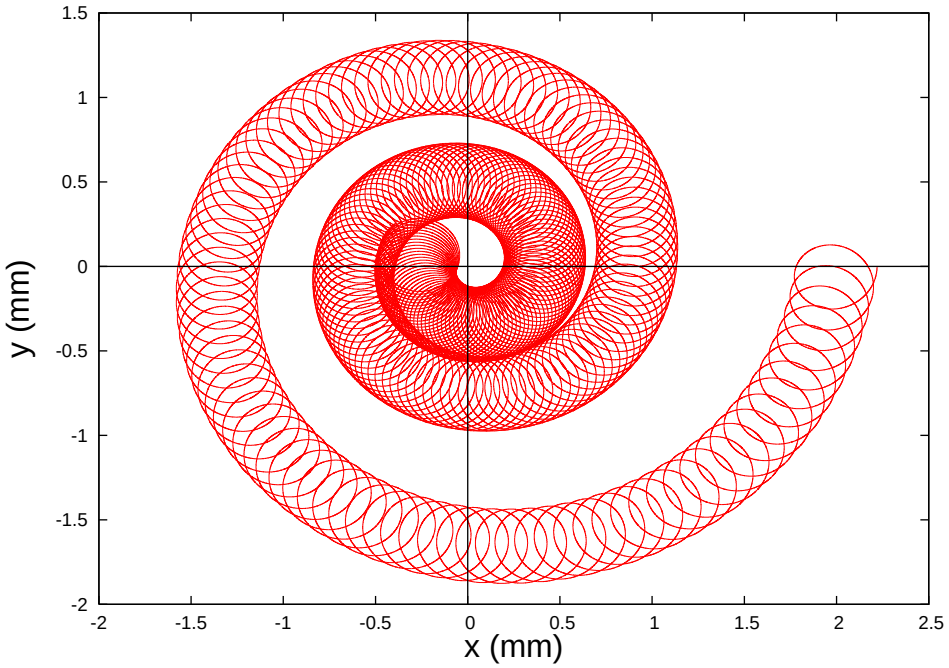

Figure 3.12: Schematic of ion motion with azimuthal quadrupole excitation in a buffer gas: in this schematic diagram, the ion begins in a magnetron orbit with radius 2 mm; the magnetron radius decreases as the perturbation pushes the ion into cyclotron motion, while the energy gained in cyclotron motion is constantly lost to the buffer gas. The minimum radius the ions reach is determined by their equilibrium with the buffer gas. The actual cooling by the buffer gas is based on collisions, so no actual ion trajectory would be as orderly as the one shown.

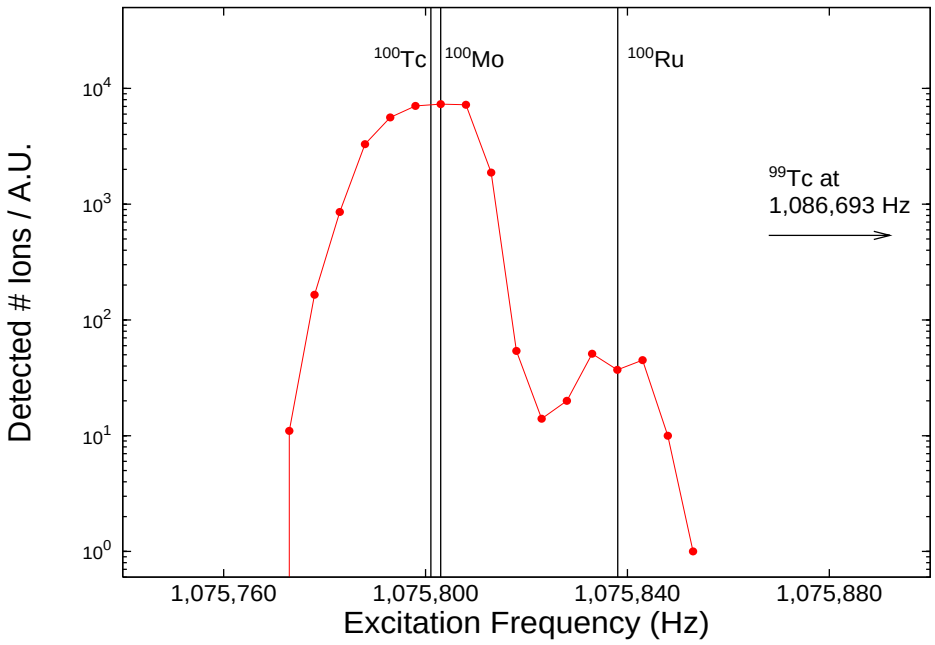

Figure 3.13: Mass scan for $A = 100$ obtained with JYFLTRAP.

^{99}Tc, which comes with unwanted Tc x rays from an isomeric state with a long haf-life, $t_{1/2} \approx 6$ h. The excitation frequency was set to $f = 1,075,800$ Hz for beam purification during the experiment.

Chapter 4

ANALYSIS

The ratio of the number of EC decays, $N_{\rm EC}$, to the total number of decays, N_{tot}, determines the EC branch. Mo K-shell x rays, created by vacancies in the K-shell electron energy levels of the Mo atom after electron capture, provide the signal for $N_{\rm EC}$. The 539.5- and 590.8-keV γ rays, together with measurements of their intensities, provide the signal for N_{tot}. A calibration of the Ge detector's efficiency as a function of photon energy determines $N_{\rm EC}/N_{tot}$ from the number of Mo x rays observed relative to the number of counts in either the 539.5- or 590.8-keV γ-ray photopeaks.

First we present our calibration of the Ge detector and use a precise measurement of the 590.8-keV γ-ray intensity to calculate the EC branch. Then we present a calibration of the scintillator and an independent measurement of the 539.5- and 590.8-keV γ-ray intensities. Finally, we discuss possible systematic errors.

4.1 Photon Efficiency

The relative efficiency between the Mo K-shell x rays and the 539.5-keV and 590.8-keV γ rays, needed to extract $N_{\rm EC}/N_{\rm tot}$, was obtained from calibration sources and simulations based on the experimental geometry. ^{92}Tc was obtained from impurities in the enriched ^{100}Mo target by tuning the dipole magnet, RFQ buncher, and Penning trap for $A = 92$. Figure 4.1 shows the spectrum of x rays with our fit for the $A = 92$ beam.

^{92}Tc provides an intense source of the same Mo x rays that signal the EC decay of ^{100}Tc. We produced fits for these x rays using a line-shape functional consisting of a low-energy exponential folded with a Gaussian, plus a low-energy shoulder for Compton scattering with a shape determined by PENELOPE [73] simulations. In our fits we fixed the relative x-ray intensities and extracted the relative efficiencies for

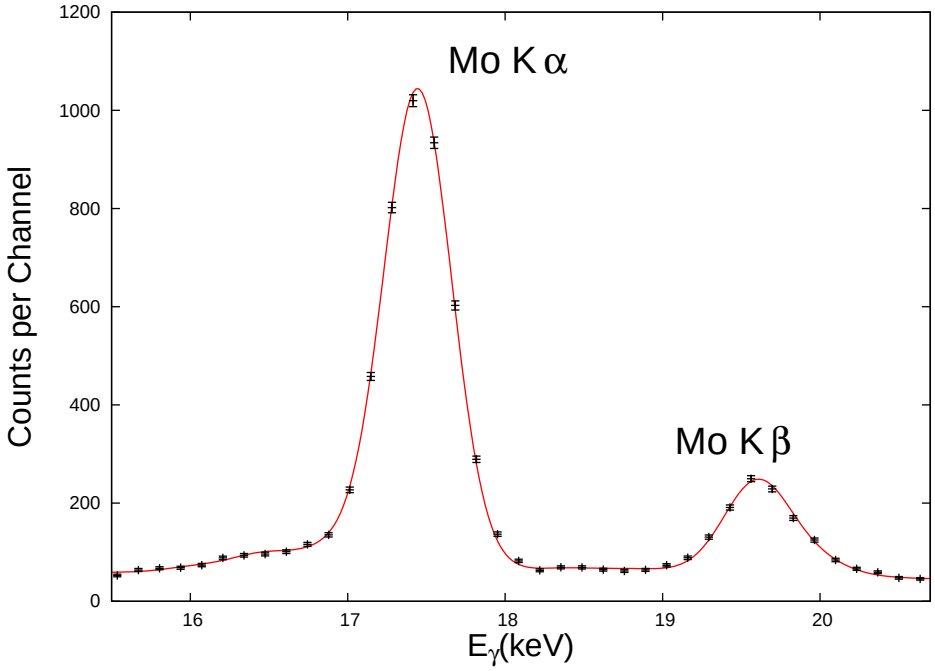

Figure 4.1: ^{92}Tc x-ray spectrum fit: the two apparent peaks are actually composed of five x rays, two Kα and three Kβ. The shape of the low-energy shoulder due to Compton scattering, seen below the $\overline{E}$ =17.44 keV Kα peak, was fixed using simulations with PENELOPE and included in the fit. The same Compton shoulder shape, relative efficiencies, and energy calibration were imposed on all fits to the x-ray spectra from the decay of ^{100}Tc. This fit gives $\chi^2/285 = 1.030$.

the two Mo-Kα and three Mo-Kβ x rays. The shape of the Compton shoulder and the energy calibration determined in Figure 4.1 were also used to constrain all fits to the x-ray spectra from ^{134}Cs and ^{100}Tc. The relative efficiency between the Mo Kα and Kβ x rays is dominated by the dead layer of the contact at the front of the Ge crystal and the thickness of the thin wall of the scintillator (see Figure 2.4).

Figure 4.2 shows a fit to a ^{134}Cs-source x-ray spectrum from a ^{134}Cs calibration source. Figure 4.3 shows a ^{134}Cs-source γ-ray spectrum from the same source. The calibration source was made by placing drops of a solution with ^{134}Cs onto a foil made for the scintillator, then allowing the solution to evaporate. Figure 2.8 shows a foil with the ^{134}Cs solution on it in preparation. This method facilitated reproduction of the experimental geometry for accurate calibration. We used the known ^{134}Cs x-ray and γ-ray intensities [79] to determine the relative efficiencies between x and γ rays. Summing corrections for the ^{134}Cs source were taken into consideration and found to be negligible.

Figure 4.4 shows efficiencies for x rays and γ rays from both ^{92}Tc and ^{134}Cs with results of Monte Carlo simulations performed using the code PENELOPE [73]. The 563.2- and 569.3-keV γ rays from ^{134}Cs are conveniently close in energy to the 539.5- and 590.8-keV γ rays from the decay of ^{100}Tc. The simulations were used to determine the relative efficiencies between the ^{100}Ru γ rays and the Mo K-shell x rays used in our EC branch calculation.

4.2 Electron-Capture Branch Calculation

Figure 4.5 shows a raw γ-ray spectrum taken with the ^{100}Tc beam. Figure 4.6 shows a raw x-ray spectrum taken with the ^{100}Tc beam. Figure 4.7 shows the fit for the Mo- and Ru-x-ray lines to a scintillator-vetoed spectrum from five runs. We calculate the electron-capture branch as:

$$B(\text{EC}) = \frac{A(\text{Mo-K})}{A(590.8\text{-keV})} \frac{\eta(590.8\text{-keV})}{\eta(\text{Mo-K})} \frac{(1-c)\cdot I_\gamma(590.8\text{-keV})}{f_K \omega_K}, \tag{4.1}$$

where A(Mo-K) and A(590.8-keV) are the photopeak areas for the Mo-K and 590.8-keV transitions; η(590.8-keV)/η(Mo-K) is the relative efficiency between the 590.8-keV

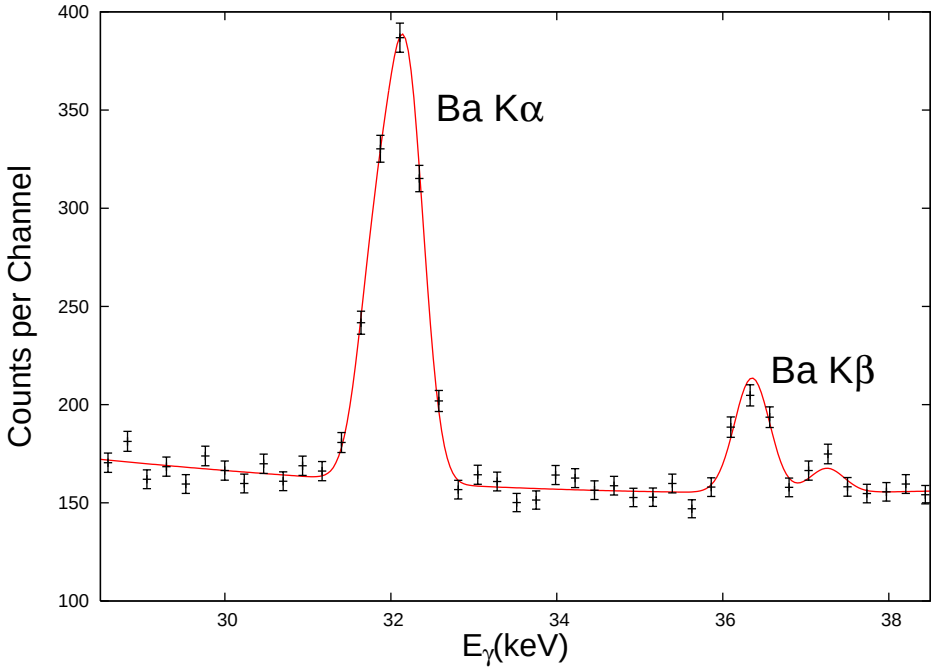

Figure 4.2: ^{134}Cs x-ray spectrum: the relative efficiencies between the Kα and Kβ x rays were fixed by the simulations used to calculate the relative efficiencies for the fit to the ^{92}Tc x rays in Figure 4.1.

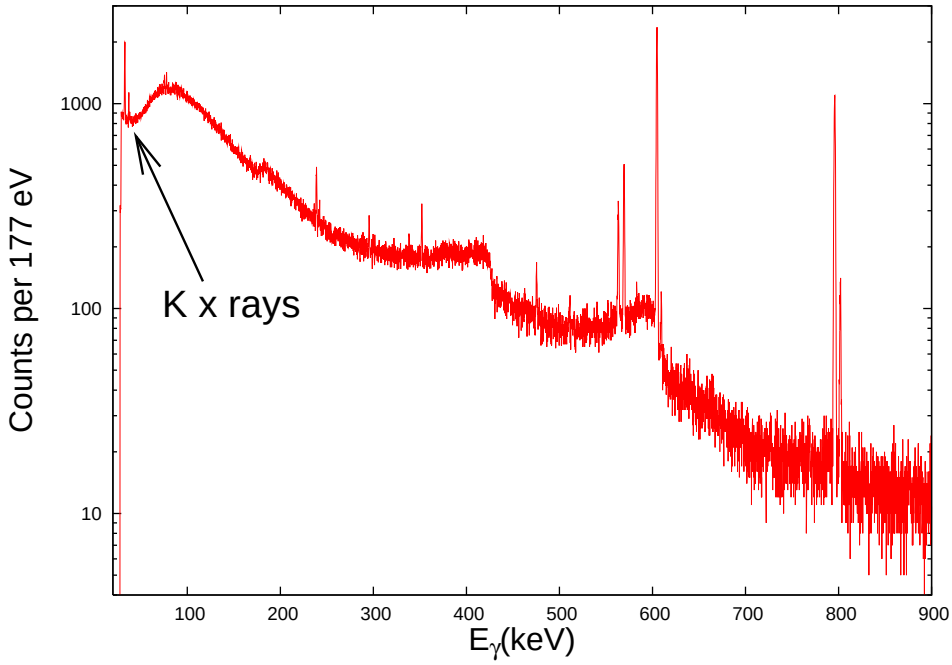

Figure 4.3: ^{134}Cs γ-ray spectrum: the lines in this spectrum were used to fix the relative efficiencies between x rays and γ rays. The x rays fitted in Figure 4.2 are visible at the low energy end of the spectrum.

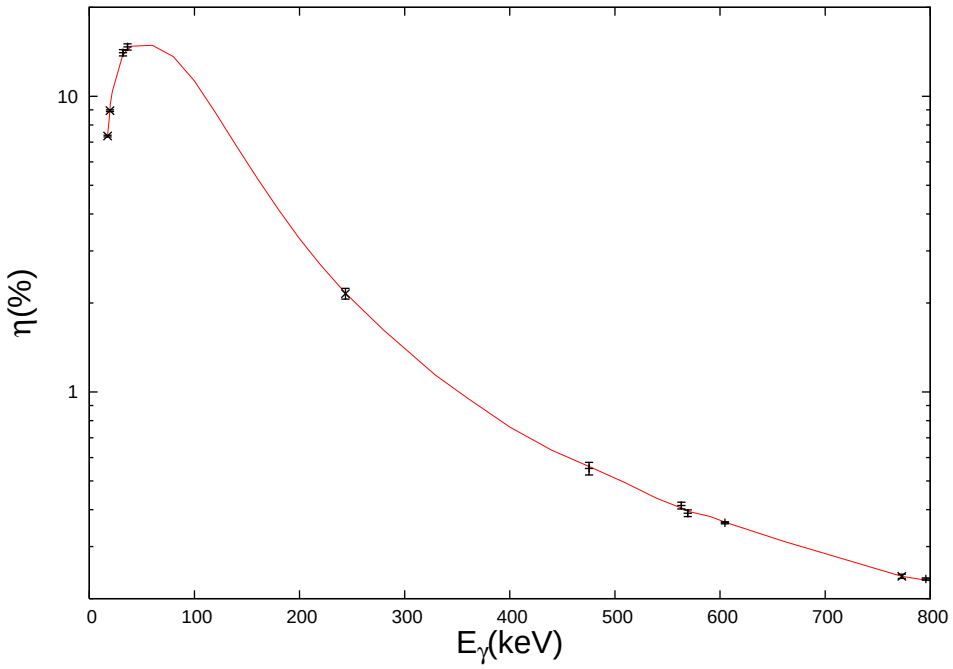

Figure 4.4: Ge detector calibration: the red curve comes from simulations with PENELOPE. The black points with error bars around a horizontal line are from the ^{134}Cs calibration source. The black points with error bars around a centered x are from ^{92}Tc.

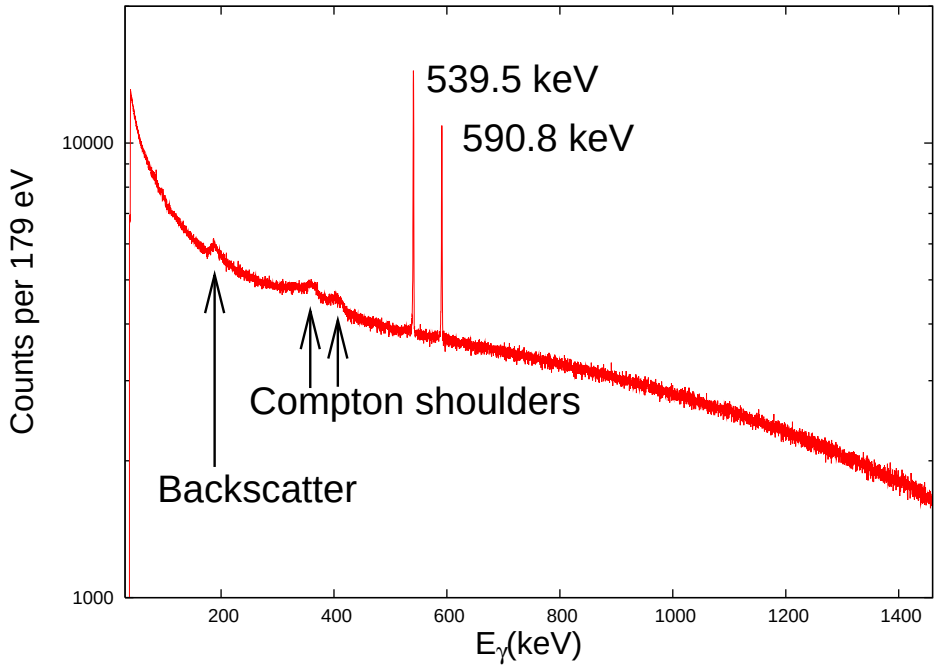

Figure 4.5: γ-ray spectrum taken from one run with ^{100}Tc beam, showing only the 539.5- and 590.8-keV γ rays and their Comptons, and a continuous beta background, and a Pb x ray from lead shielding showing at 74 keV.

and Mo-K transitions; c is a correction for the fraction of 590.8-keV γ rays lost from summing due to coincident 539.5-keV γ rays and beta particles, calculated from the same simulations used to determine the Ge detector efficiency; I_γ(590.8-keV) is the absolute intensity of the 590.8-keV γ ray; $f_K = 0.88$ is the fraction of EC decays that produce a vacancy in the K shell; and $\omega_K = 0.765$ is the total K-shell fluorescence yield [15], i.e., the probability of emission of a K-shell Mo x ray per K-shell vacancy. In practice, because the efficiency changes between the Kα and Kβ lines, we obtained A(Mo-K)/η(Mo-K) as the sum of A(Mo-K$_i$)/η(Mo-K$_i$) over all the individiual K-shell lines.

Over the course of several days running the experiment, we observed changes in the Ge detector's resolution. In our analysis we independently fit the x-ray spectrum from each run with resolution better than FWHM$\leq$ 700 eV in the x-ray region.

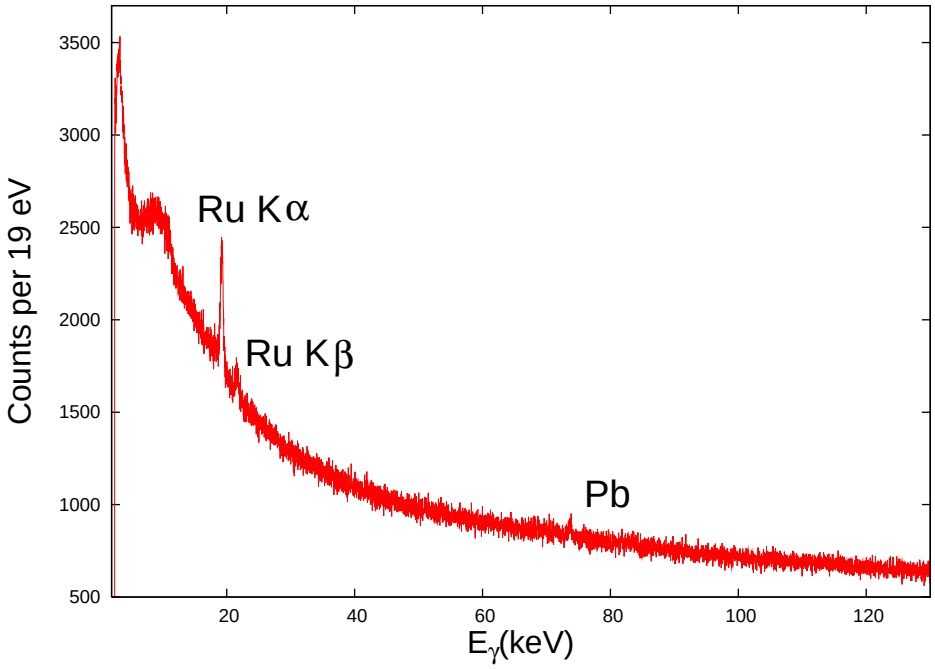

Figure 4.6: Raw x-ray spectrum from one run with ^{100}Tc beam. The Ru-Kα and Ru-Kβ lines are visible at 19.2 keV and 21.6 keV. A Pb x ray from lead shielding is visible at 74 keV.

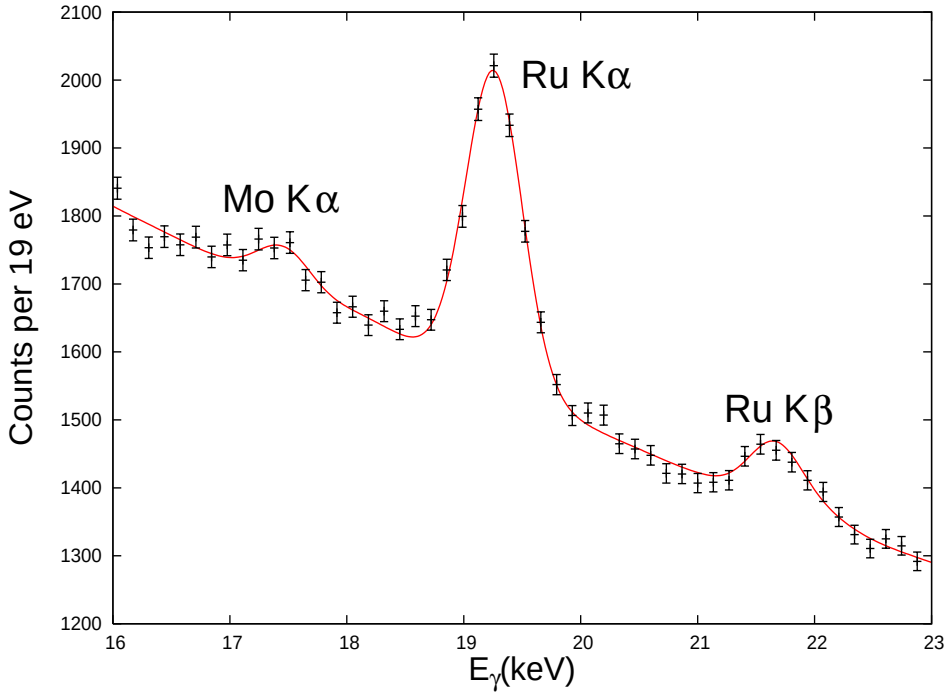

Figure 4.7: Fit to vetoed x-ray spectrum for five runs. Each x-ray peak from both isotopes was constrained during the fit to have an area equal to the product of one overall amplitude for the isotope, the fluorescence yield for each peak, and the efficiency of the Ge detector at the energy of each peak. The Mo Kα peak is at 17.4 keV, the Ru Kα peak is at 19.2 keV, and the Ru Kβ peak is at 21.6 keV. This fit yields $\chi^2/\nu = 1.042$ with $\nu = 394$.

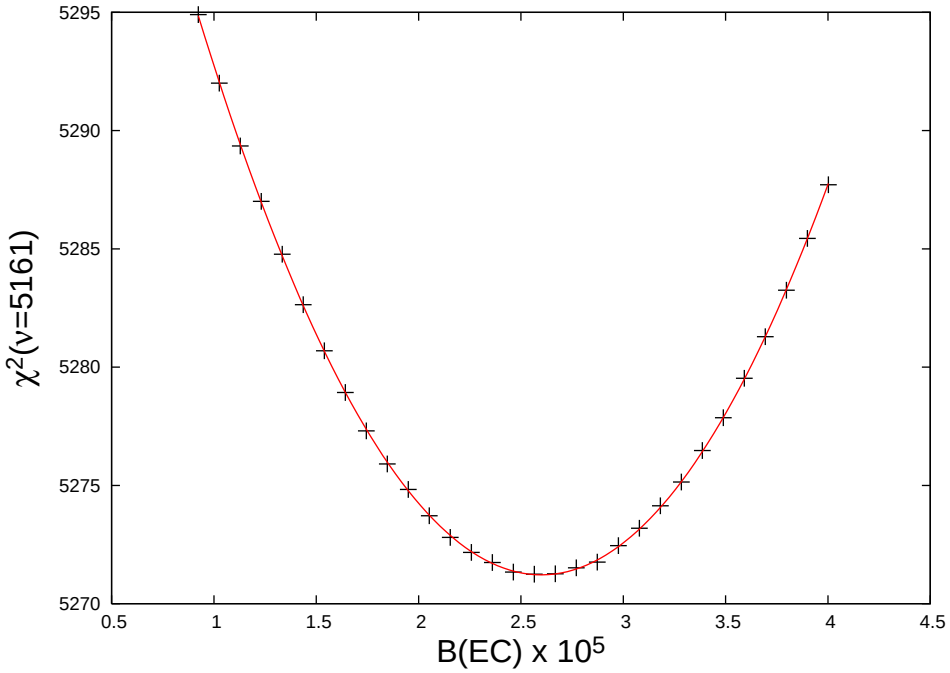

Figure 4.8: Plot of the cumulative χ^2 from 13 runs as a function of $B(\mathrm{EC})$.

To get the best value of the $B(\mathrm{EC})$ from all runs, including short runs from which one would individually obtain a value of $B(\mathrm{EC})$ statistically consistent with zero, we used the following scheme. For an assumed $B(\mathrm{EC})$, we calculated the number of Mo x rays expected given the number of 590.8-keV γ rays, fit the vetoed x-ray spectra from all runs with the Mo x-ray areas fixed, then added the total χ^2 for all runs. Figure 4.8 shows a plot of the results, from which we obtain

$$B(\mathrm{EC}) = (2.60 \pm 0.34 \pm 0.20) \times 10^{-5}, \tag{4.2}$$

in which the first uncertainty is statistical and the second uncertainty is due to the Ge detector calibration. Adding the uncertainties in quadrature yields $B(\mathrm{EC}) = (2.60 \pm 0.39) \times 10^{-5} \approx (2.6 \pm 0.4) \times 10^{-5}$; for simplicity, the latter will be used for discussions in Chapter 5.

This result is more precise than the previous determination [36]: $B(\mathrm{EC}) = (1.8 \pm 0.9) \times 10^{-5}$. That experiment did not use a high-resolution mass separator and con-

sequently had to make a separate measurement to determine the contributions from contaminants. Radioactivity was collected on a tape for several hours, then γ rays from the unwanted isotopes were measured, and finally the amount of Mo K-shell x rays due to the electron capture of ^{100}Tc during the experiment were deduced by accounting for veto efficiencies, branching ratios, and the effect of the periodic movement of the tape. This experiment avoids these difficulties and the limitations associated with depending on the measured branches from each contaminating isotope.

4.3 Corrections to Scintillator Signals

The decay of ^{100}Tc includes $\beta-\gamma$ coincidences that allowed calibration of the scintillator. By requiring the detection of a photon in the Ge detector, it is possible to obtain the scintillator's response for a beta-decay spectrum of known energy. But to use these data, it was necessary to correct the measurements from the scintillator.

Dead time played an important role in our analysis of the 539.5- and 590.8-keV γ-ray intensities. Due to decay rates as high as ≈ 20 kHz detected with $> 95\%$ efficiency in the scintillator, delays in our electronics became significant sources of dead time. See Appendix F for an explanation of the functional form of dead time corrections. For the following analysis, ten periods were selected from all the data for approximately constant event rates, then sorted individually. Figure 4.9 shows the events per unit time for Sort 1 from Table 4.1.

To calculate the necessary corrections, we begin by determining the scintillator's trigger rate as a function of m, the rate at which events are read from the ADC. Figure 4.10 shows a schematic of the relevant electronics. The dead time imposed on all gates to prevent signals from interfering with events being read from the ADC was $\tau_g = 100$ μs. An independent signal was recorded to count how many gates were from the scintillator. The number of scintillator triggers divided by the time interval of the sort determines R_0, the rate at which the scintillator triggered data acquisition. This signal was subject to the dead time, τ_g, imposed at the gate generator, so it follows that

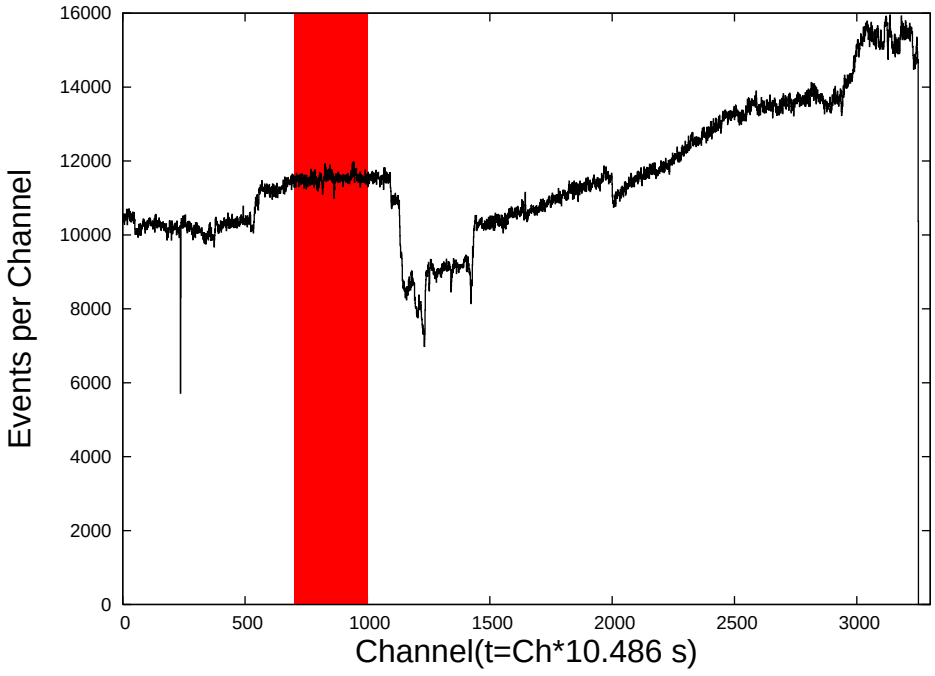

Figure 4.9: Rate gate for dead time corrections. The spectrum shows the number of events recorded by the ADC per unit time. The width of each channel is 10.486 s. The red region was selected for its approximately constant event rate. The average rate for the gate shown in the figure is $m = 1099.5$ Hz. The gate shown in this figure corresponds to Sort 1 from Table 4.1.

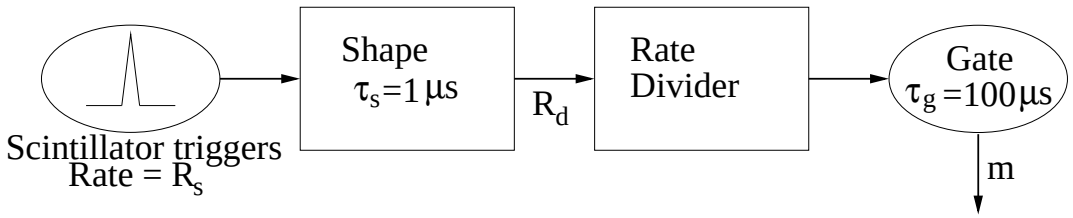

Figure 4.10: Schematic for dead time correction to raw scintillator signals. The scintillator trigger rate obtained from the ADC requires a correction for τ_g, the dead time imposed on gates to prevent pileup in the Ge detector. The rate from the rate divider requires a correction for τ_s, the width given to the pulses from the discriminator to make them work properly with the rate divider. For a more complete schematic of the electronics, see Figure 2.12.

the corresponding rate into the gate generator is

$$R_d = \frac{R_0}{1 - m\tau_g}. \tag{4.3}$$

Knowing R_d, the same form of correction but for the shorter dead time $\tau_s = 1\ \mu$s applies due to the shaping of the scintillator pulses before the rate divider. The rate from the scintillator itself is then

$$R_s = \frac{R_d}{1 - R_d\tau_s}. \tag{4.4}$$

Table 4.1 shows R_s calculated as a function of m from these two corrections.

A time-amplitude converter (TAC), which converts the time difference between two logic signals into a voltage, recorded coincidences between the Ge detector and scintillator to veto beta-decay events. It was imperative to trigger on the Ge signals to detect the maximum number of x rays, needed to measure the EC decays from ^{100}Tc. Because the PMTs have a much faster response time than the Ge detector's preamplifier, it was necessary to delay the signals from the scintillator to make them arrive after the Ge signals. The actual delay applied to the logic signals from the scintillator to stop the TAC during the experiment was $\tau_d = 19\ \mu$s.

To get the correction for the number of TAC signals, it was necessary to solve for the "observed" scintillator rate, m_s, from the delay unit to the TAC (see Figure 4.11).

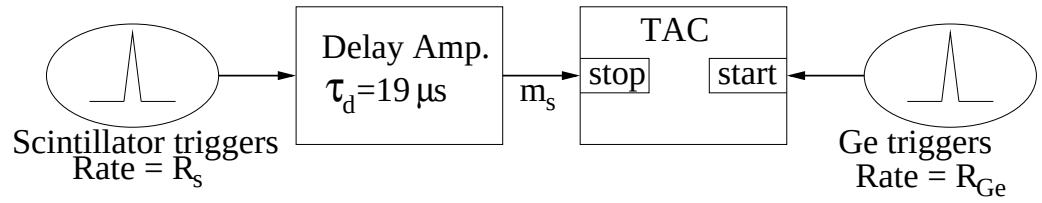

Figure 4.11: Schematic of dead time correction to TAC signals. Signals from the scintillator are lost because the delay unit is "dead" until the end of its delay period from the previous scintillator signal. For a more complete schematic of the electronics, see Figure 2.12.

Using the imposed delay time τ_d =19 μs to solve for R_s from

$$R_s = \frac{m_s}{1 - m_s\tau_d}, \tag{4.5}$$

one obtains the correction to the TAC signal:

$$C_{\text{TAC}} \equiv \frac{1}{1 - m_s\tau_d} = \frac{1}{1 - R_s\tau_d/(1 + R_s\tau_d)}. \tag{4.6}$$

The correction to the number of triggers from the scintillator, C_{st}, also has the same form but with $\tau_d \rightarrow \tau_s$ and $m_s \rightarrow R_d$. Both C_{TAC} and C_{st} for all ten rate sorts are shown in Table 4.1.

4.4 Scintillator Effficiency

We use the 590.8-keV γ ray to determine the efficiency of the scintillator. Direct beta-decay feeding of the ^{100}Ru excited state at $E_x = 1130$ keV accounts for 99.9% of the 590.8-keV γ-ray intensity [8], which makes it convenient to determine the scintillator's efficiency for a known beta-decay energy spectrum. To do this, we gate on the photopeak of the 590.8-keV γ ray and find the number of TAC signals.

The calibration procedure follows. Three coincidence spectra were taken, as shown in Figure 4.12: a low-energy background, a high-energy background, and a spectrum in coincidence with the 590.8-keV γ ray. The net number of coincidences from the TAC is given by

$$N_{\text{TAC}} = A_T(Ch_p) - A_T(Ch_1)\frac{Ch_p}{2Ch_1} - A_T(Ch_2)\frac{Ch_p}{2Ch_1}, \tag{4.7}$$

Table 4.1: Dead time corrections. m is the rate at which events were written from the ADCs. ΔT is the length of the sort's time interval. $N_{\mathrm{st}}/999$ is the number of scintillator triggers after the rate divider; these are non-integers because a background rate, which accounted for $< 0.6\%$ of the total rate in all sorts, has been subtracted. R_s is the rate coming from the scintillator, calculated from Equations 4.3 and 4.4. C_{TAC} and C_{st} are the corrections for N_{TAC} and $N_{\mathrm{st}}/999$ calculated from Equation 4.6 and its counterpart for N_{st}.

Sort	m(Hz)	ΔT(s)	$N_{\mathrm{st}}/999$	R_s(Hz)	C_{TAC}	C_{st}
1	1099.5	3156.3	25884.5	9290.3	1.1765	1.0093
2	982.1	996.2	7400.3	8297.6	1.1577	1.0083
3	1479.8	450.9	4913.2	12941.5	1.2459	1.0129
4	1291.8	2107.7	20217.5	11126.6	1.2114	1.0111
5	871.6	660.6	4347.2	7254.1	1.1378	1.0073
6	1247.2	2107.7	19156.5	10482.3	1.1992	1.0105
7	1858.6	1583.4	20145.5	15859.4	1.3013	1.0159
8	1912.3	2107.7	27923.5	16636.7	1.3161	1.0166
9	1901.7	2107.7	27249.5	16207.0	1.3079	1.0162
10	1980.9	3156.3	44210.5	17759.6	1.3374	1.0178

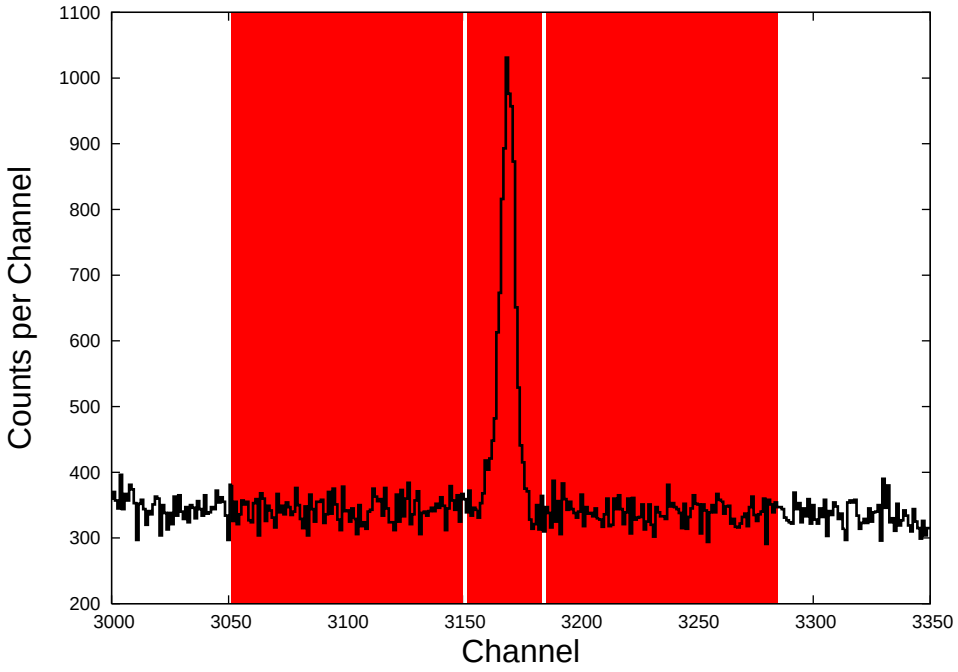

Figure 4.12: γ-ray gating scheme to measure scintillator coincidences: the number of coincident signals was determined for each of the three gated regions shown, to make a linear background subtraction. This is the actual 590.8-keV γ ray from Sort 1 of Table 4.1

in which Ch_1, Ch_2, and Ch_p are the number of channels in the respective gate for the low-energy background, high-energy background, and peak, and $A_T(Ch_i)$ is the number of TAC signals in coincidence with the Ge signals in gate i. Figure 4.13 shows the TAC peak obtained from the gate on the 590.8-keV γ ray in Figure 4.12. The corresponding scintillator efficiency is

$$\eta_s(E_x = 1130 \text{ keV}) = \frac{N_{\text{TAC}} C_{\text{TAC}}}{A(\gamma)}, \tag{4.8}$$

where $A(\gamma)$ is the net area of the photopeak in the γ-ray spectrum and C_{TAC} is the correction applied to the TAC signal due to dead time, given in Equation 4.6 and Table 4.1.

The scintillator's efficiency for this beta-decay branch was calculated for ten constant-

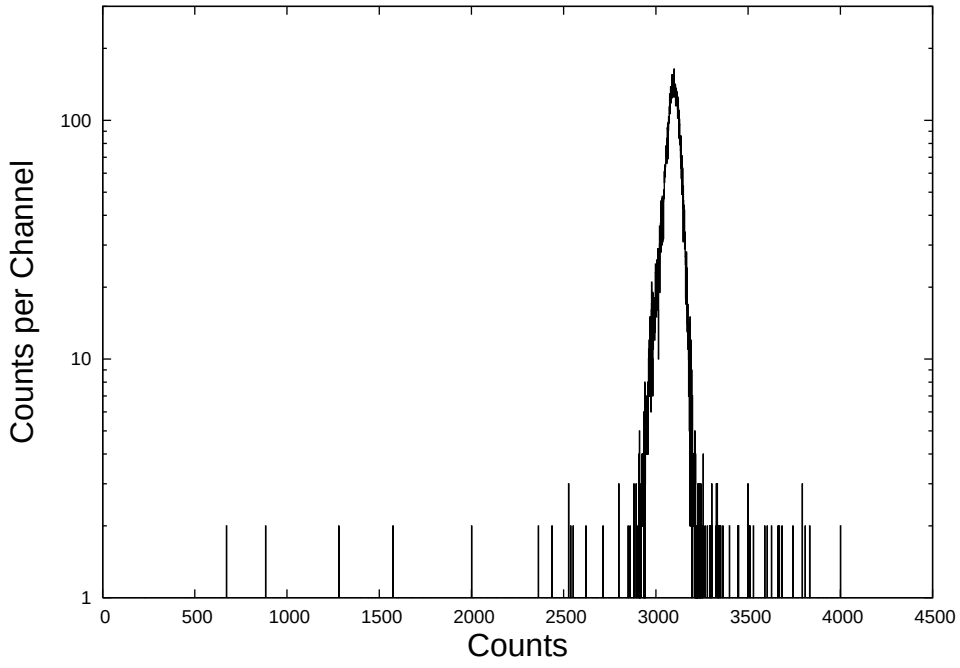

Figure 4.13: TAC peak obtained from gating on the 590.8-keV γ ray in Figure 4.12. This is the TAC peak corresponding to Sort 1 from Table 4.1 and to the gate on the photopeak in Figure 4.12. To obtain $A_T(Ch_p)$ from Equation 4.7, we take the area of this peak with a (small) background subtraction.

Table 4.2: Scintillator efficiency data. These data are from the same sorts listed in Table 4.1. $A(590.8\text{-keV})$ is the net area of the 590.8-keV γ ray from the sort. N_{TAC} is the net area of the TAC peak in coincidence with the γ ray, calculated using Equation 4.7. C_{TAC} is the correction to the TAC. η_s is the efficiency of the scintillator for each sort, as calculated by Equation 4.8. The fit gives $\chi^2/9 = 0.895$.

Sort	$A(590.8\text{-keV})$	N_{TAC}	C_{TAC}	$\eta_s(\%)$
1	5355(117)	4220.4	1.1765	92.7(2.2)
2	1537(66)	1246.2	1.1577	93.9(4.0)
3	989(51)	767.7	1.2459	96.7(5.0)
4	4082(100)	3094.2	1.2114	91.8(2.2)
5	858(43)	736.2	1.1378	97.6(4.9)
6	3885(102)	3176.8	1.1992	98.1(2.6)
7	3949(112)	2851.9	1.3013	94.0(2.7)
8	5264(135)	3890.9	1.3161	97.3(2.5)
9	5281(129)	3874.8	1.3079	98.4(2.4)
10	8628(165)	6235.3	1.3374	96.7(1.8)
LS fit				95.5(0.8)

rate sorts. A least-squares fit to these ten efficiencies gives

$$\eta_s(E_x = 1130 \text{ keV}) = 95.5 \pm 0.8\%, \tag{4.9}$$

which can be compared to the the same efficiency calculated using our simulations, $\eta_{\text{sim}}(E_x = 1130 \text{ keV}) = 95.4\%$. Table 4.2 shows the TAC and γ-ray areas from the sorts used to calculate the efficiency for the beta-decay branch to the ^{100}Ru excited state, $E_x = 1130$ keV. Figure 4.14 shows the measurement of the scintillator's efficiency, using the TAC signal corrected over a range of event rates.

We use the simulations, which showed excellent agreement with the measured scintillator efficiency for the $E_x = 1130$ keV excited state, to calculate the scintillator's average efficiency for all the decay branches of ^{100}Tc. Table 4.3 shows the simulation

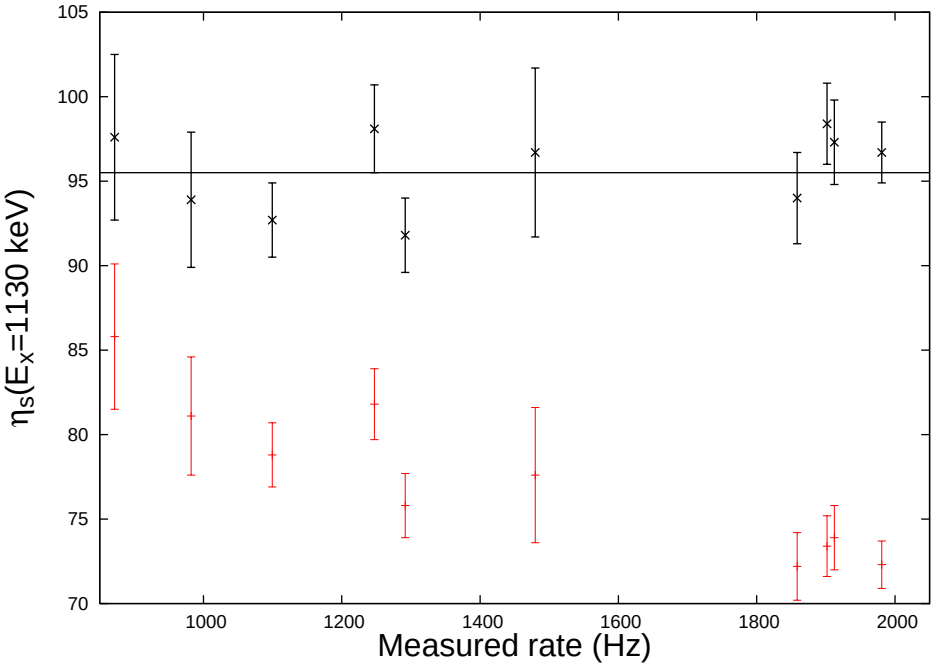

Figure 4.14: Scintillator efficiency as a function of data acquisition rate. The red points are prior to correction, the black points are corrected, and the overall fit of $\eta_s = 95.5 \pm 0.8\%$ gives $\chi^2/9 = 0.895$. The actual rates that determined the dead time correction were the scintillator rates, which were approximately an order of magnitude larger, approaching 20 kHz at its maximum. Table 4.1 gives the corrections and Table 4.2 gives the data used to calculate the efficiency.

Table 4.3: Simulated scintillator efficiencies obtained from PENELOPE using the design geometry for the scintillator and 1 mil for the thickness of the aluminum foil, measured with a micrometer. $c(\beta)$ is the calculated percentage of beta decays for each spectrum that deposit energy in the Ge detector.

E_0 (keV)	$\bar{E}$ (keV)	η_{sim} (%)	$c(\beta)$ (%)
3202.8	1351.1	98.1	11.2
2663.3	1099.3	97.1	8.0
2072.6	825.2	95.4	4.0
1151.3	415.0	86.9	0.5

results for each decay branch. The resulting average efficiency is $\bar{\eta}_{\text{sim}} = 97.9\%$. This average depends weakly on the decay-branch intensities assumed since the sum of the total intensity to all excited states is $I_x \approx 7\%$; the result is dominated by the efficiency for the ground state, $\eta_{\text{sim}}(E_x = 0 \text{ keV}) = 98.1\%$.

4.5 Calculation of γ Intensities

Given the scintillator's efficiency, $\bar{\eta}_{\text{sim}}$, and the number of triggers from the scintillator, N_{st}, we obtain the number of decays for the same rate-selected data as

$$N_D = \frac{N_{st} C_{st}}{\bar{\eta}_{\text{sim}}}. \tag{4.10}$$

The total number of decays should be related to the number of counts in the γ-ray photopeaks by the relationship

$$A(\gamma) = N_D I_\gamma \eta(E_\gamma)(1 - c), \tag{4.11}$$

in which A(γ) is the area in the photopeak of the γ ray, I_γ is the intensity of the γ ray, $\eta(E_\gamma)$ is the Ge detector's efficiency for the γ ray, and c is a correction for coincident beta particles and γ rays summing with the γ ray of interest in the Ge detector. The most directly accessible quantity from the data is the product $I_\gamma \eta(E_\gamma)(1 - c)$. Figure 4.15

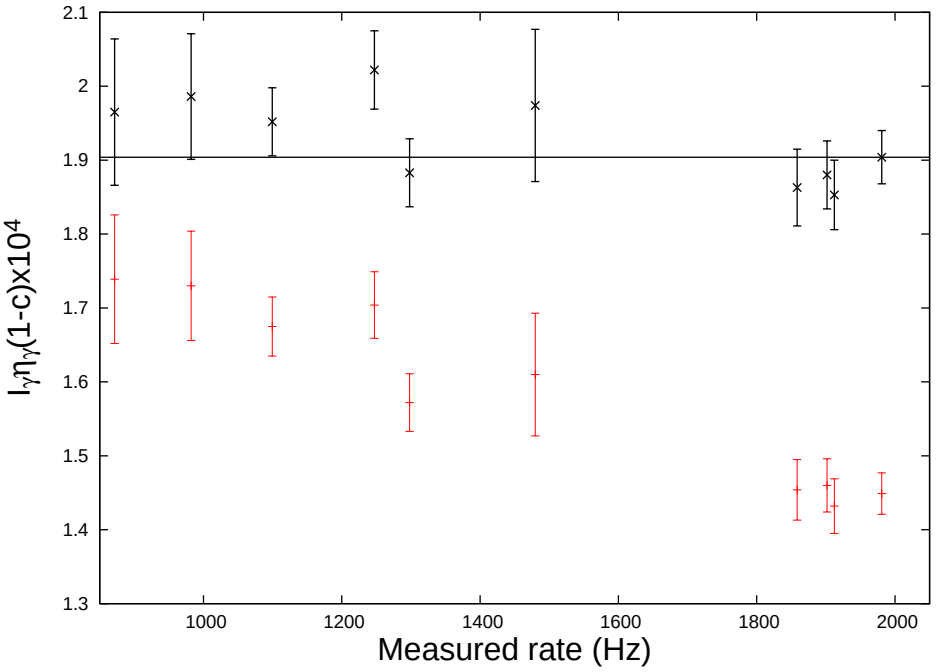

Figure 4.15: Weighted average of ten measurements of the 590.8-keV γ-ray intensity at different rates. The actual quantity measured is the product of the intensity, I_γ, the Ge detector's efficiency at E_γ =591 keV, η_γ, and a correction for summing from beta particles and γ rays coincident with the γ ray, $(1-c)$. The weighted average is $I_\gamma\eta_\gamma(1-c) = (1.904 \pm 0.019) \times 10^{-4}$. The average gives $\frac{\chi^2}{9} = 0.823$.

shows a least-squares fit to this quantity for the 590.8-keV γ ray, from which we obtain the 590.8-keV γ-ray intensity.

All values used to calculate $I_\gamma\eta(E_\gamma)(1-c)$ for the 590.8-keV γ ray are given in Tables 4.1 and 4.2. Calculating the same quantity for the 539.5-keV γ ray using the same scintillator calibration and the areas of the 539.5-keV γ rays from the same sorts, we find $I_\gamma\eta_\gamma(1-c)(\text{539.5-keV}) = (2.68 \pm 0.03) \times 10^{-4}$. Table 4.4 shows the values used to calculate both branches, from which we obtain

$$I_\gamma(\text{590.8-keV}) = 5.5 \pm 0.3\% \tag{4.12}$$

and

$$I_\gamma(\text{539.5-keV}) = 6.6 \pm 0.3\%. \tag{4.13}$$

Table 4.4: Values used to calculate γ-ray intensities. The corrections c take into account summing from beta particles and the other γ ray in the cascade, including the angular correlation between the two γ rays due to the $E2$ multipolarity of the transition.

E_γ (keV)	$I_\gamma \eta_\gamma (1-c)$ ($\times 10^4$)	$\eta(E_\gamma)$ (%)	c (%)
590.8	1.90(2)	0.379(17)	8.4(4)
539.5	2.62(3)	0.437(19)	9.1(5)

These intensities can be compared with the recent precision measurements [34, 32] of $I_\gamma(590.8\text{-keV}) = 5.5 \pm 0.3\%$ and $I_\gamma(539.5\text{-keV}) = 6.6 \pm 0.5\%$. The agreement is remarkable, considering the estimated 4.5% uncertainty in our calibration of the Ge detector's absolute efficiency. A weighted average of these two independent results yields

$$I_\gamma(590.8\text{-keV})_{\text{avg}} = 5.5 \pm 0.2\% \tag{4.14}$$

and

$$I_\gamma(539.5\text{-keV})_{\text{avg}} = 6.6 \pm 0.3\%. \tag{4.15}$$

4.6 Internal Ionization and Excitation

Our experiment allos us to determine the probability of K-shell internal ionization and excitation (IIE) [51] from the decay of ^{100}Tc. The Ru Kα x-ray peak in the raw x-ray spectrum originates mainly from three sources: internal conversion (IC) of the 539.5- and 590.8-keV γ rays, and IIE from the β^- decay of ^{100}Tc. In general, atomic vacancies are created predominantly by internal conversion (IC) of γ rays, but the contribution from IIE is approximately equal to the contribution from IC in the beta decay of ^{100}Tc because the gamma intensities are relatively small. The tabulated IC coefficients from Reference [15], the probability of a K-shell vacancy due to IC per γ ray emitted, are $e_K/\gamma(539.5) = 0.0038(2)$ and $e_K/\gamma(590.8) = 0.0030(2)$. Our data allows us to calculate $P_K(\text{IIE})$ from the relative number of Ru K-shell x rays in a raw x-ray spectrum versus

the number of 590.8- or 539.5-keV γ rays in a raw γ-ray spectrum. We find

$$P_K(IIE) = (7.2 \pm 0.6) \times 10^{-4}, \tag{4.16}$$

which can be compared with the result quoted in Reference [36], $P_K(\text{IIE}) = (6.0 \pm 0.6) \times 10^{-4}$. This reference used different values of the IC coefficients and would agree with our $P_K(IIE)$ value if the same IC coefficients were used.

4.7 Monte Carlo Simulations

The measured γ- and x-ray spectra from ^{92}Tc and ^{134}Cs were used to determine the Ge detector's relative efficiency as a function of energy. Simulations with PENELOPE using the experimental geometry, tuned to match the calibration spectra, determined the absolute efficiency and provided our interpolation from the energies of the lines in the calibration spectra to the 539.5- and 590.8-keV γ rays from the excited states of ^{100}Ru.

Figure 4.16 shows a cross section of the geometry used for simulations. The Ge detector's housing and the foil within the scintillator are both aluminum, represented by the green bodies. The BC-408 plastic scintillator consists of 1.032 g/cc of polyvinyl-toluene, represented by the blue body. The red body is the 0.254-mm thick Be window for the Ge detector. The Ge crystal is purple.

The parameters used to tune the simulations were a front and back dead layer on the Ge crystal. The front dead layer owes its explanation to boron ions implanted to make the p-type contact at the front of the crystal. Other phenomena that could produce similar x-ray attenuating effects include damage to the front layers of the crystal that affect charge collection and the presence of unknown attenuating materials. The PVT scintillator absorbs a fraction of the x rays comparable to the fraction absorbed by the front Ge dead layer. The method by which our simulations were tuned and the dead layers obtained are similar to those described as Set 2 in Reference [46], which a more rigorous calibration described as Set 3 in the same reference showed to be accurate to better than 1% for energies from 20 keV to energies greater than 1 MeV.

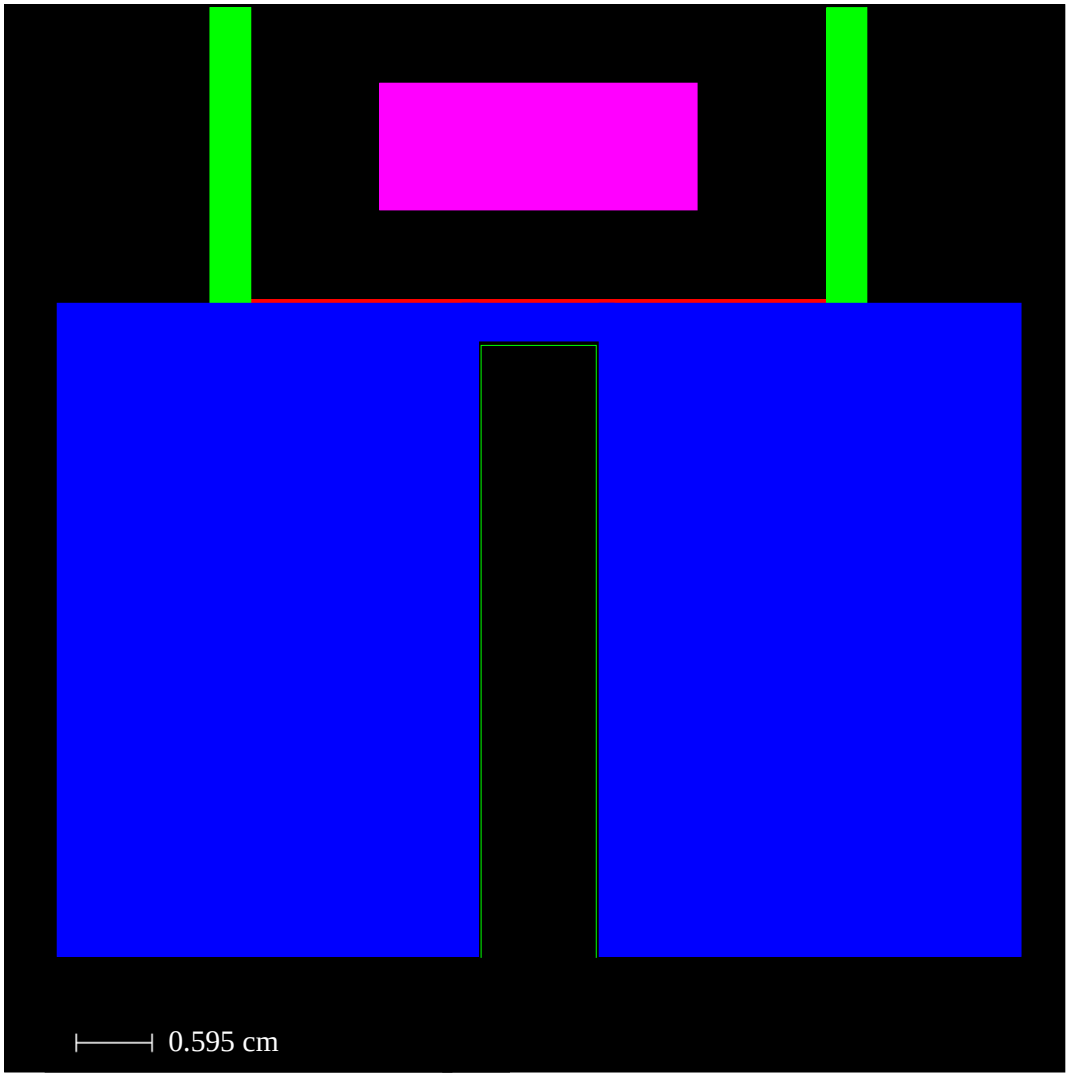

Figure 4.16: Geometry used in PENELOPE simulations. The magenta body is the Ge crystal. The blue body is the plastic scintillator. The green bodies are the aluminum housing of the Ge detector and foil inside the scintillator. The red body is the beryllium window of the Ge detector.

Table 4.5: Parameters for Compton shapes in x-ray fits: for the average energy of each Kα and Kβ peak, the Compton shoulder shape was included in the fit using these parameters. At each energy, a peak with the same FWHM as the photopeak and an amplitude equal to the amplitude of the photopeak multiplied by the factor under Amplitude.

X Ray	Energy (keV)	Amplitude	X Ray	Energy (keV)	Amplitude
Mo Kα	17.27	0.022	Mo Kβ	19.34	0.035
Mo Kα	16.90	0.043	Mo Kβ	18.84	0.038
Mo Kα	16.46	0.037	Mo Kβ	18.39	0.041
Mo Kα	16.02	0.013	Mo Kβ	17.95	0.012
Mo Kα	15.45	0.0032	Mo Kβ	17.49	0.0045
Ru Kα	18.908	0.0479	Ru Kβ	21.469	0.0311
Ru Kα	18.418	0.0270	Ru Kβ	21.005	0.0320
Ru Kα	18.040	0.0365	Ru Kβ	20.480	0.0394
Ru Kα	17.611	0.0109	Ru Kβ	20.050	0.0353
Ru Kα	17.146	0.0056	Ru Kβ	19.520	0.0100

The x-ray spectrum in Figure 4.1 shows excellent agreement between the shape of the Compton shoulder on the Mo Kα x ray from the fit and the ^{92}Tc x-ray calibration data. Compton shoulders were included for the Mo Kα, Mo Kβ, Ru Kα, and Ru Kβ x-ray peaks in all fits to the ^{100}Tc data. The shapes used in the fits, extracted from simulations, were given by five Gaussian amplitudes for each of the peaks, with energies and amplitudes fixed relative to the overall amplitude of the x-ray peak. The FWHM for the Gaussian distributions used to represent the Compton shoulders were kept the same as the FWHM of the photopeaks obtained in each fit, for functional simplicity. Table 4.5 shows the energies and amplitudes used to represent the Compton shoulder of each x-ray peak. Figure 4.17 shows a comparison between the PENELOPE simulation and the shape obtained from the peak plus five Gaussians for the Mo Kα peak.

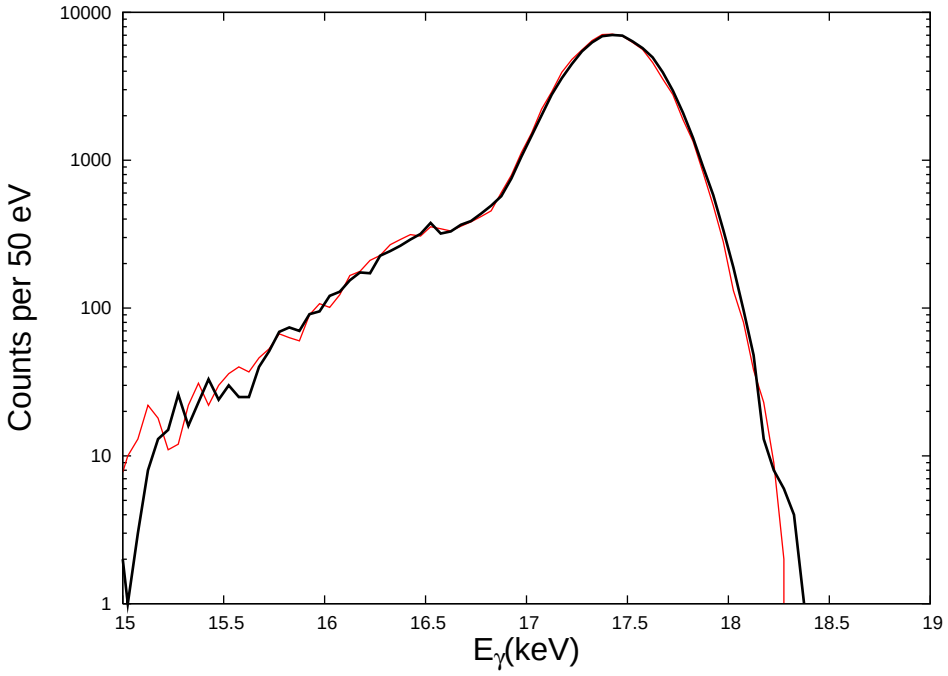

Figure 4.17: Comparison of PENELOPE simulation (thick black line) of a 17.44-keV peak to approximate the average Mo Kα energy and the form obtained from the five Gaussians listed in Table 4.5 (thin red line). Both the simulation and the fitting form have been given a FWHM of 509 eV for this comparison.

4.8 Systematic Uncertainties

The purification Penning trap ensured that only ions having $A = 100$ could reach the experimental setup. Neither the γ-ray nor x-ray spectra (Figure 4.5 and Figure 4.6) show any signs of contaminants.

Mo x rays could potentially be generated by fluorescence of ^{100}Mo, coming with the $A = 100$ beam and from the decay of ^{100}Tc. In order to check for this possibility we inserted a 1 μm-thick Pd foil between the scintillator and Ge detector and tried to observe fluorescence while taking the $A = 100$ beam. The amount of Pd in the foil is $\approx 10^{10}$ times greater than the total amount of Mo deposited during the entire experiment. No Pd x rays were observed; thus we exclude contamination of the Mo x rays by fluorescence.

Our calibration scheme determines the Ge detector efficiency as a function of photon energy. The simulations used for the efficiencies were also used to determine the summing corrections in our extraction of the γ-ray intensities (c in Equation 4.11). Uncertainties in the actual geometry of the experiment, including detector specifications for both the scintillator and Ge detector, could cause these values to be inaccurate. To account for these geometrical uncertainties, we calculated an uncertainty based on a shift in the detector's beam-axis position of 0.5 mm in both the summing corrections and the Ge efficiency, $\eta(E_\gamma)$. We also studied radial beam position and beam spread, which we found to be negligible.

For the calculation of $B(\text{EC})$ (Equation 4.1), the uncertainties in the summing correction c and the γ-rau efficiency $\eta(E_\gamma)$ are negligible because coincidence measurements with the scintillator determine the product $\eta(590.8\text{-keV})(1-c)I_\gamma(590.8\text{-keV})$ to 1% accuracy (as shown in Figure 4.15). The uncertainty in η(Mo-K) was determined from the fits explained in Section 4.1 to be 6.2%. This was added in quadrature to smaller effects due to experimental geometry and beam variations described above to determine an overall systematic uncertainty of 7.7% in our determination of $B(\text{EC})$. The same systematic uncertainty applies to the determination of P_K for IIE.

For our determination of $I_\gamma(590.8\text{-keV})$ and $I_\gamma(539.5\text{-keV})$, the estimated error due

to $\eta(E_\gamma)$ is 4.5%. The efficiencies of the higher energy x rays in the ^{134}Cs spectrum (Figure 4.2), which were used to determine the ratios between the efficiencies for the x rays and γ rays, show less sensitivity to the tuned parameters in our simulations. Corrections calculated for both the 590.8- and 539.5-keV γ rays include summing from both beta particles and the angular correlation between the $E2$ transitions in the $0^+ \rightarrow 2^+ \rightarrow 0^+$ γ-ray cascade.

Chapter 5

CONCLUSIONS

5.1 Calculation of $\log(ft)$

First we use our determination of $B(\mathrm{EC})$ to calculate the $\log(ft)$ for the electron-capture branch of ^{100}Tc. The most precise lifetime measurement [34] to date for ^{100}Tc is

$$T_{1/2}(^{100}\mathrm{Tc} \rightarrow ^{100}\ \mathrm{Ru}) = 15.27 \pm 0.05\ \mathrm{s}. \tag{5.1}$$

It follows from our branch measurement that the partial half-life

$$T_{1/2}(^{100}\mathrm{Tc} + e^- \rightarrow ^{100}\ \mathrm{Mo} + \nu_e) = 5.87^{+1.07}_{-0.78} \times 10^5\ \mathrm{s}. \tag{5.2}$$

We calculate the phase space using the tables of Reference [15], in which the total electron-capture decay rate is cited as

$$T^{-1} = \frac{G_\beta^2}{2\pi^3} \sum_x n_x C_x F_x \tag{5.3}$$

with n_x being the occupation number (all $n_x = 1$ for states with appreciable contribution to the EC of ^{100}Tc), C_x is the modulus squared of the nuclear matrix element, and F_x is the phase space given by

$$F_x = \frac{\pi}{2} q_x^2 \beta_x^2 B_x, \tag{5.4}$$

in which q_x is the neutrino energy in units of m_e for the capture of an electron with a particular binding energy, β_x is the amplitude of the bound-state electron radial function at the origin (nucleus), and B_x is a correction for exchange effects and imperfect atomic overlap between the parent and daughter nuclei.

Table 5.1 shows the numbers used to calculate the phase space. The result gives

$$\log(ft) = 4.29^{+0.08}_{-0.07} \tag{5.5}$$

for the EC decay of ^{100}Tc. This can be compared with the $\log(ft)$ values for the decays of ^{98}Zr and ^{102}Mo, for which $\log(ft) \approx 4.2$.

Table 5.1: ^{100}Tc atomic levels, binding energies BE, neutrino energy q_x in units of m_e, squared atomic wavefunctions with corrections, and the resulting contribution to the phase space. Only levels with contributions that are nonnegligible in the least significant digit shown have been included in the table. The stated error is due to the uncertainty in the value of Q_{EC}, propagated to the F_x via the uncertainty it implies in the neutrino energy, q_x.

Level	BE (keV)	q_x	$\beta_x^2 B_x$	F_x
K	21.0440	0.2876	0.2129	0.0277
L_1	3.0425	0.3228	0.02522	0.0041
L_2	2.7932	0.3233	3.937×10^{-4}	0.0001
L_3	2.6769	0.3235	0.001086	0.0002
M_1	0.5440	0.3277	0.004965	0.0008
N_1	0.0680	0.3286	9.186×10^{-4}	0.0002
Total				0.0331(24)

5.2 Implications for a pp neutrino Detector

Reference [20] estimated the amount of ^{100}Mo necessary to make a solar nuetrino detector. They used a value of $B(\mathrm{GT};^{100}\mathrm{Mo} \rightarrow^{100} \mathrm{Tc}) = 0.52 \pm 0.06$, extracted from a measurement of the charge-exchange reaction ^{3}He + ^{100}Mo $\rightarrow^3$H+^{100}Tc. Our direct measurement of $B(\mathrm{EC})$ also determines this $B(\mathrm{GT})$.

First we determine $B(\mathrm{GT})$ from $B(\mathrm{EC})$. We combine the result of Equation 5.2 with the calculated phase space using the relationship

$$T_{1/2}^{-1} = \sum_i f_i \frac{B(\mathrm{GT})_i}{D}, \tag{5.6}$$

in which $D = 6145.4(1.6)$ s. This value of D follows from the weighted average $\overline{\mathcal{F}T}_{1/2} = 3072.7(8)$ s for the superallowed decays between $T = 1$ nuclear analog states in Reference [42]. The matrix elements for these decays are given by $B(\mathrm{F}) = |M_F|^2 = |G_V|^2\langle\tau_+\rangle^2 = |G_V|^2 T(T+1) = 2|G_V|^2$, so it follows that $D = 2\overline{\mathcal{F}T}_{1/2}$.

Our determination of the EC branch gives the Gamow-Teller strength,

$$B(\text{GT};^{100}\,\text{Mo} \rightarrow^{100}\,\text{Tc}) = 0.95 \pm 0.16. \tag{5.7}$$

This determination of the Gamow-Teller strength is approximately 80% larger than the value used in Reference [20], so that the estimate would be revised to 1.6×10^3 kg of ^{100}Mo (17×10^3 kg of natural Mo).

5.3 Comparisons to QRPA Models for Double-Beta Decay

This section compares theoretical studies of the $A = 100$ system using the pn-QRPA approximation to our measurement. Griffiths and Vogel [41] performed QRPA calculations of both ground state to ground state single-beta decay strengths and the $2\nu\beta\beta$ decay strengths to both the ^{100}Ru ground state and the $E_x = 1130$-keV, $J^\pi = 0^+$ excited state. They used zero-range δ forces to approximate the residual interaction-strength parameters. Tuning the particle-hole proton-neutron interaction parameter, g_{ph}, to reproduce the observed energy of the Gamow-Teller (GT) giant resonance in ^{100}Tc, they found that values of the particle-particle proton-neutron interaction parameter, g_{pp}, which could reasonably reproduce both the $2\nu\beta\beta$ decay rates and the single-beta decay to the ground state of ^{100}Ru resulted in a very large value for the electron-capture decay strength: $B(\text{GT};^{100}\,\text{Tc} \rightarrow^{100}\,\text{Mo}) \approx 2.5$.

Suhonen and Civitarese [81] also used the QRPA to calculate the single-beta decay rates from ^{100}Tc to ^{100}Ru and ^{100}Mo and the $2\nu\beta\beta$ and $0\nu\beta\beta$ decay rates from ^{100}Mo to ^{100}Ru, and aditionally $E2$ transition strengths for both ^{100}Mo and ^{100}Ru and $0\nu\beta\beta$ decay rates. They used more realistic spatial dependences for their residual nucleon-nucleon interactions. They also tuned the g_{ph} parameter using the GT giant resonance. The particle-particle interaction parameter, g_{pp}, was determined by calculating the single-beta decay rate to the ground state of ^{100}Ru, $B(\text{GT};^{100}\,\text{Tc} \rightarrow^{100}\,\text{Ru})$. In this scheme, for a smaller and larger truncated set of single-particle states they calculated $B(\text{GT};^{100}\,\text{Tc} \rightarrow^{100}\,\text{Mo}) = 1.41$ and $B(\text{GT};^{100}\,\text{Tc} \rightarrow^{100}\,\text{Mo}) = 2.03$. These are both significantly larger than our measurement, $B(\text{GT};^{100}\,\text{Tc} \rightarrow^{100}\,\text{Mo}) = 0.32 \pm 0.05$.

Tuning the two parameters g_{ph} and g_{pp} does not appear adequate to reproduce the full set of observables. A recent paper by Faessler *et al* [28] shows that the three ground-state beta-decay observables may be reproduced simultaneously, for both of the double-beta decaying nuclei ^{100}Mo and ^{116}Cd, by fitting the axial vector coupling constant and allowing $g_A < 1$. One would assume that the similar structure of the $2\nu\beta\beta$ decay calculations to both the 0^+ ground state and 0^+ excited state would allow the calculations for both to be successfully scaled simultaneously, but their work does not mention a corresponding calculation and comparison with the experimentally-measured $2\nu\beta\beta$ decay rate to the 1130-keV, $J^\pi = 0^+$ excited state of ^{100}Ru. It remains to be seen how meaningful tuning these three parameters (g_A, g_{ph}, and g_{pp}) to reproduce three observables ($\tau(2\nu\beta\beta)$, $\tau(\mathrm{EC})$, and $\tau(\beta^-)$) will be for predicting $\mathcal{M}(0\nu\beta\beta)$.

5.4 ^{100}Tc Ground-State Contribution to $2\nu\beta\beta$ Decay Rates

In order to test the SSD hypothesis as precisely as possible, we use the calculations from Reference [76], in which the denominator in the matrix element,

$$\mathcal{M}_{fi} = \sum_m \frac{\langle {}^{100}\mathrm{Ru}||\sigma\tau||{}^{100}\mathrm{Tc}^m\rangle\langle {}^{100}\mathrm{Tc}^m||\sigma\tau||{}^{100}\mathrm{Mo}\rangle}{M_{\mathrm{Mo}} - E_{\beta 1} - E_{\bar{\nu}_e 1} - E_{\mathrm{Tc}^m}}, \tag{5.8}$$

was evaluated with the phase space integral. Their calculations found that the theoretical half lives obtained by performing the integral with the denominator intact were smaller than those obtained from a constant denominator using the approximation $\langle E_{\beta 1} + E_{\bar{\nu}_e 1}\rangle = Q_{\beta\beta}/2$. Their calculations yield a 20% reduction in the theoretical half-life for the $2\nu\beta\beta$ decay to the ground state of ^{100}Ru and a reduction of 18% for the $2\nu\beta\beta$ decay to the 0^+ excited state. Table 5.2 compares the results for the SSD hypothesis with the approximate denominator, the SSD hypothesis with the calculations of Reference [76], and recent measurements. In both cases, the double-beta decay contribution from only the ground state appears to be stronger than the *total* double-beta decay strength. It appears that contributions from higher levels of the intermediate nucleus must interfere destructively. These results suggest that the ground state plays an important role in the $2\nu\beta\beta$ decay rates.

Table 5.2: Predictions of the single-state dominance hypothesis versus experimental data for $2\nu\beta\beta$ decays of ^{100}Mo. The first column (SSD1) uses the approximation $\langle E_{\beta_1} + E_{\bar{\nu}_1} \rangle = Q_{\beta\beta}/2$. The second column (SSD2) includes the integrated denominator from Reference [76]. The third column lists experimental data from Reference [25] for comparison.

^{100}Ru level		$T^{2\nu\beta\beta}_{1/2}$-SSD1	$T^{2\nu\beta\beta}_{1/2}$-SSD2	$T^{2\nu\beta\beta}_{1/2}$-Experiment
J^π	E_x(keV)	(years)	(years)	(years)
0^+	0	$(6.2 \pm 0.9) \times 10^{18}$	$(5.0 \pm 0.7) \times 10^{18}$	$(7.3 \pm 0.4) \times 10^{18}$
0^+	1130	$(3.8 \pm 0.6) \times 10^{20}$	$(3.1 \pm 0.5) \times 10^{20}$	$(5.7^{+1.5}_{-1.2}) \times 10^{20}$
2^+	539.5	$(3.2 \pm 0.5) \times 10^{23}$	$(1.2 \pm 0.2) \times 10^{23}$	$> 1.1 \times 10^{21}$

5.5 Future possibilities

A proposed experiment using our scintillator again with the purification Penning trap at the IGISOL facilitiy will benefit from insights obtained during our analysis. Most significantly, any reduction in the delay of the scintillator signal to the TAC will lead to a corresponding reduction in the fraction of TAC signals that are lost because of dead time. The Ge detector gates were generated from the bipolar output of the amplifier that shaped the x-ray signals. Generating a faster trigger from the Ge detector independent of the spectroscopy amplifier and minimizing the timing between the Ge detector trigger and scintillator trigger for the TAC should already yield a 50% reduction in the dead time of the TAC. This will lead to more efficient veto, smaller backgounds, and a higher signal-to-noise ratio in the scintillator-vetoed x-ray spectra For instance, an easily-achieved reduction to a 10-μs delay for the TAC would result in approximately 20% less background in Figure 4.7.

Having demonstrated the viability of our experimental technique, we intend to apply it to the EC branch of ^{116}In, which holds interest as an intermediate nucleus with spin-parity $J^\pi = 1^+$ in another double-beta decay scenario. This decay has been directly measured previously, finding [9] $B(\text{GT}) = 0.75 \pm 0.21$. The $A = 116$ system

features beta-decay energies similar to the $A = 100$ system, $Q_{\beta^-} = 3274$ keV from ^{116}In to ^{116}Sn. $B(\mathrm{EC})$ is approximately a factor of 10 larger for ^{116}In due to the additional phase space available from the higher value of $Q_{\mathrm{EC}} = 470$ keV, compared with the value $Q_{\mathrm{EC}} = 168$ keV for ^{100}Tc. Thus the same experimental advantages of the trap and scintillator apply, but much higher x-ray production can be expected from the larger value of $B(\mathrm{EC})$. Naively assuming that all other factors (beam time, production from the source and trap, scintillator-veto efficiency, x-ray detection efficiency) will remain equal, $B(\mathrm{EC})$ being ten times larger should lead to ten times the number of observed x rays to signal EC events, and therefore approximately three times the precision of our measurement. If this were the case, the result using the same techniques with no improvements would be limited by systematic uncertainties and should yield a precision on the order of 10%.

^{116}Cd is another daughter nucleus in which the SSD hypothesis very nearly reproduces the measured double-beta decay rate, so there is motivation to pursue a more precise measurement. The $B(\mathrm{EC})$ of ^{116}Cd will provide another good test for QRPA calculations, which are expected to perform better for ^{116}In (the double-beta decay parent) because of smaller nuclear deformations.

Chapter 6

POLARIZED NEUTRON β-DECAY: THE PROTON ASYMMETRY AND RECOIL-ORDER CURRENTS

This chapter presents an analytic, recoil-order calculation of the proton asymmetry from polarized neutron β-decay. The differential decay rate in terms of electron energy and proton direction follows, parametrized in terms of the most general Lorentz-invariant hadron current coupled to a left-handed lepton current. Implications for experimental efforts to measure recoil-order currents are discussed.

6.1 Introduction

It is possible to calculate the decay distributions of the proton, electron and antineutrino from a polarized, free neutron due to the weak interaction with great precision within the framework of the standard model. In the case of neutron decay, electromagnetic effects are relatively small. Consequently, precision measurements of the decay distributions from polarized neutrons are good candidates in the search for new physics.

Measurements of the correlations from polarized free neutrons in conjunction with the neutron lifetime, τ_n, have been used to study the overall coupling constant, G_F, the ratio of the axial vector to vector couplings, to put limits on possible right-handed currents, and to probe for time reversal invariance-violating effects [26]. Given the neutron lifetime, $\tau_n \propto [|V_{ud}|^2 G_F^2 (1 + 3\lambda^2)]^{-1}$, it is also possible to extract the quark-mixing matrix element $|V_{ud}|$ from measurements of τ_n and λ, where λ is the ratio of axial vector to vector coupling in the hadron current. The value of $|V_{ud}|$ has important implications for the unitarity of the CKM matrix in conjunction with $|V_{us}|$ and $|V_{ub}|$ via the constraint $|V_{ud}|^2 + |V_{us}|^2 + |V_{ub}|^2 = 1$.

There are ongoing efforts to improve significantly on these measurements. The

first measurement of the beta asymmetry with ultracold neutrons was recently published [67].

6.2 Overview of Polarized Neutron β-decay Asymmetries

The purpose of this chapter is to present an anlytical formula for the proton asymmetry from polarized neutron decay including recoil-order effects. It is useful to expand the neutron's differential decay rate in terms of the electron's maximum energy divided by the neutron mass. We refer to this small, dimensionless quantity as R for recoil, $R \equiv max(E_e/m_n) \approx 0.001$. Both kinematic effects and terms in the interaction current proportional to the momentum transfer contribute at $\mathcal{O}(R)$. Taking these effects into account will play a role not only in searching for new physics, but also in extracting the standard-model form factors from combined measurements.

Excellent reviews on the effects of recoil-order corrections in beta decay already exist [48, 40, 43], so here we give a brief introduction. A common expression for the decay rate [52] is

$$d^5\Gamma = \frac{2|G_F|^2}{(2\pi)^5} E_e|\overrightarrow{p_e}|(E_0-E_e)^2\left[1+a\frac{\overrightarrow{p_e}}{E_e}\cdot\frac{\overrightarrow{p_\nu}}{E_\nu}+\overrightarrow{P}\cdot\left(A\frac{\overrightarrow{p_e}}{E_e}+B\frac{\overrightarrow{p_\nu}}{E_\nu}+D\frac{\overrightarrow{p_e}}{E_e}\times\frac{\overrightarrow{p_\nu}}{E_\nu}\right)\right]dE_e d\Omega_e d\Omega_\nu, \tag{6.1}$$

in which E_0 is the maximum electron energy, $\overrightarrow{p_e}$ and $\overrightarrow{p_\nu}$ are the momenta of the electron and neutrino, and E_e and E_ν are the energies of the electron and neutrino. $\overrightarrow{P}$ is the neutron's polarization. As can be seen from the equation a determines the $e-\nu$ correlation, A the beta asymmetry, B the neutrino asymmetry, and D is a T-odd term. The coefficients a, A, B, and D depend on the form of the interaction. Within the standard model and ignoring recoil-order effects and radiative corrections,

$$a = \frac{1-\lambda^2}{1+3\lambda^2}, A = \frac{2\lambda(1-\lambda)}{1+3\lambda^2}, \text{ and } B = \frac{2\lambda(1+\lambda)}{1+3\lambda^2}. \tag{6.2}$$

To first order ($\mathcal{O}(R)$), the neutrino exhibits a large asymmetry ($B \approx 0.98$) and the electron exhibits a small asymmetry ($A \approx -0.1$, see Figure 6.3).

Because the neutron is a composite object, the weak current contains terms in addition to those found for point-like particles, and the most general possible (Lorentz

invariant) V-A hadron current can be written with six dimensionless constants (form factors), three vector (f_i) and three axial vector (g_i). Parametrizing these currents in terms of the momentum transfer leads to a matrix element of the form

$$\mathcal{M} = \frac{G_F}{\sqrt{2}}\langle p|J^\mu(q^2)|\overrightarrow{n}\rangle \times \overline{e}(p_e)\gamma_\mu(1-\gamma_5)\nu(p_\nu), \tag{6.3}$$

in which

$$\langle p(p')|J^\mu|n(p,\overrightarrow{s})\rangle = \overline{p}(p')\Big[f_1\gamma^\mu - i\frac{f_2}{m_n}\sigma^{\mu\nu}q_\nu + \frac{f_3}{m_n}q^\mu - g_1\gamma^\mu\gamma_5 + i\frac{g_2}{m_n}\sigma^{\mu\nu}\gamma_5 q_\nu - \frac{g_3}{m_n}\gamma_5 q^\mu\Big]n(p,\overrightarrow{s}). \tag{6.4}$$

Here $q^\mu = p^\mu - p'^\mu$ is the momentum transfer, which is equal to the difference between the neutron (p^μ) and proton (p'^μ) momenta. m_n and $\overrightarrow{s}$ are the neutron's mass and spin.

Because the mass of the neutron is of order 1 GeV, while the momentum transfer in its decay is ≈ 1 MeV, the recoil-order effects are of order 0.1%. All the vector (f_i) form factors are related to the isovector electromagnetic form factors of the nucleon via the Conservation of the Vector Current (CVC) hypothesis [30, 38]:

$$\begin{aligned} f_1 &= 1 \\ f_2 &= \frac{\mu_p - \mu_n}{2} \\ f_3 &= 0. \end{aligned} \tag{6.5}$$

Both the terms with f_3 and g_2 are called Second Class Currents (SCC) [83]. Within the standard model and assuming isospin to be an exact symmetry, f_3 and g_2 should be zero, but due to differences between the quark wave functions within the neutron and proton one expects [19, 74] g_2/g_1 in the range $\approx 0.01 - 0.05$. Presently the best value of g_2 comes from an experiment in the $A = 12$ system [62], which found $2g_2/g_1 = -0.15 \pm 0.12 \pm 0.05$(theory). The pseudoscalar term g_3 only results in smaller terms that don't contribute to $\mathcal{O}(R^2)$.

Measurements of neutron decay have a distinct advantage over experiments with composite nuclei in terms of systematic uncertainties, since one need not account for the effects of the many-body nuclear system. In a composite nucleus, the observables used to search for second-class currents include contributions from first-class currents. In order to disentangle the effects of these two types of couplings, it is necessary to

measure both β^+ and β^- decays from mirror nuclei. It is also necessary to calculate and compensate for the two separate nuclear transition matrix elements to the daughter nucleus to use the data from the mirror nuclei.

The neutron is simply three quarks in a bound state. Precision measurements of the parity-breaking beta and proton asymmetries with respect to the neutron spin could provide better tests of the recoil-order terms within the weak interaction hadron current. To this end, we present a calcuation of the proton asymmetry.

Much work has been done on recoil-order effects in the weak interaction. Recoil-order calculations of the lepton asymmetry were performed by Harrington [43] for the polarized weak hadron decays of the neutron, Σ^-, Λ, and Ξ. A very general treatment within "effective field theory" covering various asymmetries and correlations of both composite nuclei and hadrons was published by Holstein [48]. Recently, Gardner and Zhang [37] gave results specialized to the neutron for the β-asymmetry and $e\nu$ correlation. Glück and Toth [39] numerically calculated asymmetries, including the recoil asymmetry. Notably missing from all this work is an analytic calculation of the recoil asymmetry. We performed an analytic calculation of the recoil asymmetry for completeness, maximum insight into possible systematic errors, and to get access to as many analysis tools as possible for neutron β-decay. It is experimentally possible to measure both the electron and the proton from neutron β-decay. Several experimental collaborations [85, 67, 69] are making precision measurements of A and the recoil asymmetry; hopefully calculations of the recoil asymmetry will prove useful in subsequent analyses.

In the process of evaluating the proton asymmetry, it was natural to reevaluate the hadronic matrix element. We found small differences with previous calculations that are listed under [43]. Evaluation of the matrix element in the rest frame of the neutron leads to a general expression of the form

$$\boldsymbol{M} = C_1 + \overrightarrow{P} \cdot (C_2 \overrightarrow{p_e} + C_3 \overrightarrow{p_\nu} + C_4 (\overrightarrow{p_e} \times \overrightarrow{p_\nu})) \,, \tag{6.6}$$

in which each C_i is a function of the four-momenta p_e, p_p, and p_ν. We performed recoil-order calculations of a and A, obtaining agreement with the results of Gardner and

Zhang [37]. Experimentally, current values of these parameters are $\lambda = -1.2695 \pm .0029$, $a = -0.103 \pm .004$, and $A = -0.1173 \pm 0.0013$ [26].

6.3 Calculation of the Proton Asymmetry

The desired new observable is the decay rate in terms of electron energy and proton angle, or $\frac{d^2\Gamma}{dE_e d(\cos\theta_p)}$. The easiest way to calculate this is to first integrate over $d^3\overrightarrow{p_\nu}$, then $d(\cos\theta_{ep})$. In order to obtain the asymmetry term C_3 as a function of $\overrightarrow{p_p}$ instead of $\overrightarrow{p_\nu}$, simply substitute $\overrightarrow{p_\nu} = -\overrightarrow{p_e} - \overrightarrow{p_p}$. With the limits $\cos(\theta_{ep}) = \pm 1$, conservation of energy and momentum give three limiting equations,

$$\begin{aligned} |\overrightarrow{p_\nu}| = E_\nu = \quad (m_n - E_e - E_p) = \quad & |\overrightarrow{p_e}| + |\overrightarrow{p_p}|, \\ & |\overrightarrow{p_e}| - |\overrightarrow{p_p}|, \text{ and} \\ & |\overrightarrow{p_p}| - |\overrightarrow{p_e}|. \end{aligned} \tag{6.7}$$

The first two provide lower limits of the integral over proton momentum for low and high electron energies, respectively, and the last is an upper limit for all electron energies. The first of the two lower limits applies when $\overrightarrow{p_e}$ is smaller than $\overrightarrow{p_\nu}$, which is equivalent to $E_e < E_e^c$, where E_e^c is the solution to $\overrightarrow{p_e} = \overrightarrow{p_\nu}$. The second lower limit applies when $\overrightarrow{p_e}$ is larger than $\overrightarrow{p_\nu}$, or when $E_e > E_e^c$. These limits reflect the fact that in the neutron's rest frame at very low electron energies, the recoil momentum must oppose the neutrino momentum; similarly at high electron energies, the recoil momentum must oppose the electron's momentum.

It is simplest to express the result in terms of the dimensionless recoil variables. To this end, we define

$$\begin{aligned} R \equiv \quad & \frac{E_0}{m_n} && = \frac{m_n^2 + m_e^2 - m_p^2}{2m_n^2} \approx .0014, \\ x \equiv \quad & \frac{E_e}{E_0} && = E_e/(Rm_n), \\ \epsilon \equiv \quad & \left(\frac{m_e}{m_n}\right)^2 && \approx 3 \cdot 10^{-7}, \text{ and} \\ \beta \equiv \quad & \frac{p_e}{E_e}, && \\ x^c \equiv \quad & \frac{E_e^c}{E_0} && = \frac{m_n[(m_n - m_p)^2 + m_e^2]}{(m_n - m_p)[(m_n - m_p)(m_n + m_p) + m_e^2]} \\ & && \approx 0.578 \end{aligned} \tag{6.8}$$

and the limits for the integral over proton momentum become

$$\begin{aligned} p_p/m_n \equiv\ & y \\ y_- &= \frac{R(1-x)}{1-Rx(1+\beta)} - \beta Rx \quad (x < x^c) \\ y_- &= \beta Rx - \frac{R(1-x)}{1-Rx(1+\beta)} \quad (x > x^c) \\ y_+ &= \beta Rx + \frac{R(1-x)}{1-Rx(1-\beta)} \quad (\text{upper limit } \forall\ x). \end{aligned} \tag{6.9}$$

Two integrals are necessary to obtain the proton asymmetry, one for the portion dominated by the neutrino (E_e small) and one for the portion dominated by the electron. The results for the proton asymmetry follow (see Appendix), with all recoil-order terms included. See Figure 6.1 for a plot of the proton asymmetry. All plots are of the observable

$$\Lambda = 2(N_+ - N_-)/(N_+ + N_-), \tag{6.10}$$

where N_+ is the number of the given particle emitted in the hemisphere defined by a positive dot product with the direction of the neutron's polarization, and N_- is the number in the opposing hemisphere. Λ is 1 if the given particle is always emitted along the parent's polarization, 0 if the particle is emitted isotropically, and -1 if all emissions oppose the parent's polarization. Note that the value of the proton asymmetry ranges from $-\Lambda_\nu$ at $E_e = m_e$ to $-\Lambda_e$ at $E_e = E_0$.

The proton asymmetry follows, omitting a factor of $|f_1|^2$ so that f_1 is normalized to 1. The equations appear as if all form factors are real for the sake of brevity. To obtain the more general complex expressions, first separate all possible factors of λ^2 and replace with $|\lambda|^2$. All remaining expressions involve only two form factors. Take the real part of the product of one form factor and the complex conjugate of the other, *e.g.* $f_2 f_3 \rightarrow Re(f_2 f_3^*)$. (The only possible exception is a single factor of λ, which would imply $Re(f_1 g_1^*)$.) For completeness, the full matrix element is included in Appendix G.

$$\frac{d^2\Gamma}{dE_e d(\cos\theta_p)} = \frac{2|G_F|^2}{(2\pi)^3}(m_n R)^4 \beta x^2 (1-x)^2 [1 + A_p \cos\theta_p] \tag{6.11}$$

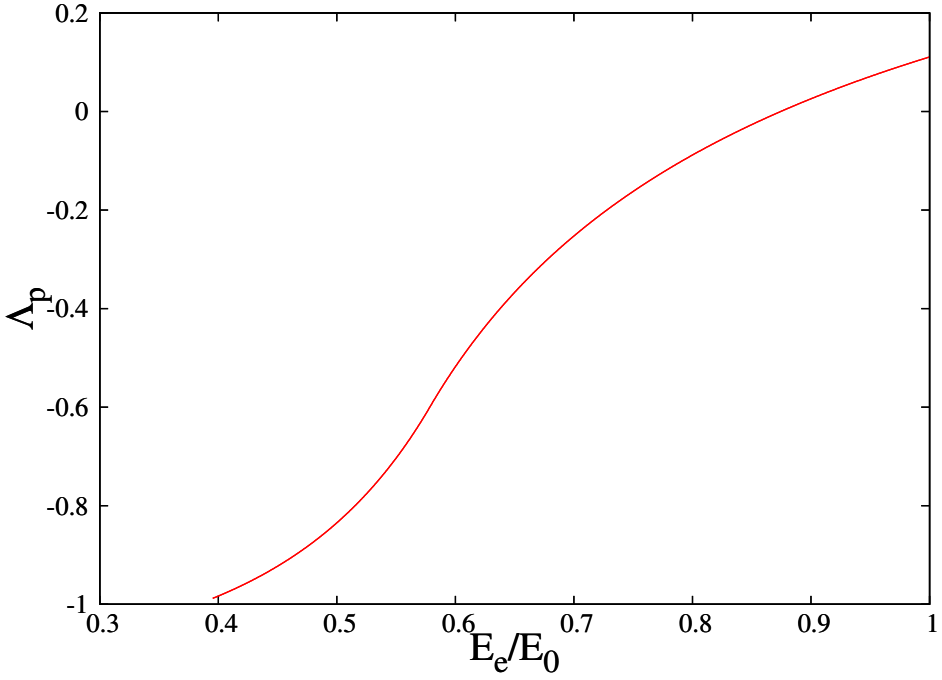

Figure 6.1: The proton asymmetry, with f_2 set to its CVC hypothesis value and all other recoil-order hadron couplings set to zero. Λ_p is equal to the observable $2(N_{p+} - N_{p-})/(N_{p+} + N_{p-})$.

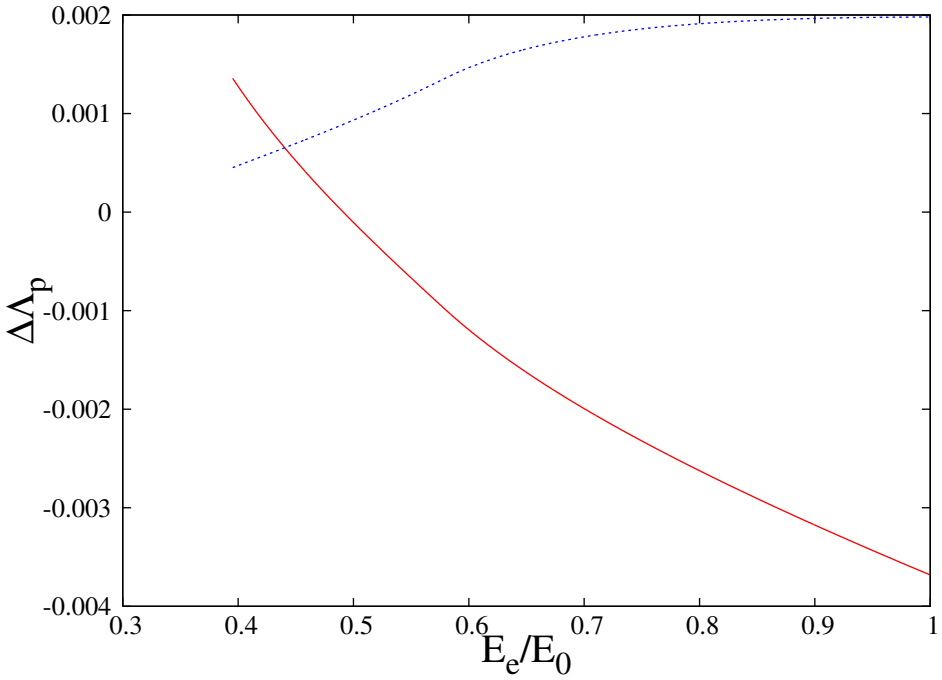

Figure 6.2: Possible changes in the proton asymmetry. The solid line is the change in Λ_p from f_2 set to the value predicted by the CVC hypothesis to $f_2 = 0$. The dashed line is the change in Λ_p from λ equal to the world average[26] to λ set to the world average plus its uncertainty, $\lambda + \Delta\lambda$.

$$
\begin{aligned}
A_p = \; & -\frac{2\lambda}{3(1-x)^2(1+3\lambda^2)} \times [3\lambda(1-x)^2 + 3(1-x)^2 + \beta^2 x((2-3x) + \lambda(-2+x))] \\
& R\frac{2}{3(1-x)^2(1+3\lambda^2)^2} \times \{\lambda[3(1-x)^3(\lambda^3 - \lambda^2 - \lambda + 1) \\
& +\beta^2 x(\lambda^3(-5+3x-4x^2-4\beta^2 x + \tfrac{19}{5}\beta^2 x^2) \\
& +\lambda^2(9-11x+4x^2-\tfrac{11}{5}\beta^2 x^2) + \lambda(-3+5x-4x^2+4\beta^2 x - \tfrac{27}{5}\beta^2 x^2) \\
& +(-1+3x-4x^2+\tfrac{3}{5}\beta^2 x^2))] \\
& +f_2\lambda[3\lambda^2(1-x)^2(x+2) + 3\lambda(1-x)^2(3x-4) + 6\lambda(1-x)^3 \\
& +\beta^2 x(\lambda^2(1-2x)(10x-7) + \lambda(7-8x+2x^2) - 6(1-x)^2) \\
& +\beta^4 x^2(\lambda^2(-8+\tfrac{53}{5}x) + \lambda(6-11x) + (2-\tfrac{4}{5}x))] \\
& +2f_2^2\lambda[\lambda(-3(1-x)^3 + \beta^2(1-x)(3-4x+2x^2) + \beta^4(1-x)(x-2)) \\
& -3(1-x)^3 + \beta^2(1-x)(3-8x+6x^2) + \beta^4 x(1-x)(2-3x)] \\
& +2f_2f_3\lambda^2[-3(1-x)^3 + \beta^2(1-x)(3-4x+2x^2) + \beta^4 x(1-x)(x-2)] \\
& +f_3\lambda[3\lambda x(1-x)^2 + x(1-x)^2 + \beta^2 x(\lambda(-3+4x-2x^2) + (-3+8x-6x^2)) \\
& +\beta^4 x^2(\lambda(2-x)) + (-2+3x)] \\
& +g_2[2\lambda^3(3(1-x)^3 + \beta^2 x(1-2x)(1-x) - \beta^4 x^2(2-x)) \\
& +\lambda^2(3(x-4)(1-x)^2 + \beta^2 x(1-10x+12x^2)) + \beta^4 x^2(4-\tfrac{27}{5}x) \\
& +3\lambda(3(1-x)^2 - \beta^2 x(2-x)) + (3x(1-x)^2 + \beta^2 x(1-2x) + \tfrac{1}{5}\beta^4 x^3)]\} + \mathcal{O}(R^2) \\
& (E_e < E_e^c)
\end{aligned}
\tag{6.12}
$$

$$
\begin{aligned}
A_p = \quad & \frac{2\lambda}{3\beta x^2(1+3\lambda^2)} \times [-\lambda(1-x^2)+(1-3x)(1-x)+3\beta^2x^2(\lambda-1)] \\
& -R\frac{2\lambda}{15\beta x^2(1+3\lambda^2)^2} \times \{(1-x)(2x^2+21x-13)+15\beta^2x^2(1-2x) \\
& +\lambda[-(1-x)(3-41x+28x^2)+5\beta^2x(2x+1)(2-3x)-30\beta^4x^3] \\
& +\lambda^2[-(1-x)(39-103x+34x^2)+5\beta^2x^2(1-10x)] \\
& +\lambda^3[31-28x-7x^2+4x^3+5\beta^2x(-2+3x-10x^2)+30\beta^4x^3] \\
& +f_2\lambda[-3(1-x)^2(3x+2)+5\beta^2x(1+4x-8x^2)-15\beta^4x^3] \\
& +10f_2^2\lambda[(3x-1)(1-x)^2+\lambda(x+1)(1-x)^2 \\
& +\beta^2(1-x)(1-4x+6x^2-\lambda(1+2x^2))+3\beta^4x^2(1-x)(1-\lambda)] \\
& +10f_2f_3\lambda[(1-x)^2((3x-1)+\lambda(x+1)+\beta^2(1-x)((1-4x+6x^2)-\lambda(2x^2+1)) \\
& +3\beta^4x^2\lambda(1-x)(1-\lambda)] \\
& +5xf_3\lambda[-(1-x)(3x-1)+\lambda(x^2-1)+\beta^2((-1+4x-6x^2)+\lambda(1+2x^2)) \\
& +3\beta^4x^2(1-\lambda)] \\
& +g_2[-2(1-x)(3x^2+4x-2)+10\lambda(x^2-1)+5\lambda^2x(x^2-1)-10\lambda^3(x+1)(1-x)^2 \\
& +10\beta^2x(-x+x^2+3\lambda x+\lambda^2(1-x+9x^2)+\lambda^3(1-x)(2x-1)) \\
& +15\beta^4x^3\lambda(1-\lambda)]\}+\mathcal{O}(R^2) \\
& (E_e > E_e^c)
\end{aligned}
\tag{6.13}
$$

6.4 Conclusions

The proton asymmetry could be used to measure f_2 and check its agreement with the CVC hypothesis. The absolute magnitude of the f_2 contribution to Λ_p(Figure 6.2) is approximately twice as large as the f_2 contribution to Λ_e, the beta asymmetry (Figure 6.4). The overall magnitude of the proton asymmetry is much larger, but the f_2 contribution results in a shift of 1.896 keV in the electron energy at which Λ_p crosses zero, which could be detected with sufficient precision. The proton distribution is isotropic at a higher electron energy if $f_2 = 0$.

SCC effects would be much harder to observe. Based on the current limit, g_2 could only contribute to Λ_p at 5% of the level at which f_2 does. To extract g_2 from a measure-

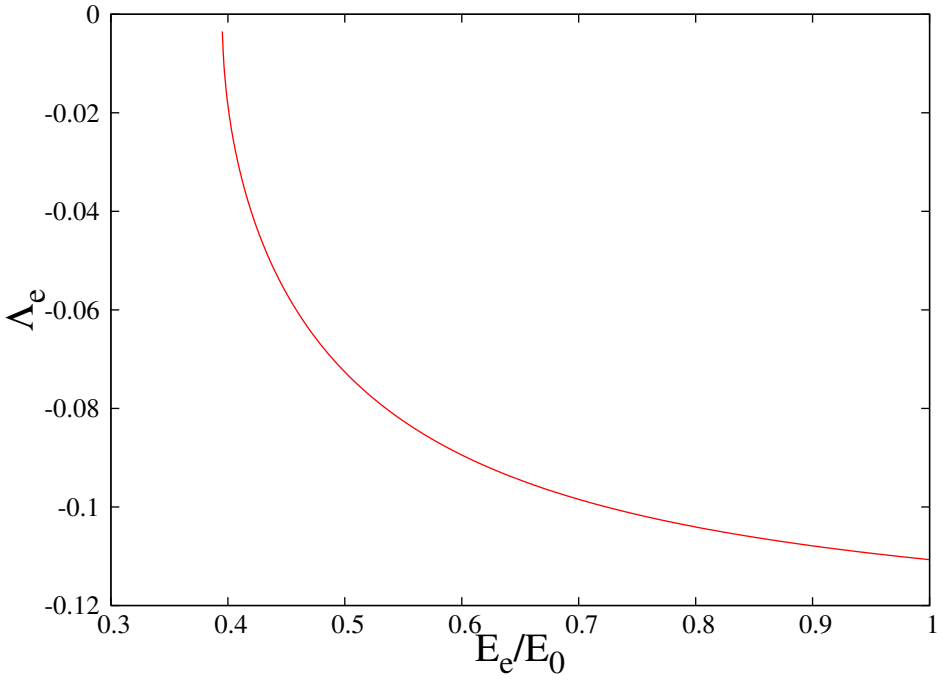

Figure 6.3: The beta asymmetry, with f_2 set to its CVC hypothesis value and all other recoil-order hadron couplings set to zero. The beta asymmetry is dominated by the overall factor $\beta = \frac{p_e}{E_e}$.

ment of Λ_p would require accuracy better than one part in ten thousand.

Incomplete knowledge of the polarization of the neutron could be a dominant systematic effect in experiments to measure decay asymmetries [58], so it is useful to consider a quantity that is independent of the polarization. The ratio Λ_p/Λ_e is independent of the neutron's polarization. Figure 6.5 shows the ratio Λ_p/Λ_e. Λ_p/Λ_e also shows sensitivity to the values of f_2 and λ. Figure 6.6 shows the change in Λ_p/Λ_e, which is at the 1% level. So not only is the ratio of the asymmetries independent of the neutron's polarization, it is also more sensitive to variations in the parameters λ and f_2 than either Λ_p or Λ_e alone.

In summary, we presented an analytical expression for the proton asymmetry from polarized neutron decay and used it in conjunction with a similar expression for the beta asymmetry to highlight advantages of a combined measurement.

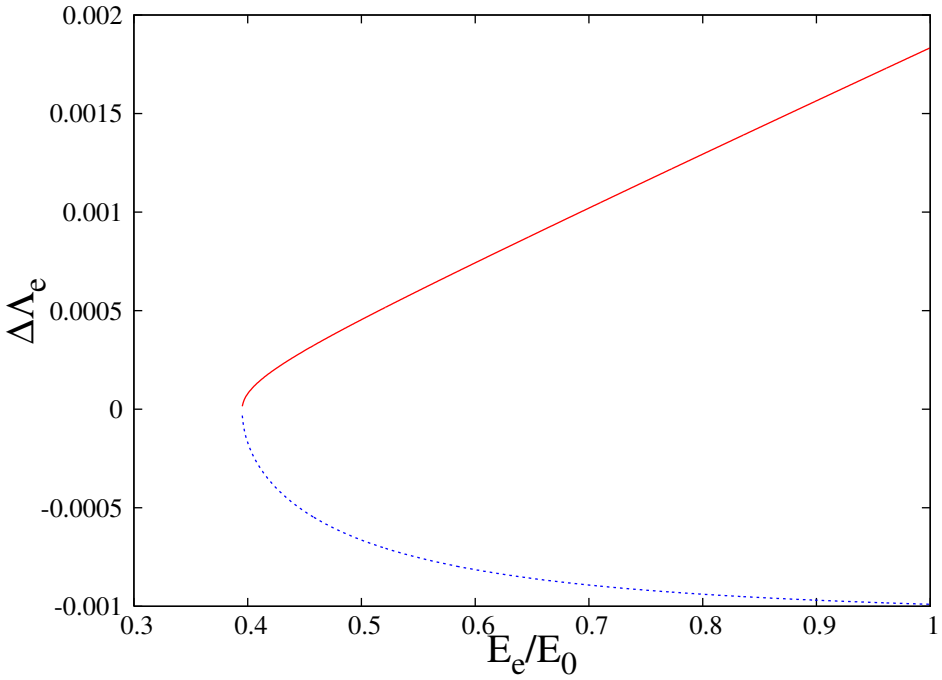

Figure 6.4: The possible changes in the beta asymmetry. The solid line is the change in Λ_e from f_2 set to the value predicted by the CVC hypothesis to $f_2 = 0$. The dashed line is the change in Λ_e from λ equal to the world average to λ set to the world average plus its uncertainty, $\lambda + \Delta\lambda$.

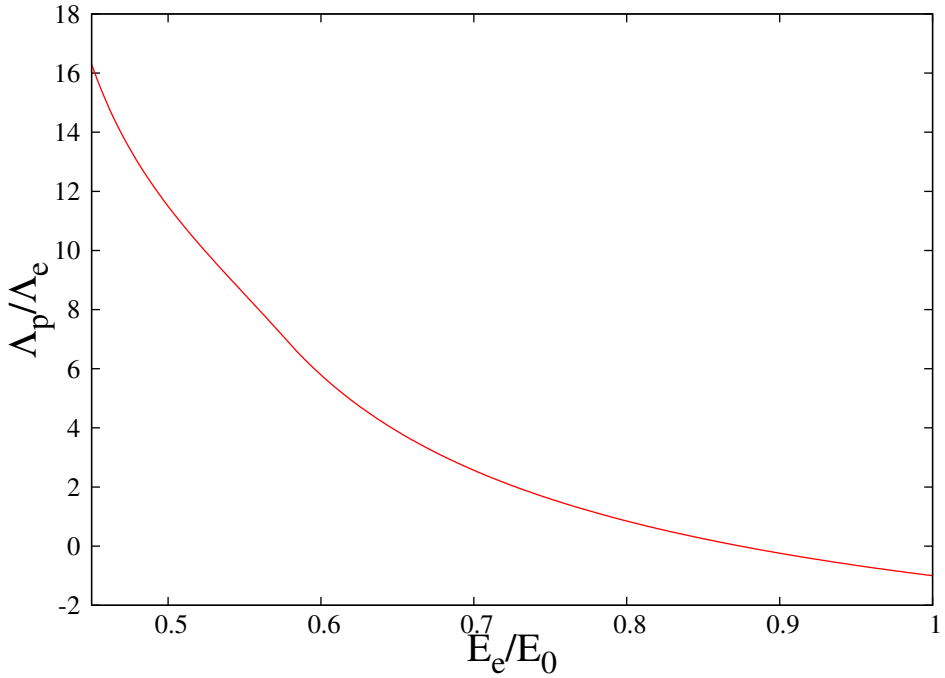

Figure 6.5: The ratio Λ_p/Λ_e, which is independent of the neutron's polarization, with f_2 set to its CVC hypothesis value and all other recoil-order hadron couplings set to zero. The plot excludes the lowest energies because the ratio diverges as $E_e \to m_e$ and $\Lambda_e \to 0$.

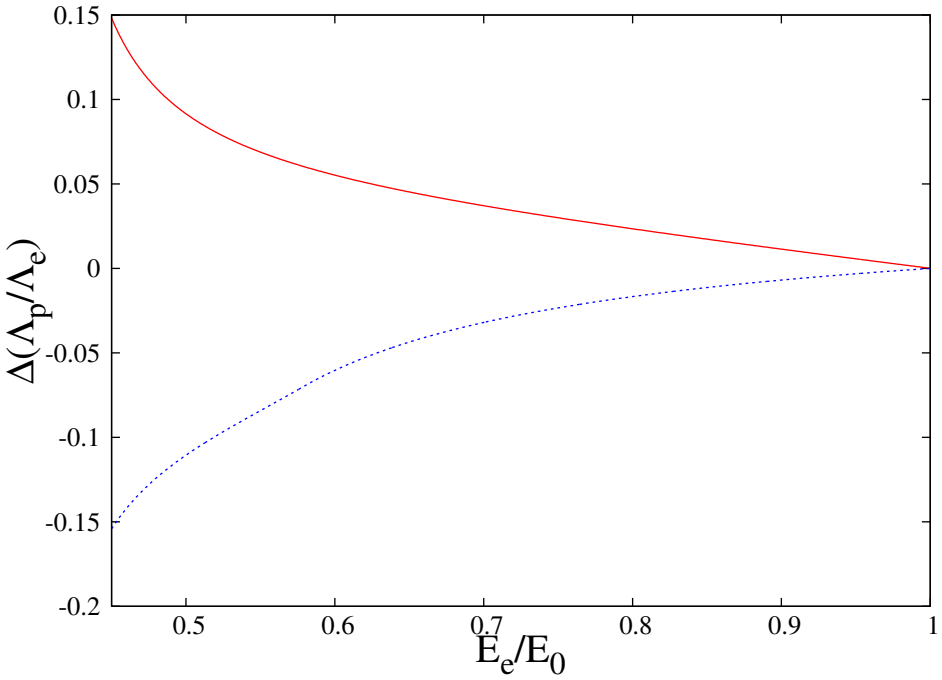

Figure 6.6: Changes in the ratio Λ_p/Λ_e. The solid line is the change in the ratio from f_2 set the value predicted by the CVC hypothesis to $f_2 = 0$. The dashed line is the change in the ratio from λ equal to the world average to λ set to the world average plus its uncertainty, $\lambda + \Delta\lambda$.

6.5 Comments

This work was previously published [78]. Since then, the proton asymmetry has been measured with 1% precision [75]. The magnitudes of various recoil-order currents based on supersymmetric extensions to the Standard Model have recently been estimated [66]. Next-generation proton asymmetry measurements, especially combined with the beta asymmetry, truly have the potential to text the limits of the standard model.

BIBLIOGRAPHY

[1] C. E. Aalseth and H. S. Miley. A self-calibrating pulse-shape discriminator for identifying neutrinoless double-beta decay events in HPGe spectrometers. *IEEE Nucl. Sci. Symp. Conf. Rec.*, pages 1250–1253, 2003.

[2] Hidetoshi Akimune, Hiroyasu Ejiri, Mamoru Fujiwara, Izuru Daito, Toru Inomata, Ryota Hazama, Atsushi Tamii, Hidenori Toyokawa, and Mosaru Yosoi. GT strengths studied by (3He,t) reactions and nuclear matrix elements for double beta decays. *Physics Letters B*, 394:23–28, 1997.

[3] J. Ärje, J. Äystö, H. Hyvönen, P. Taskinen, V. Koponen, J. Honkanen, K. Valli, A. Hautojärvi, and K. Vierinen. The ion guide isotope separator on-line, IGISOL. *Nuclear Instruments and Methods in Physics Research*, A247:431–437, 1986.

[4] R. Arnold, C. Augier, A. M. Bakalyarov, J. Baker, A. Barabash, Ph. Bernaudin, M. Bouchel, V. Brudanin, A. J. Caffrey, J. Cailleret, J. E. Campagne, D. Dassié, V. Egorov, K. Errahmane, A. I. Etienvre, T. Filipova, J. Forget, A. Guiral, P. Guiral, J. L. Guyonnet, F. Hubert, Ph. Hubert, B. Humbert, R. Igersheim anbd P. Imbert, C. Jollet, S. Jullian, I. Kisel, A. Klimenko, O. Kochetov, V. Kovalenko, D. Lalanne, F. Laplanche, B. Lavigne, V. I. Lebedev, J. Lebris, F. Leccia, A. Leconte, I. Linck, C. Longuemare, Ch. Marquet, G. Martin-Chassard, F. Mauger, I. Nemchenok, I. Nikolic-Audit, H. Ohsumi, S. Pécourt, F. Piquemal, J. L. Reyss, A. Richard, C. L. Riddle, J. Rypko, X. Sarazin, L. Simard, F. Sheibling, Yu. Shitov, A. Smolnikov, I. Stekl, C. S. Sutton, G. Szklarz, V. Timkin, V. Tretyak, V. Umatov, L. Vála, I. Vanushin, S. Vasiliev, V. Vasilyev, V. Vorobel, Ts. Vylov, J. Wurtz, and S. V. Zhukov. Technical design and performance of the NEMO 3 detector. *Nuclear Instruments and Methods in Physics Research A*, 536:79–122, 2005.

[5] R. Arnold, C. Augier, J. Baker, A. Barabash, G. Broudin, V. Brudanin, A. J. Caffrey, E. Caurier, V. Egorov, K. Errahmane, A. I. Etienvre, J. L. Guyonnet, F. Hubert, Ph. Hubert, C. Jollet, S. Jullian, O. Kochetov, V. Kovalenko, S. Konovalov, D. Lalanne, F. Leccia, C. Longuemare, G. Lutter, Ch. Marquet, F. Mauger, F. Nowacki, H. Ohsumi, F. Piquemal, J. L. Reyss, R. Saakyan, X. Sarazin, L. Simard, F. Šimkovic, Yu. Shitov, A. Smolnikov, L. Štekl, J. Suhonen, C. S. Sutton, G. Szklarz, J. Thomas, V. Timkin, V. Tretyak, V. Umatov, L. Vála, I. Vanushin, V. Vasilyev, V. Vorobel, and Ts. Vylov. First results of the search for neutrinoless double-beta decay with the NEMO 3 detector. *Physical Review Letters*, 95:182302, 2005.

[6] Juha Äystö. Development and applications of the IGISOL technique. *Nuclear Physics A*, 693:477, 2001.

[7] John N. Bahcall and M. H. Pinsonneault. What do we (not) know theoretically about solar neutrino fluxes? 2004.

[8] G. Berzins, M. E. Bunker, and J. W. Starner. Energy levels of ^{100}Ru. *Physical Review*, 187:1618–1632, 1969.

[9] M. Bhattacharya, A. García, M. M. Hindi, E. B. Norman, C. E. Ortiz, N. I. Kaloskamis, C. N. Davids, O. Civitarese, and J. Suhonen. Electron capture decay of ^{116}In and nuclear structure of double β decays. *Physical Review C*, 58:1247–1256, 1998.

[10] Klaus Blaum. High-accuracy mass spectrometry with stored ions. *Physics Reports*, 425:1–58, 2006.

[11] Georg Bollen. Traps for rare isotopes. *Lecture Notes for Physics*, 651:169–210, 2004.

[12] Martin M. Boyd, Andrew D. Ludlow, Sebastian Blatt, Seth M. Foreman, Tetsuya Ido, Tanya Zelevinsky, and Jun Ye. ^{87}Sr lattice clock with inaccuracy below 10^{-15}. *Physical Review Letters*, 98:083002, 2007.

[13] Lowell S. Brown and Gerald Gabrielse. Precision spectroscopy of a charged particle in an imperfect Penning trap. *Physical Review A*, 25:2423–2425, 1982.

[14] Lowell S. Brown and Gerald Gabrielse. Geonium theory: Physics of a single electron or ion in a Penning trap. *Reviews of Modern Physics*, 58:233–311, 1986.

[15] Edgardo Browne and Richard B. Firestone. *Table of Radioactive Isotopes*. John Wiley & Sons, Inc., 1986.

[16] E. Caurier, F. Nowacki, A. Poves, and J. Retamosa. Shell model studies of the double beta decays of 76ge, 82se, and 136xe. *Phys. Rev. Lett.*, 77(10):1954–1957, Sep 1996.

[17] Borexino Collaboration. First real time detection of ^{7}Be solar neutrinos by Borexino. *Physics Letters B*, 2008.

[18] The SNO Collaboration. An independent measurement of the total active ^{8}B solar neutrino flux using an array of ^{3}He proportional counters at the sudbury neutrino observatory. *Physical Review Letters*, 101.

[19] John F. Donoghue and Barry R. Holstein. Quark-model calculation of the weak electric coupling in semileptonic baryon decay. *Phys. Rev. D*, 25(1):206–212, Jan 1982.

[20] H. Ejiri, J. Engel, R. Hazama, P. Krastev, N. Kudomi, and R. G. H. Robertson. Spectroscopy of double-beta and inverse-beta decays from $100mo$ for neutrinos. *Phys. Rev. Lett.*, 85(14):2917–2920, Oct 2000.

[21] S. R. Elliott and P. Vogel. Double beta decay. *Annu. Rev. Nucl. Part. Sci.*, 52:115–151, 2002.

[22] T. Eronen, V.-V. Elomaa, U. Hager, J. Hakala, J. C. Hardy, A. Jokinen, A. Kankainen, I. D. Moore, H. Penttilä, S. Rahaman, S. Rinta-Antila, J. Rissanen, A. Saastamoinen, T. Sonoda, C. Weber, and J Äysto. Q_{EC} values of the superallowed β emitters ^{50}Mn and ^{54}Co. *Physical Review Letters*, 100:132502, 2008.

[23] Tommi Eronen. Precision mass measurements with penning traps; improvement of JYFLTRAP extraction efficiency. Master's thesis, University of Jyväskylä, 2003.

[24] Abad *et al. Ann. Fis.*

[25] C. Amsler *et al.* Particle data group. *Physics Letters B*, 667:1.

[26] S. Eidelman *et al*.

[27] W.-M Yao *et al*. Particle data group. *Journal of Physics G*, 33:1, 2006.

[28] A. Faessler, G. L. Fogli, E. Lisi, V. Rodin, A. M. Rotunno, and F. Šimkovich. Overconstrained estimates of neutrinoless double beta decay within the QRPA, 2008.

[29] Enrico Fermi. An attempt of a theory of beta radiation. 1. *Zeitschrift Fur Physik*, 88:161, 1934.

[30] R. P. Feynman and M. Gell-Mann. Theory of the fermi interaction. *Physical Review*, 109(1):193–198, 1958.

[31] Guido Drexlin for the KATRIN Collaboration. KATRIN - direct measurement of a sub-eV neutrino mass. *Nuclear Physics B*, 145:263–367, 2005.

[32] Kazuyoshi Furutaka, Hideo Harada, Shoji Nakamura, Toshio Katoh, Toshiyuki Fujii, Hajimu Yamana, and Subramanian Raman. Cross section of thermal-neutron capture reaction by ^{99}Tc. *Journal of Nuclear and Radiochemical Sciences*, 6:283–286, 2005.

[33] Kazuyoshi Furutaka, Shoji Nakamura, Hideo Harada, and Toshio Katoh. Evaluation of $\beta - \gamma$ coincidence measurement system using plastic scintillation β-ray detector developed for the determination of γ-ray emission probabilities of short-lived nuclides. *Journal of Nuclear Science and Technology*, 37:832–839, 2000.

[34] Kazuyoshi Furutaka, Shoji Nakamura, Hideo Harada, Toshiro Katoh, Toshiyuki Fuji, and Hajimu Yamana. Precise measurement of gamma-ray emission probabilities of ^{100}Ru. *Journal of Nuclear Science and Technology*, 38:1035–1042, 2001.

[35] A. García, E. G. Adelberger, P. V. Magnus, H. E. Swanson, D. P. Wells, F. E. Wietfeldt, and O. Tengblad. β-delayed γ-ray emission in Ca37 decay. *Physical Review C*, 51(2):R439–R442, Feb 1995.

[36] A. García, Y-D Chan, M. T. F. Cruz, R. M. Larimer, K. T. Lesko, E. B. Norman, R. G. Stokstad, F. E. Wietfeldt, I. Žlimen, D. M. Moltz, J. Batchelder, and T. J. Ognibene. Electron-capture decay of ^{100}Tc and the double-β decay of ^{100}Mo. *Physical Review C*, 47:2910–2915, 1993.

[37] S. Gardner and C. Zhang. Sharpening low-energy, standard-model tests via correlation coefficients in neutron β decay. *Phys. Rev. Lett.*, 86(25):5666–5669, Jun 2001.

[38] Murray Gell-Mann. Test of the nature of the vector interaction in β decay. *Phys. Rev.*, 111(1):362–365, Jul 1958.

[39] F. Glück and K. Tóth. Order-α radiative corrections for semileptonic decays of polarized baryons. *Phys. Rev. D*, 46(5):2090–2101, Sep 1992.

[40] Laszlo Grenacs. Induced weak currents in nuclei. *Annual Review of Nuclear and Particle Science*, 35:455–500.

[41] A. Griffiths and P. Vogel. Double-beta decay to excited 0^+ states: Decay of ^{100}Mo. *Physical Review C*, 46:181–187, 1992.

[42] J. C. Hardy and I. S. Towner. New limits on fundamental weak-interaction parameters from superallowed β decay. *Physical Review Letters*, 94:092502, 2005.

[43] D. R. Harrington. Lepton decays of hyperons. *Phys. Rev.*, 120(4):1482–1485, Nov 1960.

[44] W. C. Haxton and Jr. G. J. Stephenson. Double beta decay. *Jr. Prog. Part. Nucl. Phys.*, 12:409, 1989.

[45] Wick Haxton. Neutrino astrophysics. 2008.

[46] R. G. Helmer, J. C. Hardy, V. E. Iacob, M. Sanchez-Vega, R. G. Neilson, and J. Nelson. The use of monte carlo calculations in the determination of a Ge detector efficiency curve. *Nuclear Instruments and Methods in Physics Research A*, 511:360–381, 2003.

[47] G. Hinshaw, J. L. Weiland, R. S. Hill, N. Odegard, D. Larson, C. L. bennett, J. Dunkley, B. Gold, M. R. Greason, N. Jarosik, E. Komatsu, M. R. Nolta, L. Page, D. N. Spergel, E. Wollack, M. Halpern, A. Kogut, M. Limon, S. S. Meyer, G. S. Tucker, and E. L. Wright. Five-year wilkinson anisotropy probe (WMAP) observations: Data processing, sky maps, and basic results.

[48] Barry R. Holstein. Recoil effects in allowed beta decay: The elementary particle approach. *Rev. Mod. Phys.*, 46(4):789–814, Oct 1974.

[49] M. J. Hornish and L. De Braeckeleer. Double β decay of ^{100}Mo to excited final states. *Physical Review C*, 74:044314, 2006.

[50] J. Huikari, P. Dendooven, A. Jokinen, A. Nieminen, H. Penttilä, K. Peräjärvi, A. Popov, S. Rinta-Antila, and J. Äystö. Production of neutron deficient rare isotope beams at IGISOL; on-line and off-line studies. *Nuclear Instruments and Methods in Physics Research Section B*, 222:632–652, 2004.

[51] Yasuhito Isozumi. Effects of nuclear decay on atomic electron arrangements. *Nuclear Instruments and Methods in Physics Research A*, 280:151–160, 1989.

[52] J. D. Jackson, S. B. Treiman, and H. W. Wyld. Possible tests of time reversal invariance in beta decay. *Phys. Rev.*, 106(3):517–521, May 1957.

[53] Robert S. Van Dyck, Jr., Paul B. Schwinberg, and Hans G. Dehmelt. New high-precision comparison of electron and positron g factors. *Physical Review Letters*, 59:26–29, 1987.

[54] H. V. Klapdor-Kleingrothaus and I. V. Krivosheina. The evidence for the observation of $0\nu\beta\beta$ decay: the identification of $0\nu\beta\beta$ events from the full spectra. *Modern Physics Letters A*, 21:1547–1566, 2006.

[55] Glenn F. Knoll. *Radiation Detection and Measurement*. John Wiley & Sons, Inc., 2000.

[56] V.S. Kolhinen, S. Kopecky, T. Eronen, U. Hager, J. Hakala, J. Huikari, A. Jokinen, A. Nieminen, S. Rinta-Antila, J. Szerypo, and J. Äystö. JYFLTRAP: a cylindrical Penning trap for isobaric beam purification at IGISOL. *Nuclear Instruments and Methods in Physics Research A*, 528:776–787, 2004.

[57] Martin Kretzschmar. The Ramsey method in high-precision mass spectrometry with Penning traps: Theoretical foundations. *International Journal of Mass Spectrometry*, 264:122–145, 2007.

[58] I. A. Kuznetsov, A. P. Serebrov, I. V. Stepanenko, A. V. Alduschenkov, M. S. Lasakov, A. A. Kokin, Yu. A. Mostovoi, B. G. Yerozolimsky, and M. S. Dewey. Measurements of the antineutrino spin asymmetry in beta decay of the neutron and restrictions on the mass of a right-handed gauge boson. *Phys. Rev. Lett.*, 75(5):794–797, Jul 1995.

[59] T. D. Lee and C. N. Yang. Parity nonconservation and a two-component theory of the neutrino. *Physical Review*, 105(5):1671–1675, 1957.

[60] R. Van Lieshout, S. Monaro, G. B. Vingiani, and H. Morrinaga. The level structure of Mo^{92}. *Physics Letters*, 9:164–166, 1964.

[61] Harry J. Lipkin. Quantum theory of neutrino oscillations for pedestrians - simple answers to confusing questions. *Physics Letters B*, 642:366–371, 2006.

[62] K. Minamisono, K. Matsuta, T. Minamisono, T. Yamaguchi, T. Sumikama, T. Nagatomo, M. Ogura, T. Iwakoshi, M. Fukuda, M. Mihara, K. Koshigiri, and M. Morita. New limit of the g-parity irregular weak nucleon current detected in β decays of spin aligned $12B$ and $12N$. *Phys. Rev. C*, 65(1):015501, Dec 2001.

[63] A. Nieminen, P. Campbell, J. Billowes, D. H. Forest, J. A. R. Griffith, J. Huikari, A. Jokinen, I. D. Moore, R. Moore, G. Tungate, and J. Äystö. On-line ion cooling and bunching for collinear laser spectroscopy. *Phys. Rev. Lett.*, 88(9):094801, Feb 2002.

[64] E. W. Otten, J. Bonn, and Ch. Weinheimer. The Q-value of tritium β-decay and the neutrino mass. *International Journal of Mass Spectrometry*, 251:173–178, 2006.

[65] D. B Pinegar, S. L. Zafonte, and R. S. Van Dyck, Jr. The UW-PTMS: Recent measurements and technological progress. *Hyperfine Interactions*, 174:47–53, 2007.

[66] S. Profumo, M. J. Ramsey-Musolf, and S. Tulin. Supersymmetric contributions to weak decay correlation coefficients. *Physical Review D*, 75:075017, 2007.

[67] *et al* R. W. Pattie Jr. First measurement of the neutron β-asymmetry with ultracold neutrons.

[68] Jr. Raymond Davis, Don S. Harmer, and Kenneth C. Hoffman. Search for neutrinos from the sun. *Physical Review Letters*, 20.

[69] J. Reich, H. Abele, M. Astruc Hoffmann, S. Bae[ss]ler, P. v. Bulow, D. Dubbers, V. Nesvizhevsky, U. Peschke, and O. Zimmer. A measurement of the beta asymmetry in neutron decay with PERKEO II. *Nuclear Instruments and Methods in Physics Research Section A*, 440:535–538, 2000.

[70] Frederick Reines and Clyde L. Cowan. The neutrino. *Nature*, 178:446, 1956.

[71] V. A. Rodin, Amand Faessler, F. Šimkovic, and Petr Vogel. Uncertainty in the $0\nu\beta\beta$ decay nuclear matrix elements. *Phys. Rev. C*, 68(4):044302, Oct 2003.

[72] J. J. Sakurai. *Modern Quantum Mechanics*. Addison-Wesley Publishing Company, 1994.

[73] J. Sempau, E. Acosta, J. Baró, J.M. Fernández-Varea, and F. Salvat. An algorithm for Monte Carlo simulation of coupled electron-photon transport. *Nuclear Instruments and Methods in Physics Research B*, 132:377–390, 1997.

[74] H. Shiomi. Second class current in QCD sum rules. *Nuclear Physics A*, 603:281–302, 1996.

[75] M. Shumann, M. Kreuz, M. Deissenroth, F. Glück, J. Krempel, B. Märisch, D. Mund, A. Petoukhov, T. Soldner, and H. Abele. Measurement of the proton asymmetry parameter in neutron beta decay. *Physical Review Letters*, 100:151801, 2008.

[76] F. Šimkovic, P. Domin, and S. V. Semenov. The single state dominance hypothesis and the two-neutrino double beta decay of ^{100}Mo. *Journal of Physics G*, 27:2233–2240, 2001.

[77] Balraj Singh. Nuclear data sheets for $A = 100$. 2008.

[78] S. K. L. Sjue. Polarized neutron β-decay: the proton asymmetry and recoil-order currents. *Physical Review C*, 72:045501, 2005.

[79] A. A. Sonzogni. Nuclear data sheets for $A = 134$. 2004.

[80] E. C. G. Sudarshan and R. E. Marshak. Chirality invariance and the universal Fermi interaction. *Physical Review*, 109(5):1860=1862, 1958.

[81] J. Suhonen and O. Civitarese. Quasiparticle random phase approximation analysis of the double beta decay of ^{100}Mo to the ground state and excited states of ^{100}Ru. *Physical Review C*, 49:3055–3060, 1994.

[82] J. Suhonen and O. Civitarese. Weak-interaction and nuclear-structure aspects of nuclear double beta decay. *Physics Reports*, 300:123–214, 1998.

[83] Steven Weinberg. Charge symmetry of weak interactions. *Phys. Rev.*, 112(4):1375–1379, Nov 1958.

[84] F. E. Wietfeldt, B. M. Fisher, C. Trull, G. L. Jones, B. Collet, L. Goldin, B. G. Yerozolimsky, R. Wilson, S. Balashov, Yu. Mostovoy, A. Komives, M. Leuschner, J. Byrne, F. B. Bateman, M. S. Dewey, J. S. Nico, and A. K. Thompson. A method for an improved measurement of the electron-antineutrino correlation in free neutron beta decay. *Nuclear Instruments and Methods in Physics Research Section A*, 545.

[85] W. S. Wilburn, J. D. Bowman, G. S. Mitchell, J. M. O'Donnell, S. I. Penttila, P.-N. Seo, J. R. Calarco, F. W. Hersmann, T. E. Chupp, T. V. Cianciolo, K. P. Rykaczewski, G. R. Young, R. T. De Souza, W. M. Snow, D. Desai, G. L. Greene, R. K. Grzywacz, E. Friez, D. Pocanic, T. R. Gentile, V. Gudkov, and G. L. Jones. Measurement of neutron decay parameters-the abBA experiment. *Journal of Research of the National Institute of Standards and Technology*, 110:389–393, 2005.

[86] C. S. Wu, E. Ambler, R. W. Hayward, D. D. Hoppes, and R. P. Hudson. Experimental test of parity conservation in beta decay. *Physical Review*, 105(4):1413–1415, Feb 1957.

[87] O. Zimmer, J. Byrne, M. G. D. van der Grinten, W. Heil, and F. Glück. 'aspect' - a new spectrometer for the measurement of the angular correlation coefficient a in neutron beta decay. *Nuclear Instruments and Methods in Physics Research Section A*.

Appendix A
PERTURBATION THEORY

For the sake of both clarity and an avid interest in the subject itself, the following is a presentation of perturbation theory and some of its particularly relevant results. This first two sections are essentially modified from Sakurai [72]; the remainder takes an approach motivated by and relevant to beta and double-beta decay.

A.1 Schrödinger Equation for Time-Dependent Perturbations

Consider a Hamiltonian H_0 with a complete set of eigenstates $|i\rangle$ such that $H_0|i\rangle = E_i|i\rangle$. Any state $|\alpha\rangle$ may be written as a linear combination of the eigenstates, $|\alpha\rangle = \sum_i c_i|i\rangle$. The aim is to study the effect of a perturbation V on the Hamiltonian H_0, so the true Hamiltonian is

$$H = H_0 + V, \tag{A.1}$$

where V is small relative to H_0. The first step is to remove the known time dependence due to the unperturbed Hamiltonian, which is achieved by multiplying the ket $|\alpha\rangle$ by the inverse of the time-evolution operator for the unperturbed Hamiltonian:

$$|\alpha\rangle_I = e^{iH_0t/\hbar}|\alpha\rangle. \tag{A.2}$$

The suffix I denotes the new basis and stands for interaction. Now consider a matrix element for an operator O, $\langle\alpha|O|\alpha\rangle$. To obtain the same matrix element using $|\alpha\rangle_I$ instead of $|\alpha\rangle$, it is necessary to transform the operator:

$$O_I = e^{iH_0t/\hbar}Oe^{-iH_0t/\hbar}. \tag{A.3}$$

The goal is now to rewrite the Schrödinger Equation in terms of $|\alpha\rangle_I$. To this end, apply $i\hbar\frac{\partial}{\partial t}$ to $|\alpha\rangle_I$ to get

$$i\hbar\frac{\partial}{\partial t}|\alpha\rangle_I = -H_0|\alpha\rangle_I + e^{iH_0t/\hbar}i\hbar\frac{\partial}{\partial t}|\alpha\rangle \tag{A.4}$$

$$= -H_0|\alpha\rangle_I + H_0|\alpha\rangle_I + e^{iH_0t/\hbar}|\alpha\rangle \tag{A.5}$$

$$= e^{iH_0t/\hbar}V\left(e^{-iH_0t/\hbar}e^{iH_0t/\hbar}\right)|\alpha\rangle. \tag{A.6}$$

Taking the derivative, applying the Schrödinger Equation to $|\alpha\rangle$, and multiplying by a suggestive form of 1, one obtains

$$i\hbar\frac{\partial}{\partial t} = V_I|\alpha\rangle_I, \tag{A.7}$$

in which the time dependence due to H_0 has been removed from the state vectors.

The goal is to study transitions between the H_0 eigenstates due to V. For a state $|\alpha\rangle = \sum_i c_i|i\rangle$, with time dependence $|\alpha\rangle(t) = \sum_i c_i e^{-iE_it/\hbar}|i\rangle$, the time dependence has been strategically removed in the interaction basis, $|\alpha\rangle_I(t) = \sum_i c_i|i\rangle$. Next we apply our modified Schrödinger Equation (Equation A.7) to this ket $|\alpha\rangle_I$ and operate from the left with the bra $\langle f|$, to find

$$i\hbar\dot{c}_f(t) = \sum_i \langle f|V|i\rangle e^{i(E_f-E_i)t/\hbar}c_i(t) \tag{A.8}$$

$$= \sum_i \mathcal{M}_{fi}e^{i\omega_{fi}t}c_i(t), \tag{A.9}$$

where we have defined $\mathcal{M}_{fi} = \langle f|V|i\rangle$ and $\omega_{fi} = (E_f - E_i)/\hbar$. Equation A.9 is exact, but for a Hamiltonian with an infinite number of states, it defines an infinite set of coupled differential equations. Approximation methods will be necessary.

A.2 Dyson Series

To facilitate approximations, it is useful to rewrite the Schrödinger Equation for the interaction basis in terms of a time-evolution operator. Define the operator $U_I(t)$ so that

$$|\alpha\rangle_I(t) = U_I(t)|\alpha\rangle_I(t=0), \tag{A.10}$$

which requires that $U_I(t = 0) = 1$. Now require the time-dependent state vector $U_I(t)|\alpha\rangle_I$ to satisfy Equation A.7. $|\alpha\rangle_I(t = 0)$ is a constant, so $U_I(t)$ must satisfy

$$i\hbar\frac{\partial}{\partial t}U_I(t) = V_I(t)U_I(t). \tag{A.11}$$

Integrating to time T, one finds

$$i\hbar\left(U_I(T) - U_I(0)\right) = \int_0^T dt V_I(t)U_I(t), \tag{A.12}$$

on which we impose the initial condition $U_I(0) = 1$ to find

$$U_I(T) = 1 + \frac{1}{i\hbar}\int_0^T dt V_I(t)U_I(t). \tag{A.13}$$

Now we solve for $U_I(T)$ recursively to obtain the Dyson Series:

$$U_I(T) = 1 + \frac{1}{i\hbar}\int_0^T dt V_I(t) + \frac{1}{(i\hbar)^2}\int_0^T dt\int_0^t dt' V_I(t)V_I(t') + ... \tag{A.14}$$

This series has an infinite number of terms. The second and third terms are sufficient for our purposes. Although the derivation used the Schrödinger Equation instead of fields and a Lagrangian density, the same series can give us the correct results for the Weak Interaction processes we wish to study.

A.3 Fermi's Golden Rule

The second term on the right-hand side of Equation A.14 describes processes involving a single interaction. Consider a system initially in a state $|i\rangle$. To first order in the perturbation V, assuming that the perturbation is time-independent, the probability of a transition to state $|f\rangle$ is

$$\begin{aligned} P_{i\to f}(t) &= |\langle f|U_I(t)|i\rangle|^2 && \text{(A.15)}\\ &= \left|\frac{1}{i\hbar}\int_0^t dt'\langle f|V_I|i\rangle\right|^2 && \text{(A.16)}\\ &= \left|\frac{\mathcal{M}_{fi}}{i\hbar}\int_0^t dt' e^{i\omega_{fi}t}\right|^2 && \text{(A.17)}\\ &= \frac{|\mathcal{M}_{fi}|^2}{(\hbar\omega_{fi})^2}\left(2 - 2\cos(\omega_{fi}t)\right), && \text{(A.18)} \end{aligned}$$

where the notation introduced for Equation A.9 has been used again. This is the total probability of a transition to a state $|f\rangle$. Note that for short times, the probability is actually nonzero even for states that violate conservation of energy. This is why processes like beta decay, in which there is an intermediate virtual W boson that violates conservation of energy, are possible.

For most purposes, the quantity of interest is the transition rate. For instance, measuring the lifetime of a radioactive isotope, one measures the decay rate as a function of time for a large sample. To find the average transition rate from the transition probability, divide by t and take the limit as t becomes very large:

$$\Gamma_{i\to f} = \lim_{t\to\infty} \frac{|\mathcal{M}_{fi}|^2}{(\hbar\omega_{fi})^2} \frac{(2-2\cos(\omega_{fi}t))}{t}. \tag{A.19}$$

Clearly, the transition rate vanishes unless $\omega_{fi} \to 0$. The function diverges at $\omega_{fi} = 0$. This expression for the decay rate at long times behaves like an energy-conserving δ function.

To extract the normalization of the δ function, one can integrate the function by use of contour integrals in the complex plane. For convenience, we momentarily discard the subscripts to write ω in place of ω_{fi}. The integral of interest is

$$\int_{-\infty}^{\infty} d\omega \frac{(2-2\cos(\omega t))}{\omega^2}. \tag{A.20}$$

Consider the two terms in the numerator of the integral separately. The two integrals are

$$\int_{-\infty}^{\infty} d\omega \frac{2}{\omega^2} \tag{A.21}$$

and

$$\int_{-\infty}^{\infty} d\omega \frac{-2\cos(\omega t)}{\omega^2}. \tag{A.22}$$

Both integrals can be solved by allowing ω to take complex values and considering the two contour integrals in Figure A.1. By the Residue Theorem, the integral A.21 vanishes because it has no residue. The second integral can be solved as the real part of the integral of an exponential

$$\int_{-\infty}^{\infty} d\omega \frac{-2\cos(\omega t)}{\omega^2} = \mathrm{Re}\left(\int_{-\infty}^{\infty} d\omega \frac{-2e^{i\omega t}}{\omega^2}\right). \tag{A.23}$$

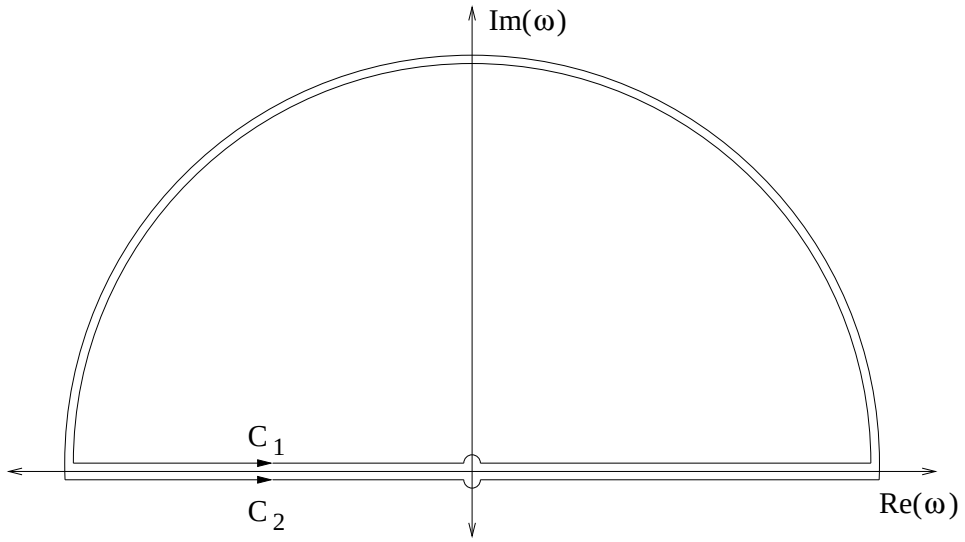

Figure A.1: Contours to integrate the δ function in Fermi's Golden Rule. In the limit where the semicircular radius $R \to \infty$, its contribution to both integrals vanishes. The integral from $-\infty$ to ∞ along the real axis is equal to the average of the integral over each of the two contours. Both contours follow the real axis except at the origin, where there is a pole. The semicircles about the pole at $\omega = 0$ are considered in the limit where the radius $r \to 0$. The contours have been drawn away from the real axis for clarity.

The desired integral is equal to the average of the two contour integrals in Figure A.1.

$$\int_{-\infty}^{\infty} d\omega \frac{-2e^{i\omega t}}{\omega^2} = \frac{1}{2}\left(\oint_{C_1} d\omega \frac{-2e^{i\omega t}}{\omega^2} + \oint_{C_2} d\omega \frac{-2e^{i\omega t}}{\omega^2}\right) \tag{A.24}$$

The integral over C_1 vanishes because it has no residue. All that is necessary to solve the integral over C_2 is to determine the residue at $\omega = 0$.

To find the residue at $\omega = 0$, expand the exponential:

$$-2\frac{e^{i\omega t}}{\omega^2} = -2\left(\frac{1 + i\omega t - \omega^2 t^2/2 - \cdots}{\omega^2}\right) \tag{A.25}$$

The coefficient for the term that goes like $\frac{1}{\omega}$ is $-2it$; this is the residue at $\omega = 0$. Using the Residue Theorem, the result is

$$\int_{-\infty}^{\infty} d\omega \frac{-2\cos(\omega t)}{\omega^2} = \frac{1}{2} Re\left(2\pi i[-2it]\right) = 2\pi t. \tag{A.26}$$

Now we revisit Equation A.19 with this result to obtain

$$\Gamma_{i\to f} = 2\pi \frac{|\mathcal{M}_{fi}|^2}{\hbar^2}\delta(\omega_{fi}). \tag{A.27}$$

This is the average rate of transition from a state $|i\rangle$ to a state $|f\rangle$ due to the perturbing interaction, V.

For beta decay, we will consider final states that involve a continuum of states for free particles: for example, a β^- shares energy available from a decay's Q value with a $\bar{\nu}_e$; both are free particles that can be emitted in any direction, with continuous energy distributions. For this reason, to get an actual decay rate, one must sum Equation A.27 over the number of final states available. Since the final states are continuum states, the integral performed over ω_{fi} becomes an integral over E_f, while changing the units within the δ function gives a factor of $\hbar$. Integrating over the continuum states by applying $\int dE_f \frac{dN}{dE_f}$ to get the total decay probability, one finds the standard form of Fermi's Golden Rule:

$$\Gamma_{i\to f} = \frac{2\pi}{\hbar}\int dE_f \frac{dN}{E_f}|\mathcal{M}_{fi}|^2\delta(E_f - E_i) \tag{A.28}$$

The factor $\int dE_f \frac{dN}{dE_f}$ gives the number of final states available. The number of final states available is determined by the total phase space available, which is given by the dimensionless integral

$$N = \int dE_f \frac{dN}{dE_f} = \int \prod_k \frac{d^3\vec{p}_k d^3\vec{x}_k}{(2\pi\hbar)^3}, \tag{A.29}$$

where the product is over the number of particles in the final state, k. In general, the volume integrals are performed to evaluate the interaction matrix elements. Barring non-local interactions, the volume integrals will yield a momentum-conserving delta function, $\delta^3(\sum_i \vec{p}_i - \sum_k \vec{p}_k)$. The remaining integral,

$$f \equiv \int \prod_k \frac{d^3\vec{p}_k}{(2\pi)^3}\delta^3(\sum_i \vec{p}_i - \sum_k \vec{p}_k)\delta(\sum_i E_i - \sum_k E_k), \tag{A.30}$$

is commonly denoted by f in the literature and referred to as the phase-space integral. The results of this integral for several beta-decay processes are presented in Appendix B.

A.4 Second-Order Transitions

Now we examine the third term on the right-hand side of Equation A.14. The results apply to both $2\nu\beta\beta$ and $0\nu\beta\beta$ decay. These are both processes that feature two interactions. Consider the term

$$\frac{1}{(i\hbar)^2}\int_0^T dt \int_0^t dt' V_I(t)V_I(t'), \tag{A.31}$$

which gives the transition amplitude

$$M_{i\to f}(T) = \langle f|\frac{1}{(i\hbar)^2}\int_0^T dt \int_0^t dt' V_I(t)V_I(t')|i\rangle. \tag{A.32}$$

Insert a complete set of states, $\sum_m |m\rangle\langle m|$, between $V_I(t)$ and $V_I(t')$ to find

$$M_{i\to f}(T) = \sum_m \frac{1}{(i\hbar)^2}\int_0^T dt \int_0^t dt' \mathcal{M}_{fm} e^{i\omega_{fm}t}\mathcal{M}_{mi}e^{i\omega_{mi}t'}. \tag{A.33}$$

The result from the integral over dt' is

$$M_{i\to f}(T) = \sum_m \frac{1}{(i\hbar)^2}\int_0^T dt \frac{\mathcal{M}_{fm}\mathcal{M}_{mi}}{i\omega_{mi}}\left(e^{i\omega_{fi}t} - e^{i\omega_{fm}t}\right). \tag{A.34}$$

For systems that exhibit double-beta decay, energy levels of the intermediate nucleus are the states m over which one sums. In cases of experimental interest, the intermediate nucleus has a higher ground-state energy than either the parent or daughter nucleus. The modulus-squared of the previous expression includes terms proportional to $e^{i\omega_{fm}}$ and $e^{i\omega_{mi}}$, but because there are no states in the intermediate nucleus that satisfy conservation of energy, these terms will vanish. The same integrals performed to obtain Equation A.28 apply to this expression and give the same result, with a modification to the matrix element

$$\mathcal{M}_{fi} \to \sum_m \frac{\mathcal{M}_{fm}\mathcal{M}_{mi}}{\hbar\omega_{mi}}. \tag{A.35}$$

In the case of $2\nu\beta\beta$ decay of ^{100}Mo to the ground state of ^{100}Ru, for example, the matrix element can be expressed as

$$\mathcal{M}_{fi} = \sum_m \frac{\langle {}^{100}\mathrm{Ru}|V|{}^{100}\mathrm{Tc}^m\rangle\langle {}^{100}\mathrm{Tc}^m|V|{}^{100}\mathrm{Mo}\rangle}{M_{\mathrm{Mo}} - E_{\beta 1} - E_{\bar{\nu}_e 1} - E_{\mathrm{Tc}^m}}, \tag{A.36}$$

where the sum is over the ground and excited states of ^{100}Tc and $E_{\beta 1}$ and $E_{\bar{\nu}_e 1}$ are the energies of the electron and neutrino emitted in the first virtual transition. Making the intuitive assumption that $E_{\beta 1}$ and $E_{\bar{\nu}_e 1}$ should have the same energy as $E_{\beta 2}$ and $E_{\bar{\nu}_e 2}$ on average, one can substitute

$$E_{\beta 1} + E_{\bar{\nu}_e 1} = \frac{Q_{\beta\beta}}{2} = \frac{(Q_\beta - Q_{EC})}{2} \tag{A.37}$$

in the denominator to obtain the contribution to the total decay matrix element from the ^{100}Tc ground state (or any other state, for that matter):

$$|\mathcal{M}_{fi}(gs)| \approx \frac{|\langle ^{100}\mathrm{Ru}|V|^{100}\mathrm{Tc}(gs)\rangle||\langle ^{100}\mathrm{Tc}(gs)|V|^{100}\mathrm{Mo}\rangle|}{(Q_{EC} + Q_\beta)/2} \tag{A.38}$$

The approximation of a constant denominator using an effective Q-value for the average excitation energy in the intermediate nucleus has been used extensively in the literature. This approximation is especially suited for $0\nu\beta\beta$ decay, because the denominator gets integrated with an additional factor of the virtual neutrino's energy E_ν, which is large compared to the Q values involved (See Section 1.7).

Appendix B

BETA-DECAY KINEMATICS

It is worthwhile to consider phase-space integrals for the weak processes and approximations that are referenced throughout this document. Here we consider only the functional forms of the integrals for clarity, leaving dimensions, factors of 2, and factors of π for the references that will inevitably be necessary for precise calculations.

B.1 Electron Capture

The simplest of these integrals for β-decay processes is the integral corresponding to electron capture. This is the process in which a nucleus captures one of its atomic electrons and emits a neutrino,

$$A(N,Z) + e^- \rightarrow A(N+1, Z-1) + \nu_e. \tag{B.1}$$

The same integral applies to neutrino capture. Writing f in terms of the final-state neutrino and daughter nucleus in the rest frame of the parent nucleus,

$$f \propto \int d^3\vec{p}_f d^3\vec{p}_\nu \delta^3(\vec{p}_\nu - \vec{p}_f)\delta(E_f + E_\nu - M). \tag{B.2}$$

Performing the integral, one finds

$$f \propto \frac{p_\nu^2}{\frac{p_\nu}{E_\nu} + \frac{p_\nu}{M_f}}, \tag{B.3}$$

which is now constrained such that $p_\nu^2 + m_\nu^2 + \dfrac{p_\nu^2}{2M_f} = \Delta M$. Treating the neutrino mass as negligible compared to the Q-value and the Q-value as negligible compared mass of the daughter nucleus, this simplifies to

$$f \propto p_\nu^2, \tag{B.4}$$

where $p_\nu = E_\nu = Q$. Just to put the approximations in perspective, for the EC decay of ^{100}Tc, the energy available is $Q_{\rm EC} = 168$ keV. The recoil correction is $\mathcal{O}(10^{-6})$.

Assuming a neutrino mass $m_\nu = 1$ eV, the correction for the for the neutrino mass is $< 10^{-5}$.

Accurate calculations must take into account the captured electron's wave function and binding energy, which can be significant compared to the low Q values at which electron captures take place. Exchange effects, due to antisymmetrization of all the final-state electron wave functions, are also relevant.

B.2 Beta Decay

In beta decay, an initial nucleus decays into a daughter nucleus with a different charge, emitting either a β^- and a $\bar{\nu}_e$

$$A(N, Z) \rightarrow A(N-1, Z+1) + \beta^- + \bar{\nu}_e, \tag{B.5}$$

or a β^+ and a ν_e,

$$A(N, Z) \rightarrow A(N+1, Z-1) + \beta^+ + \nu_e. \tag{B.6}$$

In the rest frame of the parent nucleus, the phase space for the three final particles is given by

$$f \propto \int d^3\vec{p}_f d^3\vec{p}_e d^3\vec{p}_\nu \delta^3(\vec{p}_f + \vec{p}_e + \vec{p}_\nu)\delta(M - E_f - E_e - E_\nu), \tag{B.7}$$

in which M is the mass of the parent nucleus and m_f and E_f are the mass and energy of the daughter nucleus. Integrating over the daugher nucleus's momentum first and using the relation $d^3\vec{p} = p^2 dp d\Omega \propto pEdE$ for both the neutrino and the electron, one finds

$$f \propto \int dE_\nu dE_e p_e E_e E_\nu^2 \delta(M - \sqrt{M_f^2 + p_e^2 + p_\nu^2 + 2\vec{p}_e \cdot \vec{p}_\nu} - E_e - E_\nu), \tag{B.8}$$

in which m_ν / E_ν has been neglected. Integrating over dE_ν, the derivative of the δ function's argument gives a denominator of $1 + (E_\nu + p_e \cos(\theta_{e\nu}))/E_f$. Note that this denominator differs from 1 only by a very small quantity. For the moment, neglect the small term in the denominator. This gives an approximate result that is adequate qualitatively adequate for many beta-decay spectra:

$$\frac{d\Gamma}{dE_e} = E_e p_e (E_0 - E_e)^2. \tag{B.9}$$

The integral over the electron energy gives a decay rate that is proportional to Q^5, which is known as Sargent's Rule. The next most important effect to calculate an accurate beta-decay spectrum takes into account the charge of the nucleus with the Fermi function, $F(Z, E_e)$.

B.3 Beta Decay with Recoil Corrections

Extract a factor of $\frac{1}{E_f}$ from the matrix element and distribute it through the denominator before performing the integral in Equation B.8, then use the identity $E_f + E_\nu = M - E_e$ to obtain

$$f \propto \int dE_e d\Omega_e d\Omega_\nu \frac{E_e p_e E_\nu^2}{M - E_e + p_e \cos(\theta_{e\nu})}. \tag{B.10}$$

It is useful to define some variables. Conservation of energy and momentum give

$$|\vec{p}_e + \vec{p}_\nu| = \sqrt{E_f - m_f^2} = \sqrt{(M - E_e - E_\nu)^2 - M_f^2}, \tag{B.11}$$

which can be solved for the neutrino's energy:

$$E_\nu = \frac{M^2 + m_e^2 - M_f^2 - 2ME_e}{2(M - E_e + |\vec{p}_e| \cos(\theta_{e\nu}))}. \tag{B.12}$$

Defining a small, dimensionless parameter that characterizes the decay, $R \equiv max(E_e/M)$, set $E_\nu = 0$ in the previous equation and it follows that

$$R = \frac{M^2 + m_e^2 - M_f^2}{2M^2}. \tag{B.13}$$

Then the differential probability as a function of electron energy and the electron-neutrino angle becomes

$$f \propto (MR)^4 \int dx d(\cos(\theta_{e\nu})) \frac{\beta x^2 (1-x)^2}{1 - Rx\,(1 - \beta \cos(\theta_{e\nu}))}, \tag{B.14}$$

in which x is the electron's energy divided by its maximum energy, RM_n. The kinematical corrections from the denominator have effects on the same order as non-Standard Model couplings, so they are important for precision measurements that aim to probe for new physics. See Chapter 6 for more on these recoil-order effects.

B.4 Double-Beta Decay

The $0\nu\beta\beta$ decay mode has larger phase space than $2\nu\beta\beta$ decay. To make a simple approximation, ignore the portion of the phase space for the two neutrinos in $2\nu\beta\beta$ decay; the missing dimension of $[E]^6$ in the $0\nu\beta\beta$ decay phase space is contained in the neutrino potential and matrix element of Equations 1.56 and 1.57. The phase space contribution from the two electrons in either case is proportional to

$$\left(\frac{Q}{m_e}\right)^5, \tag{B.15}$$

similar to Sargent's Rule for single-beta decay. The total energy Q must be divided between all of the final-state particles. Only two electrons are emitted from $0\nu\beta\beta$ decay; thus the phase space is roughly proportional to

$$\left(\frac{Q}{2m_e}\right)^5. \tag{B.16}$$

But there are four particles from $2\nu\beta\beta$ decay; the estimate becomes

$$\left(\frac{Q}{4m_e}\right)^5. \tag{B.17}$$

Therefore the phase space is ≈ 30 times larger for $0\nu\beta\beta$ decay. However, this is insignificant compared to the suppression due to the $\langle m_\nu \rangle / \langle E_\nu \rangle$ factor in the $0\nu\beta\beta$ matrix element, which was discussed in Section 1.7.

Appendix C

DIRAC EQUATION

The Dirac equation is a first-order equation that describes spin-1/2 particles. Assuming that such an equation exists, the wave functions must satisfy

$$E\psi = \vec{\alpha} \cdot \vec{p}\psi + \beta m\psi. \tag{C.1}$$

Squaring both sides of the equation yields

$$E^2\psi = \sum_{i \neq j} \{\alpha_i, \alpha_j\} p_i p_j \psi + \beta^2 m^2 \psi + \sum_i \{\alpha_i, \beta\} p_i m\psi + \sum_i \alpha_i^2 p_i^2 \psi, \tag{C.2}$$

in which the anticommutators are given by $\{\alpha_i, \alpha_j\} = \alpha_i\alpha_j + \alpha_j\alpha_i$. This equation will satisfy the requirement of Lorentz invariance, $E^2 - p^2 = m^2$, only if the following relationships are satisfied:

$$\{\alpha_i, \alpha_j\} = \delta_{ij}, \tag{C.3}$$

$$\{\alpha_i, \beta\} = 0, \tag{C.4}$$

$$\beta^2 = 1. \tag{C.5}$$

To make the Lorentz invariance manifest in the equation, multiply Equation C.1 by β and rearrange to obtain

$$\beta E\psi - \beta\vec{\alpha} \cdot \vec{p}\psi - m\psi = 0. \tag{C.6}$$

In the Chiral representation, also referred to as the Weyl basis, the matrices take the explicit forms

$$\beta = \begin{pmatrix} 0 & 1 \\ 1 & 0 \end{pmatrix} \tag{C.7}$$

and

$$\alpha_i = \begin{pmatrix} -\sigma_i & 0 \\ 0 & \sigma_i \end{pmatrix}, \tag{C.8}$$

where σ_i refers to the three 2×2 Pauli matrices and the 1s in β refer to the 2×2 identity matrix. These four 4×4 matrices define a four-vector,

$$(\gamma_0, \vec{\gamma}) = (\beta, \beta\vec{\alpha}), \tag{C.9}$$

such that the manifestly Lorentz-invariant form of the Dirac equation is

$$\gamma^\mu p_\mu \psi = m\psi, \tag{C.10}$$

and p^μ is the four-momentum $(E, \vec{p})$. The Dirac equation satisfies Lorentz invariance because of the anticommutation relation between the γ matrices:

$$\{\gamma^\mu, \gamma^\nu\} = 2g^{\mu\nu} \tag{C.11}$$

In this representation, the metric tensor has negative spatial components $g^{ii} = -1$ and $g^{00} = +1$, descriptively known as the "mostly-minus metric." The gamma matrices are conveniently expressed as

$$\gamma^\mu = \begin{pmatrix} 0 & \sigma^\mu \\ \bar{\sigma}^\mu & 0 \end{pmatrix}, \tag{C.12}$$

if we define $\sigma^\mu = (1, \vec{\sigma})$ and $\bar{\sigma}^\mu = (1, -\vec{\sigma})$. The Feynman dagger notation is often convenient, $\not{p} \equiv p \cdot \gamma = \gamma^\mu p_\mu$. It gives the Dirac equation an especially compact form:

$$\not{p}\psi = m\psi. \tag{C.13}$$

This notation disguises a first order, linear differential equation in four dimensions in terms of complex four-by-four matrices to look as innocent as possible.

Now we seek solutions of the Dirac equation. A substitution of $\psi = e^{ip\cdot x}(u_-(p)\chi^T, u_+(p)\chi^T)^T$ into the Dirac equation written in terms of the four-vectors σ and $\bar{\sigma}$ defined after Equation C.12 yields

$$\begin{pmatrix} -m & p\cdot\sigma \\ p\cdot\bar{\sigma} & -m \end{pmatrix} \begin{pmatrix} u_-(p)\chi \\ u_+(p)\chi \end{pmatrix} = 0. \tag{C.14}$$

The identity $(p\cdot\sigma)(p\cdot\bar{\sigma}) = p^2$ makes it easy to find two solutions based on this substitution:

$$\psi = \begin{pmatrix} \sqrt{p\cdot\sigma}\chi \\ \sqrt{p\cdot\bar{\sigma}}\chi \end{pmatrix} \tag{C.15}$$

There are two solutions, one for each component of the spinor χ. These wave functions describe particles. Another set of solutions can be obtained in the same way but with the the exponent changed to $Et - \vec{p} \cdot \vec{x} \rightarrow -Et - \vec{p} \cdot \vec{x}$ and $u_{\pm} \rightarrow v_{\pm}$:

$$\begin{pmatrix} -m & -p \cdot \bar{\sigma} \\ -p \cdot \sigma & -m \end{pmatrix} \begin{pmatrix} v_{-}(p)\chi \\ v_{+}(p)\chi \end{pmatrix} = 0. \tag{C.16}$$

The "negative energy" solutions follow in a similar fashion,

$$\psi = \begin{pmatrix} \sqrt{p \cdot \bar{\sigma}}\chi \\ -\sqrt{p \cdot \sigma}\chi \end{pmatrix} \tag{C.17}$$

The negative energy in the exponent finds its interpretation in the form of antiparticles. For charged particles, these spinors correspond to particles with the opposite charge. The only uncharged fermions currently known are neutrinos. Because the neutrinos have no charge, it is not yet clear whether they are distinguishable from or identical to their antiparticles (or some subtle mixture of these two possibilities), as discussed in Section 1.7.

Consider the normalization of these wave functions. For both sets of wave functions (Equations C.15 and C.17), one finds

$$\psi^{\dagger}\psi = p \cdot \sigma \chi^{\dagger}\chi + p \cdot \bar{\sigma}\chi^{\dagger}\chi, \tag{C.18}$$

from which a sum over helicity states (χ^{+} and χ^{-}) yields $\psi^{\dagger}\psi = 2E$, which is the zeroth component of the momentum four-vector. To make a Lorentz-invariant quantity from this product of the wave functions, take the dot product of it with the four-vector $(\gamma_0, \vec{\gamma})$. The Lorentz-invariant product is

$$\bar{\psi}\psi \equiv \psi^{\dagger}\gamma_0\psi, \tag{C.19}$$

and the result of the sum over spins is $\pm 2m$, with the plus and minus signs corresponding to the positive and negative (particle and antiparticle) solutions.

Because of its importance in the weak interaction, we discuss the discrete symmetry of parity. $\bar{\psi}\psi$ is a scalar. $\bar{\psi}\gamma^{\mu}\psi$ is a vector, but substituting $\vec{p} \rightarrow -\vec{p}$ into ψ does not

give the required transformation property $\Pi : \bar{\psi}\vec{\gamma}\psi \Rightarrow -\bar{\psi}\vec{\gamma}\psi$. The correct transformation properties are exhibited by

$$\psi(\vec{p}) \rightarrow \gamma_0\psi(-\vec{p}). \tag{C.20}$$

For $\bar{\psi}$ this gives

$$\bar{\psi} = (\gamma_0\psi)^\dagger \rightarrow (\gamma_0\gamma_0\psi)^\dagger = \psi^\dagger \tag{C.21}$$

The spatial gamma matrices change sign:

$$\bar{\psi}\vec{\gamma}\psi \rightarrow \psi^\dagger\vec{\gamma}\gamma_0\psi = -\bar{\psi}\vec{\gamma}\psi. \tag{C.22}$$

But γ_0 does not change sign, because it commutes with itself. By this prescription, any operator O is given a parity transformation not only by substituting $\vec{p} \rightarrow -\vec{p}$, but also by performing the similarity transformation:

$$\Pi : O \Rightarrow \gamma_0 O \gamma_0^{-1} = \gamma_0 O \gamma_0. \tag{C.23}$$

The anticommutation relations between the gamma matrices ensure that this quantity transforms properly under parity. The matrix

$$\gamma_5 \equiv i\gamma_0\gamma_1\gamma_2\gamma_3 = \begin{pmatrix} -1 & 0 \\ 0 & 1 \end{pmatrix} \tag{C.24}$$

anticommutes with γ_0 and the components of $\vec{\gamma}$, which allows us to write the quantity that transforms like an axial vector,

$$\bar{\psi}\gamma^\mu\gamma_5\psi. \tag{C.25}$$

This is the bilinear poduct of the fields that has the same transformtion properties as $\bar{\psi}\gamma^\mu\psi$, plus an additional overall minus sign. This completes the list of ingredients essential to the weak interaction's $V - A$ current.

Appendix D

PION DECAY

The pion decay branching ratio for the production of muons versus electrons is simple to calculate. The matrix element for the decay comes from the current-current coupling,

$$\mathcal{L}_{\text{weak}} \propto h^{\mu} l_{\mu}, \tag{D.1}$$

in which l_{μ} represents the leptons. For the electron current,

$$l_{\mu} = \bar{e}\gamma_{\mu}(1-\gamma_5)\nu, \tag{D.2}$$

in which $\bar{e}$ is the field of the outgoing electron and ν is the field of the outgoing antineutrino. Only vector and axial vector currents result in a non-zero matrix element given the $V-A$ form of the lepton current. Since the pion has no spin, the only vector associated with the pion is its momentum, so we take the hadron current to be proportional to this vector

$$h^{\mu} \propto f_{\pi}(q^2)q^{\mu} \rightarrow f_{\pi}q^{\mu}, \tag{D.3}$$

in which q^{μ} is the pion's four-momentum and f_{π} accounts for the strong interaction.

First, we present a calculation that emphasizes the role of the chiral form of the weak interaction. To do this, write l^{μ} in a form that emphasizes the chiral projections that participate in the weak interaction:

$$l_{\mu} = \bar{e}\frac{1+\gamma_5}{2}\gamma_{\mu}\frac{1-\gamma_5}{2}\nu \tag{D.4}$$

The matrix element is proportional to the invariant product of the hadron current and the lepton current. The rest frame of the pion makes the calculation simple. Then $h^{\mu} \propto (m_{\pi}, 0)$, which allows one to substitute $\gamma_{\mu} \rightarrow \gamma_0$ in l_{μ} with impunity.

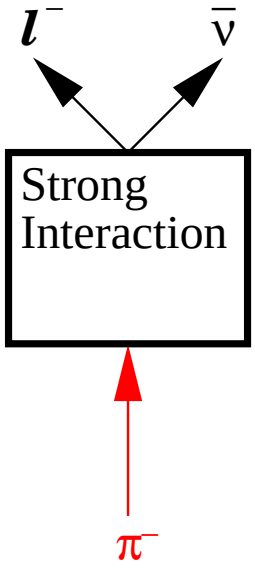

Figure D.1: Pion decay diagram for decay into a lepton-antineutrino pair. The strong-interaction's effects are represented by f_π in the calculation.

Now write the matrix element explicity in terms of the matrices and wave functions:

$$\mathcal{M} \propto f_\pi m_\pi \times \left(\begin{array}{c} \sqrt{E_e + \vec{p}_e \cdot \vec{\sigma}_e}\chi_e \\ \sqrt{E_e - \vec{p}_e \cdot \vec{\sigma}_e}\chi_e \end{array} \right)^T \left(\begin{array}{cc} 0 & 0 \\ 0 & 1 \end{array} \right) \left(\begin{array}{cc} 0 & 1 \\ 1 & 0 \end{array} \right) \left(\begin{array}{cc} 1 & 0 \\ 0 & 0 \end{array} \right) \left(\begin{array}{c} \sqrt{E_\nu + \vec{p}_\nu \cdot \vec{\sigma}_\nu}\chi_\nu \\ -\sqrt{E_\nu - \vec{p}_\nu \cdot \vec{\sigma}_\nu}\chi_\nu \end{array} \right) \tag{D.5}$$

The wave functions for the electron and neutrino were taken from Equations C.15 and C.17. Note that the chiral projection operators pick only the $\sqrt{E_e - \vec{p}_e \cdot \vec{\sigma}_e}\chi_e$ and $\sqrt{E_\nu + \vec{p}_\nu \cdot \vec{\sigma}_\nu}\chi_\nu$ components of the wave functions. Because of this, the matrix element is proportional to their product:

$$\mathcal{M} \propto \sqrt{E_e - \vec{p}_e \cdot \vec{\sigma}_e}\sqrt{E_\nu + \vec{p}_\nu \cdot \vec{\sigma}_\nu}\chi_e^T\chi_\nu. \tag{D.6}$$

To perform the sum over spins, it is convenient to write the spinors in the helicity basis. In this basis, χ_+ represents spin in the same direction as the particle's momentum and χ_- represents spin opposed to the particle's momentum. The sum over these two states in the helicity basis gives

$$\mathcal{M} \propto \sqrt{E_e - p_e}\sqrt{E_\nu + p_\nu} + \sqrt{E_e + p_e}\sqrt{E_\nu - p_\nu}, \tag{D.7}$$

in which the first term is from χ_+ and the second term is from χ_-. If the electron and neutrino were both massless, the matrix element would be zero. Because $m_e \gg m_\nu$, the second term is negligible. Conservation of momentum gives $p_e = p_\nu = E_\nu$. It is only the mass of the electron, which mixes positive helicity into the left-handed chiral projection in proportion to the electron's mass, that results in a non-zero matrix element. The result is

$$\mathcal{M} \propto \sqrt{E_e - E_\nu}\sqrt{2E_\nu}. \tag{D.8}$$

The kinematics of the decay give $E_e - E_\nu = m_e^2/m_\pi$, so that $|\mathcal{M}|^2 \propto m_e^2$. This kinematical result is included after another calculation. The point here was to show explicitly, in terms of the effect of the chiral projection operators on the wave functions, that the weak interaction suppresses this decay, which only occurs in proportion to the electron mass.

More complicated calculations (for example, see Appendix G) require more sophisticated techniques than explicitly writing the matrices and spinors. To this end, we now calculate the same matrix element using trace identities. First, use conservation of momentum ($p_\pi^\mu = p_e^\mu + p_\nu^\mu$) to write

$$\begin{aligned} \mathcal{M} &\sim f_\pi (p_e^\mu + p_\nu^\mu)\bar{e}\gamma_\mu(1-\gamma_5)\nu \\ &= f_\pi \left(\bar{e}\not{p}_e(1-\gamma_5)\nu + \bar{e}(1+\gamma_5)\not{p}_\nu \nu \right). \end{aligned} \tag{D.9}$$

The Dirac equation tells us that

$$\bar{e}\not{p} = -m_e\bar{e}, \tag{D.10}$$

and

$$\not{p}\nu = 0, \tag{D.11}$$

neglecting the neutrino mass. The decay rate is proportional to the modulus-squared of the matrix element,

$$\begin{aligned} |\mathcal{M}|^2 &\sim |f_\pi|^2 m_e^2 \nu^\dagger (1-\gamma_5)^\dagger \gamma_0^\dagger e\bar{e}(1-\gamma_5)\nu \\ &= |f_\pi|^2 m_e^2 \bar{\nu}(1+\gamma_5)e\bar{e}(1-\gamma_5)\nu. \end{aligned} \tag{D.12}$$

This expression simplifies immensely if we sum over spins,

$$\begin{aligned} |\mathcal{M}|^2 &\sim |f_\pi|^2 m_e^2 \mathbf{Tr}\left[\not{p}_\nu(1+\gamma_5)(\not{p}_e + m_e)(1-\gamma_5)\right] \\ &= 8|f_\pi|^2 m_e^2 (p_e \cdot p_\nu) \\ &= 8|f_\pi|^2 m_e^2 (E_e E_\nu - \vec{p}_e \cdot \vec{p}_\nu) \\ &= 8|f_\pi|^2 m_e^2 E_e E_\nu (1+\beta_e). \end{aligned} \tag{D.13}$$

The last line uses β_e for the electron's relativistic velocity, p_e/E_e, and also the fact that the electron and neutrino must be emitted in opposite directions in the pion's rest frame.

Now consider the kinematics. Neglecting the neutrino mass again, in the pion's rest frame conservation of momentum yields

$$|\vec{p}_e| = |\vec{p}_\nu| = E_\nu, \tag{D.14}$$

from which we use conservation of energy to write

$$m_\pi = E_e + E_\nu = \sqrt{m_e^2 + E_\nu^2} + E_\nu. \tag{D.15}$$

A bit of algebra reveals the remaining ingredients:

$$E_\nu = \frac{m_\pi^2 - m_e^2}{2m_\pi}, \tag{D.16}$$

$$\text{and} \quad E_e = \frac{m_\pi^2 + m_e^2}{2m_\pi} \tag{D.17}$$

Putting it all together into a decay rate,

$$\Gamma(\pi^- \to e\bar{\nu}_e) \propto \int d^3p_e d^3p_\nu \delta^4(p_\pi - p_e - p_\nu) \frac{|\mathcal{M}|^2}{E_e E_\nu}. \tag{D.18}$$

Integrate over d^3p_e in the pion's rest frame to find

$$\Gamma \propto \int dE_\nu E_\nu^2 \delta(m_\pi - E_\nu - \sqrt{m_e^2 + E_\nu^2}) \frac{|\mathcal{M}|^2}{E_e E_\nu}, \tag{D.19}$$

from which the delta function gives

$$\Gamma \propto \frac{E_\nu^2}{1 + \frac{E_\nu}{E_e}} \frac{|\mathcal{M}|^2}{E_e E_\nu}. \tag{D.20}$$

The denominator is just $1 + \beta_e$. Including the matrix element from Equation D.13, the final result is

$$\Gamma \propto m_e^2 \frac{(m_\pi^2 - m_e^2)^2}{m_\pi^2}. \tag{D.21}$$

For the decay rate to the muon, only the labels change: $m_e \to m_\mu$. Thus the branching ratio is:

$$\frac{\Gamma(\pi^- \to e^- + \bar{\nu}_e)}{\Gamma(\pi^- \to \mu^- + \bar{\nu}_\mu)} = \frac{m_e^2}{m_\mu^2} \frac{(1 - m_e^2/m_\pi^2)}{(1 - m_\mu^2/m_\pi^2)} = 1.30 \times 10^{-4} \tag{D.22}$$

The decay to the muon dominates because the larger muon mass mixes more positive helicity into the left-handed chiral projection of the weak interaction.

Appendix E

DESIGN DRAWINGS

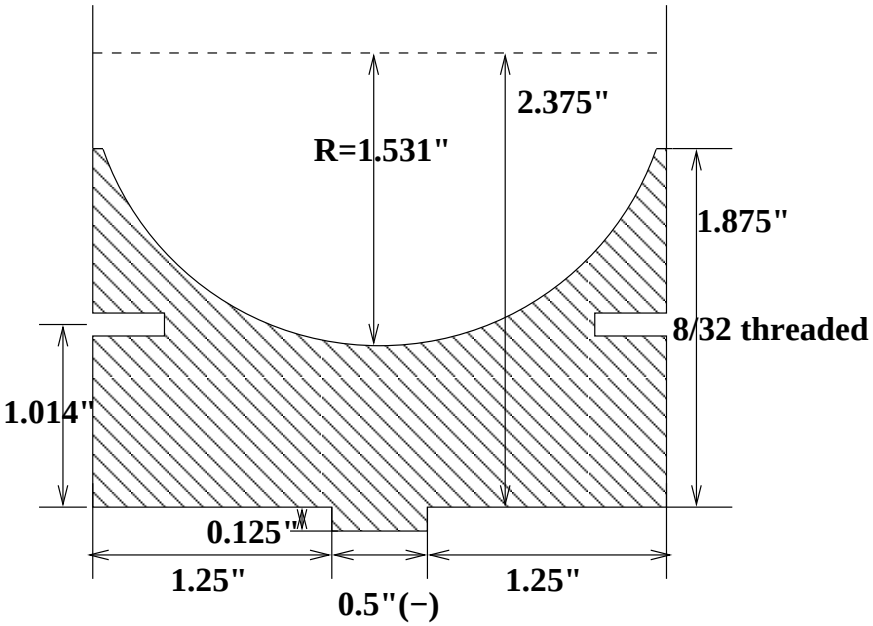

Figure E.1: Clamp to support scintillator assembly

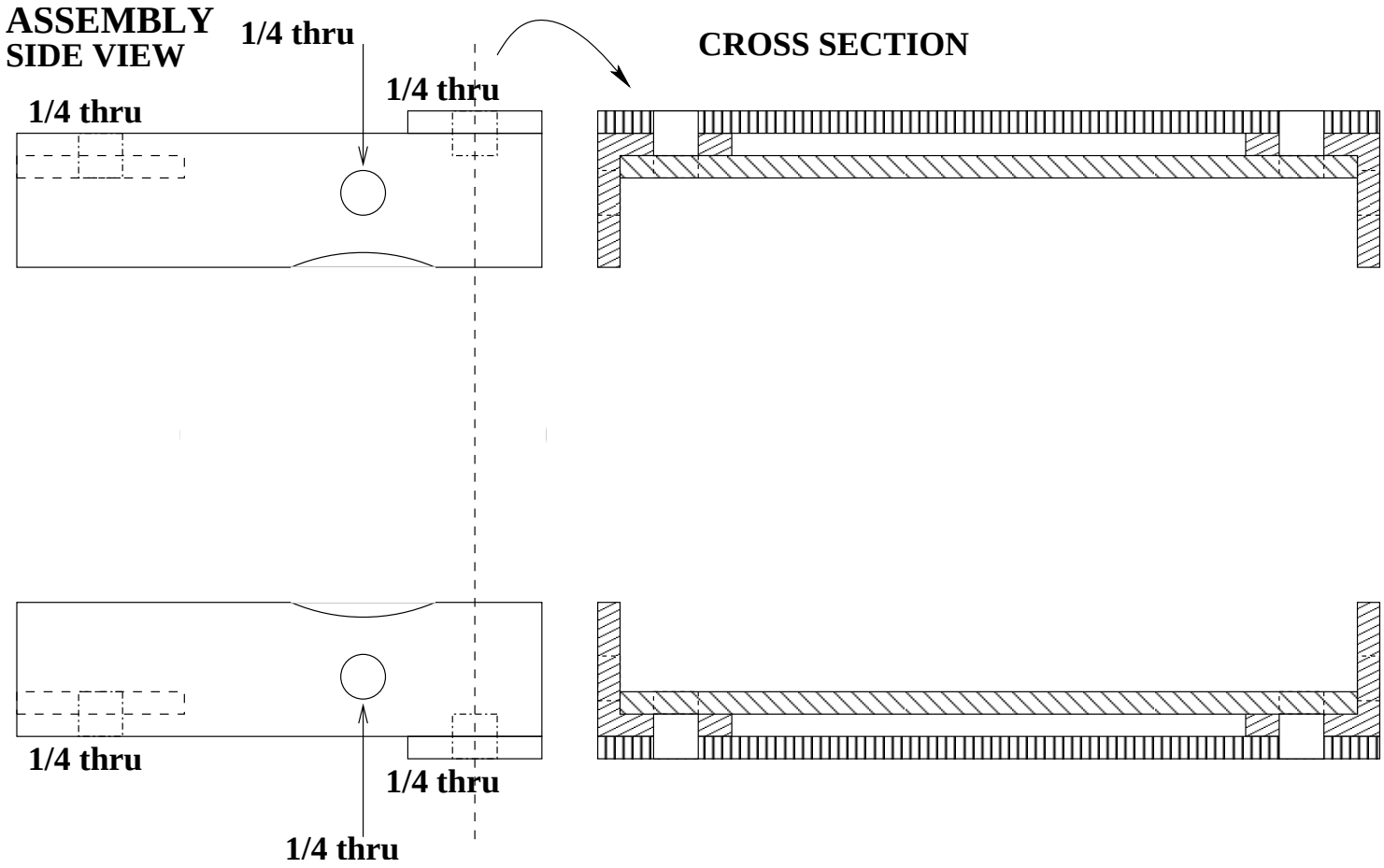

Figure E.2: PMT Mount support assembly.

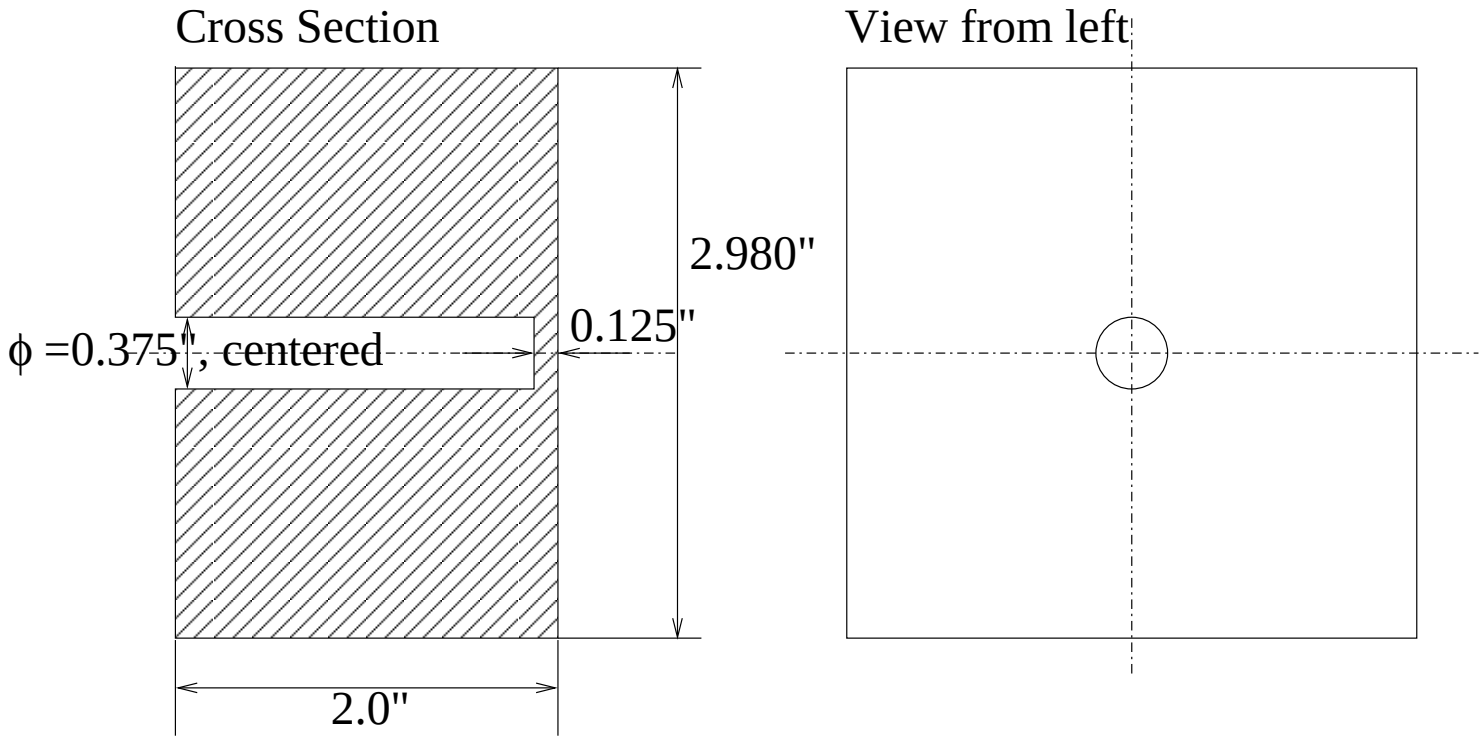

Figure E.3: Scintillator design drawing. The 2” width matched the diameter of the photomultiplier tubes. The thin wall at the end of the cylinder maximizes the x- and γ-ray detection efficiency for the germanium.

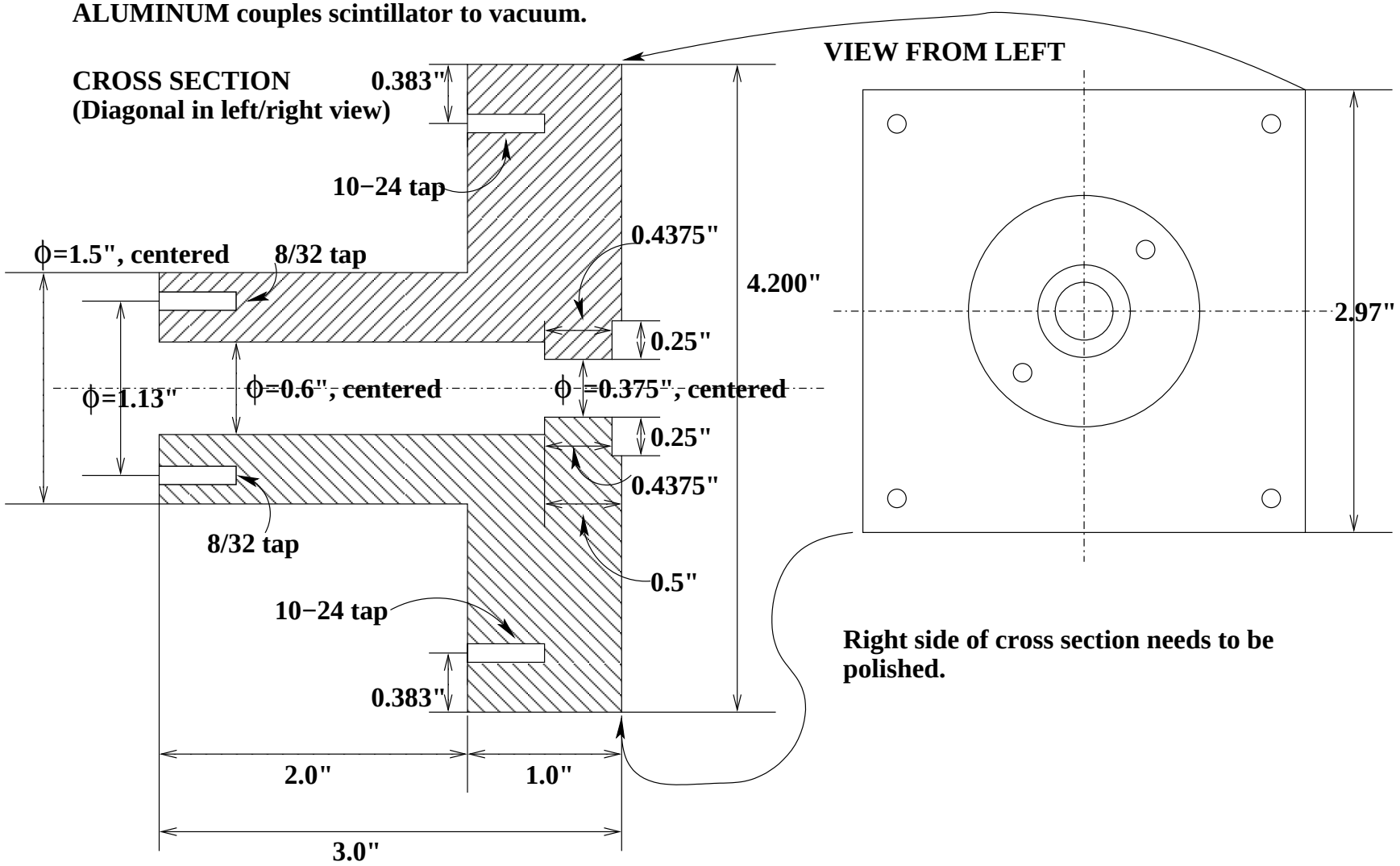

Figure E.4: Aluminum backing and vacuum coupling for the scintillator

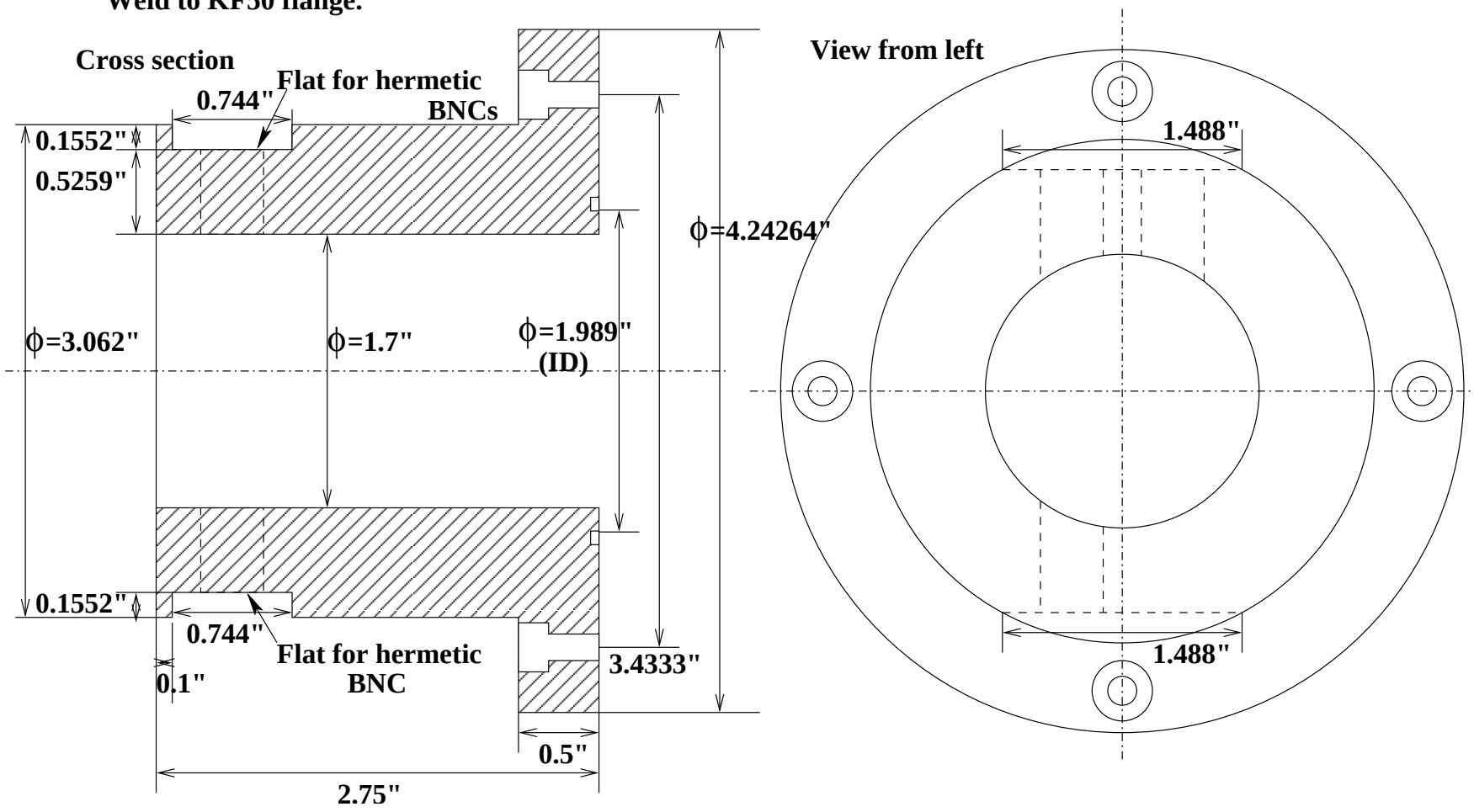

Figure E.5: Stainless steel mount for the scintillator

COPPER INSERT/FOIL HOLDER

Cross section

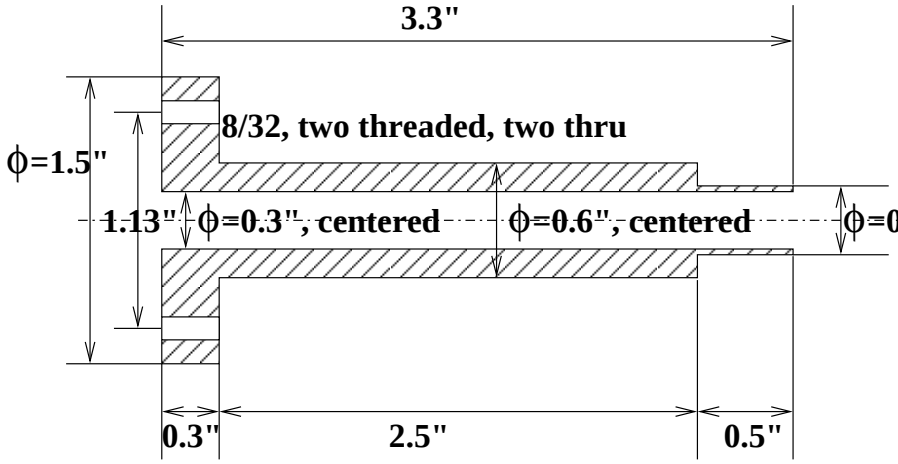

View from left

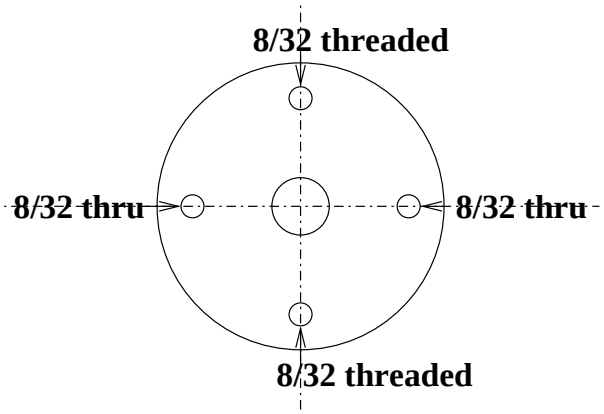

0.6" diameter portion fits snugly into aluminum piece to guide foil into scintillator, but we also need to be able to insert and remove it without it binding to aluminum.

View from right

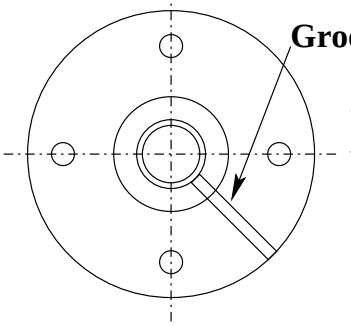

Groove for vacuum: 0.06125" wide by 0.06125" deep. Continuously runs from right side of 1.5" diameter portion in cross section to outside of 0.6" diameter cylinder, along outside of 0.6" diameter cylinder for full 2.5", then from 0.6" to edge of 0.36" diameter portion where foil attaches.

Figure E.6: Copper target-foil holder for the scintillator

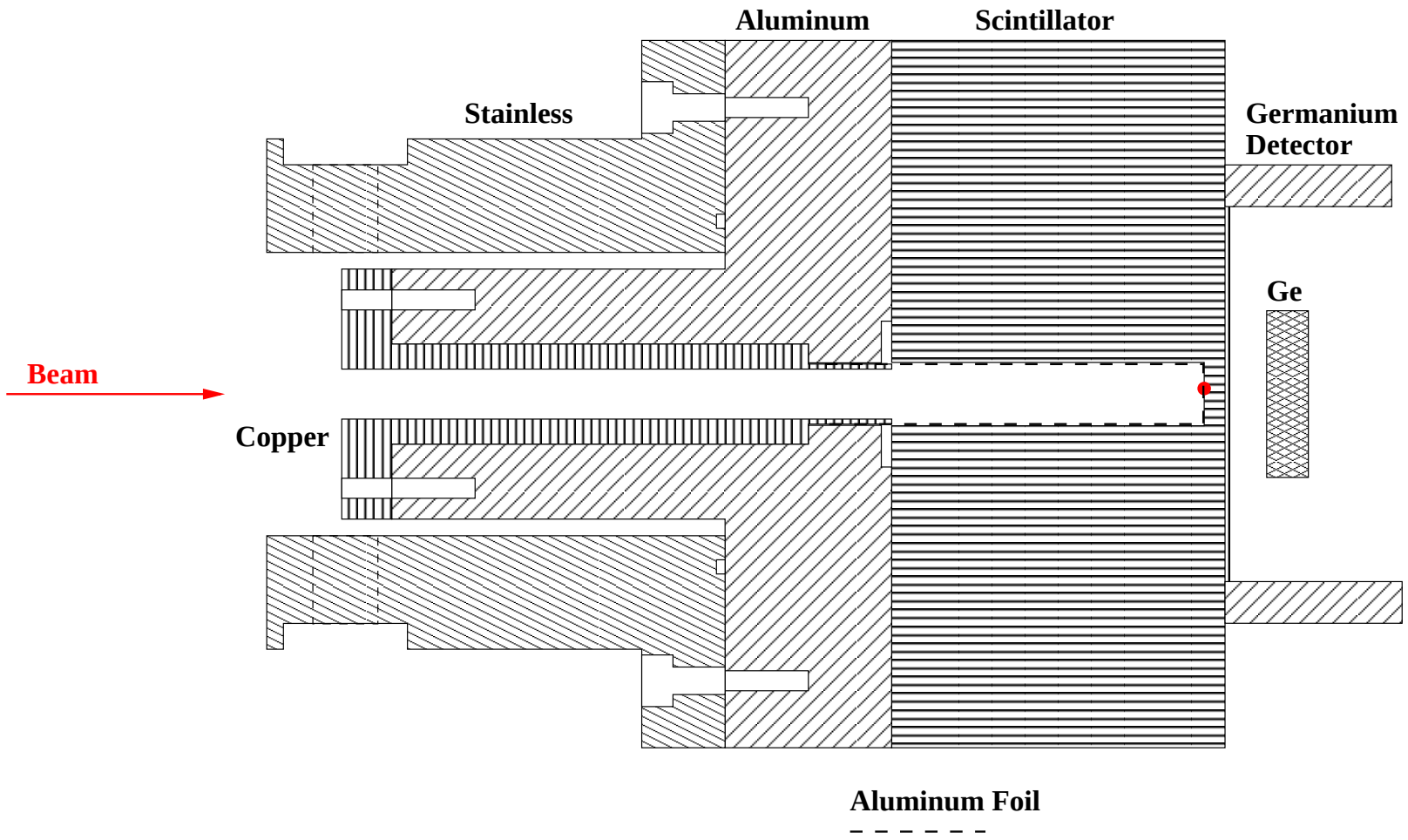

Figure E.7: Composite drawing of the scintillator in the experimental setup

Appendix F

DEAD TIME

Dead time is the time during which signals may be lost because some component of the detection system is busy. Each component of a system from the detector to the final data acquisition has some characteristic length of time required to perform its function. Signals can be lost or altered when one of the components is subjected to too high of a rate. The higher the rate, the shorter the time between events, and the probability for another event to occur within the dead time interval increases.

There are two limiting models for dead time, paralyzable and nonparalyzable. Figure F.1 illustrates these two models. In the paralyzable model, any signal that comes during the dead time from a previous signal resets the system's dead time. In the nonparalyzable model, the next signal to come after the dead time is recorded, regardless of how many signals come during the dead time.

Nonparalyzable behavior is more desirable, both because it is easier to correct and because less events are lost. Consider a nonparalyzable system with a characteristic dead time, τ, and an observed event rate, m. On average, the fraction of events lost must be equal to the product, $m\tau$. The actual event rate, n, can be related to the measured event rate by multiplying it by the fraction of time that the system is live, $1 - m\tau$. Solving for the true rate, one finds

$$n = \frac{m}{1 - m\tau}. \tag{F.1}$$

With paralyzable behavior, there must be a time interval τ between events for the latter event to be recorded. The probability of a time interval τ between events with an average rate n is $e^{-n\tau}$. Using this probability to relate the actual and recorded event rates, one finds

$$ne^{-n\tau} = m. \tag{F.2}$$

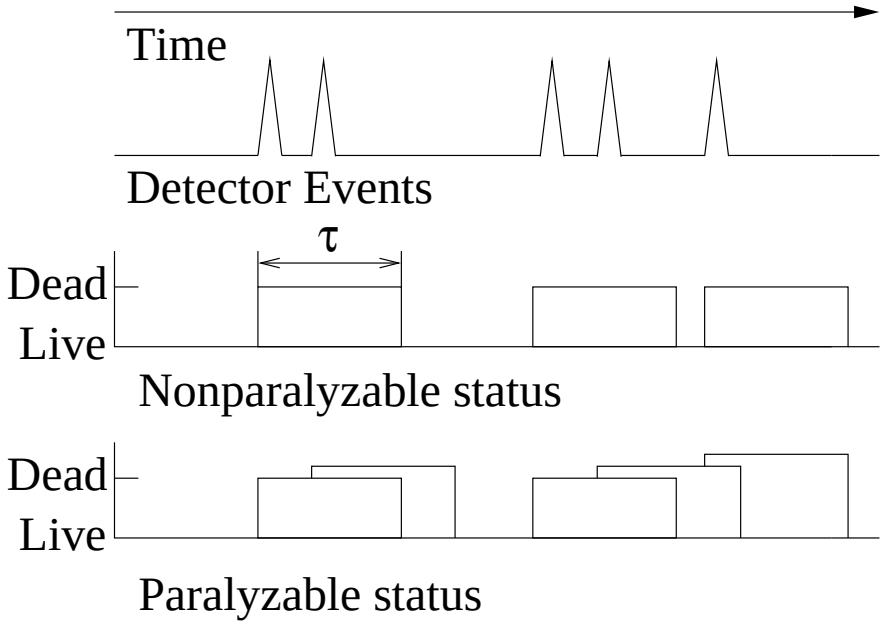

Figure F.1: Illustration of the behavior of a nonparalyzable and paralyzable system, both with dead time τ. With nonparalyzable behavior, three of five events are recorded. The paralyzable system only records two events.

In the limit where the product $n\tau \ll 1$, including only the first two terms of the exponential's Taylor series yields

$$n = \frac{m}{1 - n\tau} = \frac{m}{1 - \frac{m\tau}{1-n\tau}} \approx \frac{m}{1 - m\tau}, \tag{F.3}$$

so that the two models give the same result when the rates are small compared to $\frac{1}{\tau}$. Note that the observed rate approaches zero in the limit $n\tau \gg 1$ for the paralyzable model, while the observed rate becomes $\frac{1}{\tau}$ in the same limit for the nonparalyzable model.

In summary, it is best to avoid scenarios in which the product $m\tau$ becomes large, so that corrections due to dead time are small. Smaller corrections lead to less error. When the dead time is small enough relative to the event rate, it is unimportant which type of behavior best characterizes the system, since both models give the same result. For more background on dead time, see Knoll [55].

Appendix G

GENERAL $V-A$ HADRON CURRENT MATRIX ELEMENT

This section includes the matrix element for the most general Lorentz-invariant $V-A$ hadron current and an outline of the procedure used to calculate it. The following form of the hadron current (see Equation 6.4) was more convenient for calculations:

$$\langle p(p')|J^{\mu}|n(p,\overrightarrow{s})\rangle = \overline{p}(p')\Big[F_1\gamma^{\mu} + \frac{F_2}{m_n}p_n^{\mu} + \frac{F_3}{m_n}q^{\mu} - G_1\gamma^{\mu}\gamma_5 - \frac{G_2}{m_n}\gamma_5 p_n^{\mu} - \frac{G_3}{m_n}\gamma_5 q^{\mu}\Big]n(p,\overrightarrow{s}). \tag{G.1}$$

This form can be obtained from Equation 6.4 by simple Dirac Equation algebra. Since the weak lepton current is purely left-handed, consisting only of a vector and axial vector coupling, the hadron current can only contribute to a lepton decay via vector and axial vector currents. The form factors, f_i and g_i, are functions of the momentum transfer $q^{\mu} = (p_n - p_p)^{\mu}$, and as stated above they contain the effects from QCD and QED for the quarks that are the true elementary particles within the neutron and proton.

The vector q^{μ} is the conserved quantity in the process. The expression for J^{μ} is the most general expression possible for a strictly vector and axial vector current, since it exhausts the possibilities for constructing vectors and axial vectors from combinations of γ matrices and the momentum transfer, q^{μ}.

It is possible to simplify this expression for calculation by rewriting the terms involving $i\sigma^{\mu\nu} = i\frac{i}{2}[\gamma^{\mu},\gamma^{\nu}] = -\frac{1}{2}[\gamma^{\mu},\gamma^{\nu}]$. The Dirac Equation and a few identities for the γ matrices suffice. Consider two useful identities for the Dirac spinors first:

$$(p^{\mu}\gamma_{\mu} - m)u = 0 \rightarrow p^{\mu}\gamma_{\mu}u = mu. \tag{G.2}$$

Similarly for for $\overline{u}$, one obtains

$$\overline{u}p^{\mu}\gamma_{\mu} = \overline{u}m. \tag{G.3}$$

As for the γ matrices, all we need is the identity $\{\gamma^\mu, \gamma^\nu\} = 2g^{\mu\nu}$. Now rewrite the f_2 term:

$$\begin{aligned}
\overline{p}\tfrac{1}{2}\sigma^{\mu\nu}k_\nu n &= \overline{p}\frac{1}{2}\left(\gamma^\mu\gamma^\nu - \gamma^\nu\gamma^\mu\right)k_\nu n \\
&= \overline{p}\frac{1}{2}\left(\{\gamma^\mu, \gamma^\nu\} - 2\gamma^\nu\gamma^\mu\right)k_\nu n \\
&= \overline{p}\left(g^{\mu\nu}k_\nu - k_\nu\gamma^\nu\gamma^\mu\right)n \\
&= \overline{p}\left(k^\mu - (p_n - p_p)_\nu\gamma^\nu\gamma^\mu\right)n \\
&= \overline{p}\left(k^\mu + p_{p\nu}\gamma^\nu\gamma^\mu - p_{n\nu}\gamma^\nu\gamma^\mu\right)n \\
&= \overline{p}\left(k^\mu + m_p\gamma^\mu - p_{n\nu}2g^{\mu\nu} + \gamma^\mu\gamma^\nu p_{n\nu}\right)n \\
&= \overline{p}\left(k^\mu + (m_p + m_n)\gamma^\mu - 2p_n^\mu\right)n, \qquad \text{(G.4)}
\end{aligned}$$

from which one deduces

$$\overline{p}\left(f_2\frac{1}{2}[\gamma^\mu, \gamma^\nu]\frac{k_\nu}{m_n}\right)n = \overline{p}f_2\left(\frac{k^\mu}{m_n} + (1 + \frac{m_p}{m_n})\gamma^\mu - 2\frac{p_n^\mu}{m_n}\right)n \qquad \text{(G.5)}$$

A nearly identical calculation for g_2 using the identity $\{\gamma^\mu, \gamma^5\} = 0$ yields

$$\overline{p}\left(g_2\frac{1}{2}[\gamma^\mu, \gamma^\nu]\gamma_5\frac{k_\nu}{m_n}\right)n = \overline{p}g_2\left(\gamma_5 k^\mu - (1 - \frac{m_p}{m_n})\gamma_5\gamma^\mu - 2\gamma_5\frac{p_n^\mu}{m_n}\right)n. \qquad \text{(G.6)}$$

The desired form for easier calculation is now easy to see. Using the neutron's rest frame, $p_n = (m_n, \overrightarrow{0})$, and $q = (m_n - E_p, \overrightarrow{p_e} + \overrightarrow{p_\nu}) = (E_e + E_\nu, \overrightarrow{p_e} + \overrightarrow{p_\nu})$. Calculations in terms of p_n will be very simple in the neutron's rest frame, where $\frac{1}{2}[\gamma^\mu, \gamma^\nu]k_\nu$ would have been quite unwieldy. To calculate matrix elements we will use Equation G.1, then after calculations we can transform the results to the from factors of Equation 6.4 using the identities

$$\begin{aligned}
F_1 &= f_1 + (1 + \frac{m_p}{m_n})f_2 \\
F_2 &= -2f_2 \\
F_3 &= f_2 + f_3 \\
G_1 &= g_1 - (1 - \frac{m_p}{m_n})g_2 \\
G_2 &= -2g_2 \\
G_3 &= g_2 + g_3. \qquad \text{(G.7)}
\end{aligned}$$

More calculations are avoided by choosing a definite form for the neutron spinor. The quantity that will enter calculations is $n\bar{n}$. The spinor for a polarized neutron at rest in the Weyl basis is

$$\begin{aligned} n\bar{n} &= \sqrt{m_n}(1,0,1,0)^T\sqrt{m_n}(1,0,1,0) \\ &= \frac{m_n}{2}(1+\gamma_0\gamma_3\gamma_5+\gamma_0+\gamma_3\gamma_5). \end{aligned} \tag{G.8}$$

All observables will be proportional to $|\mathcal{M}|^2$. This means there will always be two of the form factors in any term. If one considers the definite form for the polarized, at-rest neutron spinor, matrix algebra obviates half of the calculations. Begin by considering $|F_1|^2 \to |G_1|^2$. We need only look at the γ matrices involved. $|F_1|^2$ involves

$$\gamma^\mu(1+\gamma_0\gamma_3\gamma_5+\gamma_0+\gamma_3\gamma_5)\gamma^\nu. \tag{G.9}$$

$|G_1|^2$ can be written in exactly the same form with only a couple sign changes, by anticommuting γ matrices and using $\gamma_5^2 = 1$.

$$\begin{aligned} &\gamma^\mu\gamma_5(1+\gamma_0\gamma_3\gamma_5+\gamma_0+\gamma_3\gamma_5)\gamma^\nu\gamma_5 \\ &= \gamma^\mu(\gamma_5)^2(-1-\gamma_0\gamma_3\gamma_5+\gamma_0+\gamma_3\gamma_5)\gamma^\nu \\ &= \gamma^\mu(-1-\gamma_0\gamma_3\gamma_5+\gamma_0+\gamma_3\gamma_5)\gamma^\nu \end{aligned} \tag{G.10}$$

The $|G_1|^2$ term is exactly the same as the $|F_1|^2$ term, but the $n\overline{n}$ terms with an even number of γ's have changed sign. The net effect is that these terms in the matrix element give the same result, with the transormation $|F_1|^2 \to |G_1|^2$ requiring $m_p \to -m_p$. Using the same procedure one can also see that $|F_{2/3}|^2 \to |G_{2/3}|^2$ has the same effect; this also applies to $F_2F_3^* \to G_2G_3^*$. Including the complex conjugate terms that come with the $F_2F_3^*$ lot, ten calculations have now reduced to four.

$F_1F_{2/3}^* \to G_1G_{2/3}^*$ will reduce four more calculations to one. $F_1F_2^*$ has the following combination of γ matrices:

$$\gamma^\mu(1+\gamma_0\gamma_3\gamma_5+\gamma_0+\gamma_3\gamma_5). \tag{G.11}$$

Now rearrange the $G_1 G_2^*$ matrices into the same combinations.

$$\begin{aligned} & -\gamma^\mu \gamma_5 (1 + \gamma_0 \gamma_3 \gamma_5 + \gamma_0 + \gamma_3 \gamma_5) \gamma_5 \\ & = \gamma^\mu (\gamma_5)^2 (-1 - \gamma_0 \gamma_3 \gamma_5 + \gamma_0 + \gamma_3 \gamma_5) \\ & = \gamma^\mu (-1 - \gamma_0 \gamma_3 \gamma_5 + \gamma_0 + \gamma_3 \gamma_5) \end{aligned} \tag{G.12}$$

Thinking about the combinations of γ matrices that will yield non-zero traces when this is sandwiched between the proton spinors, the result is the same as the $F_1 F_2^*$ contribution with $p_p \to -p_p$.

All that remains is algebra with the γ matrices. The resulting matrix element can be expressed in the form

$$|\mathcal{M}|^2 = \frac{1}{2m_n} \frac{1}{2E_e} \frac{1}{2E_\nu} \frac{1}{2E_p} \times 16[C_1 + C_2 \overrightarrow{P} \cdot \overrightarrow{p_e} + C_3 \overrightarrow{P} \cdot \overrightarrow{p_\nu} + C_4 \overrightarrow{P} \cdot (\overrightarrow{p_e} \times \overrightarrow{p_\nu})], \tag{G.13}$$

in which each C_i is a function of p_e, p_ν, p_p, and the six form factors, F_i and G_i, $i = 1, 2, 2$. $\overrightarrow{P}$ is just a unit vector in the direction of the neutron's polarization. Expressing each

C_i in terms of the form factors, one finds,

$$
\begin{aligned}
C_1 &= |F_1|^2 2m_n[E_\nu(p_p\cdot p_e)+E_e(p_p\cdot p_\nu)-m_p(p_e\cdot p_\nu)] \\
&+|F_2|^2 m_n(W_p+m_p)[2E_eE_\nu-(p_e\cdot p_\nu)] \\
&+2\mathrm{Re}(F_1F_2^*)m_n[E_\nu(p_p\cdot p_e)+E_e(p_p\cdot p_\nu)+2m_pE_\nu E_e-(E_p+m_p)(p_e\cdot p_\nu)] \\
&+4\mathrm{Re}(F_1G_1^*)m_n[E_\nu(p_p\cdot p_e)-E_e(p_p\cdot p_\nu)] \\
&+2\mathrm{Re}(F_1F_3^*)m_e^2[(p_p\cdot p_\nu)+W_\nu m_p] \\
&+2\mathrm{Re}(F_2F_3^*)E_\nu m_e^2(E_p+m_p) \\
&+|F_3|^2\frac{1}{m_n}m_e^2(W_p+m_p)(p_e\cdot p_\nu) \\
&+\text{symmetric terms}
\end{aligned}
\tag{G.14}
$$

$$
\begin{aligned}
C_2 &= |F_1|^2 2m_n[W_\nu m_p-(p_p\cdot p_\nu)] \\
&+2\mathrm{Re}(F_1F_2^*)m_n[E_pE_\nu-(p_p\cdot p_\nu)] \\
&+4\mathrm{Re}(F_1G_1^*)m_n(p_p\cdot p_\nu) \\
&-2\mathrm{Re}(F_2G_2^*)m_n[2E_eE_\nu-(p_e\cdot p_\nu)] \\
&-2\mathrm{Re}(F_1G_2^*)m_n[2E_eE_\nu-(p_e\cdot p_\nu)+(E_p-m_p)E_\nu] \\
&-2\mathrm{Re}(F_1G_3^*)m_e^2E_\nu \\
&-2\mathrm{Re}(F_2G_3^*)m_e^2E_\nu \\
&-2\mathrm{Re}(F_3G_3^*)\frac{1}{m_n}m_e^2(p_e\cdot p_\nu) \\
&+\text{symmetric terms}
\end{aligned}
\tag{G.15}
$$

$$
\begin{aligned}
C_3 &= -|F_1|^2 2m_n[E_em_p-(p_p\cdot p_e)] \\
&-2\mathrm{Re}(F_1F_2^*)m_n[E_pE_e-(p_p\cdot p_e)] \\
&+4\mathrm{Re}(F_1G_1^*)m_n(p_p\cdot p_e) \\
&-2\mathrm{Re}(F_2G_2^*)m_n[2E_eE_\nu-(p_e\cdot p_\nu)] \\
&-2\mathrm{Re}(F_1G_2^*)m_n[2E_eE_\nu-(p_e\cdot p_\nu)+(E_p-m_p)E_e] \\
&-2\mathrm{Re}(F_1G_3^*)m_e^2(E_\nu+E_p-m_p) \\
&-2\mathrm{Re}(F_2G_3^*)m_e^2E_\nu \\
&-2\mathrm{Re}(F_3G_3^*)\frac{1}{m_n}m_e^2(p_e\cdot p_\nu) \\
&+\text{symmetric terms}
\end{aligned}
\tag{G.16}
$$

$$
\begin{aligned}
C_4 &= 2\mathrm{Im}(F_1 F_2^*)(E_\nu - E_e) \\
&+2\mathrm{Im}(F_1 G_1^*) m_n m_p \\
&+2\mathrm{Im}(F_1 G_2^*)(E_p - m_p) \\
&-2\mathrm{Im}(F_1 F_3^*) m_e^2 \\
&+\text{symmetric terms}
\end{aligned}
\tag{G.17}
$$

The symmetric terms follow from the substitutions outlined above.

VITA

Sky Sjue was born in Hawaii in 1979. He spent his formative years between Fargo, North Dakota; Lubbock, Texas; and finally Portland, Oregon, where he attended three years of high school followed by a year of invaluable life experience before he obtained his G.E.D. He graduated from Texas Tech University *summa cum laude* with a B.S. in Mathematics and Physics in 2001. He subsequently pursued graduate studies at the University of Washington in Seattle, where he earned his M.S. in Physics in 2003 *en route* to a Ph.D. in Physics in 2008.